

# Fermi Search for Pulsar Wind Nebulae and constraints on the Galactic TeV source population

R. Rousseau, J. Lande, M. Lemoine–Goumard, S. Funk...

## ABSTRACT

Since its launch, the *Fermi* satellite has firmly identified 7 pulsar wind nebulae (PWNe) plus a large number of candidates, all powered by young and energetic pulsars. Furthermore, PWNe are the most populous class in the TeV energy range followed by the unidentified sources (UNID). Using 45 months of Fermi–LAT data, we looked around the position of 58 TeV sources to bring new constraints on the models and new clues on the nature of sources without counterparts. For each of them we derived a  $\gamma$ -ray flux or an upper limit (when the TeV source is not detected at GeV energies by the *Fermi*–LAT) above 10 GeV.

The wealth of multi-wavelength data available and the new results provided by *Fermi*–LAT is an extraordinary opportunity to constrain the origin of the  $\gamma$ -ray emission of the large sample of UNID and the radiative processes taking place in known PWNe.

*Subject headings:* Catalogs; Fermi Gamma-ray Space Telescope; Gamma rays; observations; pulsar wind nebula

## 1. Introduction

Since 2003, the continuous observation of the Galactic Plane by Čerenkov telescopes have yielded the detection of more than 80 Galactic sources. Among them, pulsar wind nebulae (PWNe) is the dominant class with more than 30 firm identifications. However, a similar number of Galactic sources cannot be associated to a counterpart in any other wavelength. They are ranked in the unidentified (UNID) class.

Multi-wavelength observations are essential to constrain the emission mechanisms occurring in these sources and identify their nature. The Large Area Telescope (LAT) aboard the *Fermi* Gamma-ray Space Telescope (*Fermi*) is especially useful in this context. Covering the energy range from  $\sim 100$  MeV to more than 300 GeV, the LAT provides a precise view of the  $\gamma$ -ray sky. With 2 years of observations, the *Fermi*–LAT Second Catalog (Nolan et al. 2012) already contains 1873 sources, 1397 being identified and 576 without counterparts.

Two different scenarii are proposed to explain the observed  $\gamma$ -ray radiation : the accelerated particles are either electrons (leptonic scenario) or protons (hadronic scenario). In the hadronic scenario,  $\gamma$ -ray photons are created by  $\pi^0$  decay from the interaction of accelerated hadrons with nuclei of the interstellar medium. In the leptonic scenario,  $\gamma$ -ray photons are created by inverse Compton (IC) scattering of the accelerated leptons on the ambient photon fields (CMB, Stellar Radiation, IR, ...).

Leptonic sources such as relic PWNe (de Jager & Djannati-Ataï 2009; de Jager et al. 2009) and hadronic sources such as old supernova remnants interacting with molecular clouds (Uchiyama 2011) have been proposed to explain the population of unidentified sources.

The distinction between these two scenarii is done by studying the link between the TeV and the GeV energy range. Slane et al. (2010); Grondin et al. (2011); Rousseau et al. (2012) have demonstrated the potential that can be provided by the use of LAT observations to study PWNe candidates. Up to now, except Vela-X (Abdo et al. 2010d), the 7 PWNe firmly identified by Fermi are all associated to a TeV counterpart and show a hard spectrum consistent with an IC peak above 100 GeV (Abdo et al. (2010c), Grondin et al. (2011)).

The motivation of this work is to bring new constraints on already known PWNe and to look for new candidates among the unidentified TeV sources. A search for  $\gamma$ -ray emission in the off-pulse window of the  $\gamma$ -ray detected pulsars, updating the method proposed in Ackermann et al. (2011), will be presented in Abdo et al. (in prep.c). The strategy presented in our work (this paper) is closer to Tam et al. (2010) in the sense that we analyzed the *Fermi*-LAT data around already known potential PWNe.

The sources included in our search were detected by H.E.S.S., VERITAS, MAGIC and MILAGRO. H.E.S.S. (Aharonian et al. 2006c) is composed of four telescopes observing the very high energy (VHE) sky from 0.1 to 100 TeV with a mean point spread function (PSF) of  $\sim 0.1^\circ$  for a point-source sensitivity around 1% of the Crab flux above 200 GeV for 25 hours of observations. The four telescopes of VERITAS (Weekes et al. 2002) detect the  $\sim 0.1$  to 30 TeV  $\gamma$ -rays with a sensitivity of 1% of the Crab in less than 30 hours and an angular resolution lower than  $0.1^\circ$  at 1 TeV. MAGIC (Aleksić et al. 2012) consists of two telescopes observing from  $\sim 50$  GeV to several tens of TeV with a sensitivity of  $\sim 0.8\%$  of the Crab nebula flux above 300 GeV with a  $\sim 0.1^\circ$  PSF. MILAGRO (Atkins et al. 2004) is a water Čerenkov detector with a large field of view (FoV) of  $\sim 2\text{sr}$  and a  $\sim 0.45^\circ$  angular resolution observing  $\gamma$ -rays from  $\sim 1$  to 100 TeV.

Starting from the TeV catalog website <sup>1</sup>, which summarizes all sources detected at TeV

---

<sup>1</sup><http://tevcat.uchicago.edu/>

energies, we established a list of sources possibly associated to PWNe (Section 3), that we studied using the method and the tools described in Section 4. The most interesting cases as well as the spatial and spectral results will be discussed (Section 5) before being presented in the context of a complete population study (Section 6).

## 2. LAT Description and Observations

The LAT is a  $\gamma$ -ray telescope that detects photons by conversion into electron-positron pairs and operates in the energy range between 20 MeV and more than 300 GeV. Details of the instrument and data processing are given in Atwood et al. (2009). The on-orbit calibration is described in Abdo et al. (2009e).

The following analysis was performed using 45 months of data collected from August 4, 2008 to April 18, 2012 (MET : 239557440–356439741) within a  $7^\circ \times 7^\circ$  square (see section 4) around the position of the TeV source aligned with Galactic coordinates. We excluded  $\gamma$ -rays coming from a zenith angle larger than  $100^\circ$  because of possible contamination from secondary  $\gamma$ -rays from the Earth’s atmosphere (Abdo et al. 2009d). We used the Pass 7 clean event class that has a substantial reduction in instrumental background above 10 GeV with only a small loss in effective area (compared to the standard event class).

This energy of 10 GeV is a good compromise between photon statistics, angular resolution necessary to study the shape of the TeV sources and proximity to the energy range covered by the Čerenkov telescopes. This also greatly reduces the contribution of the Galactic diffuse background.

The counts map in Figure 1 summarizes the regions of the Galactic Plane analyzed here. The bright pulsars Vela and Geminga clearly stand out, as well as the SNR IC443. In addition to these famous objects, a large number of sources clearly appears along the Galactic Plane, several of them being coincident with TeV detected sources, such as HESS J1614–518 and HESS J1616–508. They will be discussed in Section 5. The large number of sources visible in this counts map highlight perfectly the capabilities now offered at high energy by the LAT.

## 3. List of candidates

As a starting point, we used the catalog of TeV sources provided by the university of Chicago<sup>1</sup> to build our list of candidates. This catalog summarizes the information of all sources detected by the TeV experiments. Looking for PWNe candidates which are Galactic

sources, we selected the sources located within  $\pm 5^\circ$  in latitude.

The Galactic center being a complex region to study with *Fermi*-LAT, due to the contamination by the large density of sources and by the diffuse emission, we removed all sources within  $5^\circ$  of the Galactic center. Therefore, we did not include to our list the three sources HESS J1745-303, HESS J1741-302 and G 0.9+0.1 (Falleti et al. in prep.; Ergin et al. in prep.).

TeV sources associated to SNRs will not be discussed in this analysis. These sources will be included in a forthcoming paper which aims at bringing constraints on all known SNRs using the *Fermi*-LAT data Abdo et al. (in prep.b).

Finally we removed from this analysis the Crab Nebula and Vela-X. Both were already studied in details (Abdo et al. (2010c), Buehler et al. (2012)), and the second is the object of a new analysis Grondin et al. (in prep.).

The final list of 58 sources studied in this analysis is summarized in Table 1 together with their morphology as seen in TeV.

## 4. Conventions and methods

### 4.1. Modeling of the regions of interest

Two different tools were used to perform the spatial and spectral analysis: **gtlike** (Mattox et al. 1996) and **pointlike** (Kerr 2011; Lande et al. 2012). These tools fit a source model to the data along with models for the instrumental, extragalactic and Galactic components of the background. We used the version 09–28–00 of the *Fermi* Science Tools.

**pointlike** and **gtlike** using two different shapes for the region of interest, we used all events contained in a disk of radius  $5^\circ$  centered on the location of the TeV source when fitting the region with **pointlike** and we used a  $7^\circ \times 7^\circ$  square included in the previous disk when fitting the region using **gtlike**. We tried to keep the two methods as close as possible by using the same conventions (same spatial binning :  $\sim 0.06^\circ/\text{bin}$ , same energy binning : 8 energy bins per decade between 10 GeV and 316 GeV, same optimizer : MINUIT (James & Roos 1975)).

In the following analysis, the Galactic diffuse emission was modeled by the standard LAT diffuse emission ring–hybrid model *ring\_2yearp7v6\_v0.fits* for all sources. The residual cosmic-ray background and extragalactic radiation are described by a single isotropic component with a spectral shape described by the file *isotrop\_2year\_P76\_clean\_v0.txt*. The models

have been released and described by the *Fermi*-LAT Collaboration through the FSSC<sup>2</sup>. In the following, we fixed the isotropic diffuse normalization to limit the number of free parameters and reduce the uncertainties on the fitted parameters.

Sources within  $10^\circ$  around each source of interest and listed in the hard source list (Abdo et al. in prep.a) were included in our spatial-spectral model. We replaced potential TeV counterparts by a source with the TeV morphology summarized in Table 1. The spectral parameters of sources closer than  $2^\circ$  to the source of interest were left free, while the parameters of all other sources were fixed at the hard source list (1FHL) catalog values (Abdo et al. in prep.a).

Table 2 summarizes the sources of our list located close to a pulsar detected by the *Fermi*-LAT (Abdo et al. in prep.c). The proximity of the pulsar can lead either to the non detection of a faint source hidden by the pulsed emission or to a contamination at low energy if the pulsar is not included. We decided to include in our analysis all pulsars located outside of the TeV template or more than  $0.27^\circ$  away from the source of interest, corresponding to the average PSF above 10 GeV. Section 5.2 will show the results for the sources close to the pulsars in the case where we added the pulsar in the model and fitted the TeV source.

Due to the longer integration time of our analysis with respect to the 1FHL catalog (45 vs 36 months in the 1FHL), the appearance of additional sources is expected. To prevent contamination from these sources, we looked over all our regions and added to the model all excesses with a significance above  $4.0\sigma$  which corresponds to a  $TS > 25$  with 4 degrees of freedom (2 spatial and 2 spectral, see Section 4.4). The location and spectral parameters of these sources are described in Table 3. We fitted their spectra assuming a pure power-law above 10 GeV.

## 4.2. Analysis of the shape

Estimation of the position and extension of each PWNe candidates was performed using `pointlike`. `pointlike` is an alternate binned likelihood technique, optimized for characterizing the extension of a source (unlike `gtlike`), that was extensively tested against `gtlike` (Kerr 2011; Lande et al. 2012). To fit an extended source, `pointlike` convolves the extended source shape with the PSF (as a function of energy) and uses the MINUIT library (James & Roos 1975) to maximize the likelihood by simultaneously varying the position, extension, and spectrum of the source. Lande et al. (2012) present more details on the method

---

<sup>2</sup><http://fermi.gsfc.nasa.gov/ssc/data/access/lat/BackgroundModels.html>

146 used and its validation.

147 As previously done in Lande et al. (2012), we only used a radially-symmetric uniform  
148 disk shape (defined in Equation 1) to fit the extension of the GeV emission. In the following,  
149 we quote the radius to the edge ( $\sigma$ ) as the size of the source.

$$I_{\text{disk}}(x, y) = \begin{cases} \frac{1}{\pi\sigma^2} & x^2 + y^2 \leq \sigma^2 \\ 0 & x^2 + y^2 > \sigma^2. \end{cases} \quad (1)$$

### 150 4.3. Spectral analysis

151 We performed the spectral analysis of each TeV candidate using **pointlike** and **gtlike**,  
152 the standard likelihood analysis package for LAT data implemented in the Science Tools  
153 and distributed by the FSSC. It is a binned maximum-likelihood method (Mattox et al.  
154 1996) that was extensively validated for spectral analysis and makes fewer approximations  
155 in calculating the likelihood than **pointlike**. Both methods provided results in agreement  
156 with each other, but all spectral parameters quoted in the following were obtained using  
157 **gtlike**. The spectrum of each source was determined using the best morphological model  
158 provided by **pointlike**. Due to the narrow energy range which prevents the detection of  
159 curved spectra, we fitted all sources assuming a pure power-law of differential flux  $K$  and  
160 index  $\Gamma$  presented in Equation 2.

$$\frac{dN}{dE} = K \times \left( \frac{E}{E_0} \right)^\Gamma \quad (2)$$

161 To minimize the covariance between  $K$  and  $\Gamma$ , we ran the whole analysis twice. In the  
162 first iteration, we fitted the source assuming a power-law model depending on the integral  
163 flux  $N$  and  $\Gamma$  shown in Equation 3.

$$\frac{dN}{dE} = \frac{N \times (\Gamma + 1) \times E^\Gamma}{E_{\text{max}}^{\Gamma+1} - E_{\text{min}}^{\Gamma+1}} \quad (3)$$

164 Using the covariance matrix between the parameters of the fit, we derived the pivot  
165 energy  $E_p$  computed as the energy at which the relative uncertainty on the differential flux  
166  $K$  was minimal (Nolan et al. 2012). Then, we refitted the spectrum of the source assuming  
167 a power-law spectral model (Equation 2) with the scale parameter  $E_0$  fixed at  $E_p$ .

168 Once the morphological and spectral fit was determined, we derived the photon flux

169  $F(10\text{--}316\text{ GeV})$  in photons  $\text{cm}^{-2}\text{ s}^{-1}$  and the energy flux  $G(10\text{--}316\text{ GeV})$  in  $\text{erg cm}^{-2}\text{ s}^{-1}$   
 170 defined as:

$$F(10 - 316\text{ GeV}) = \int_{10\text{ GeV}}^{316\text{ GeV}} \frac{dN}{dE} dE \quad (4)$$

$$G(10 - 316\text{ GeV}) = \int_{10\text{ GeV}}^{316\text{ GeV}} E \frac{dN}{dE} dE \quad (5)$$

#### 171 4.4. Source significance and extension

172 We measured the source significance using a test statistic (TS) defined as Equation 6,  
 173 where  $\mathcal{L}_1$  corresponds to the likelihood obtained by fitting a model of the source of interest  
 174 and the background model and  $\mathcal{L}_0$  corresponds to the likelihood obtained by fitting the  
 175 background model only.

$$\text{TS} = 2 \times \log(\mathcal{L}_1/\mathcal{L}_0) \quad (6)$$

176 In the following, all TS values were calculated using `gtlike` and the corresponding  
 177 significance was evaluated from the  $\chi^2$  distribution with the corresponding number of degrees  
 178 of freedom (d.o.f.).

179 To decide if a source was significantly detected or not, we selected sources with a TS  
 180 above 16 ( $3.6\sigma$  with 2 d.o.f) when assuming the TeV morphology.

181 To test the extension of each source, following Lande et al. (2012), we defined  $\text{TS}_{ext}$   
 182 as Equation 7 where  $\mathcal{L}_{ext}$  represents the likelihood under an extended source hypothesis (5  
 183 d.o.f.) and  $\mathcal{L}_{ps}$  represents the likelihood assuming a point source (4 d.o.f.). The condition  
 184 for a source to be extended is  $\text{TS}_{ext} > 16$ .

$$\text{TS}_{ext} = 2 \times \log(\mathcal{L}_{ext}/\mathcal{L}_{ps}) \quad (7)$$

185 We also compared the GeV morphology to the TeV shape. The TeV shape was fixed and  
 186 we fitted only the spectra as a power-law. To assess the significance of the GeV morphology  
 187 compared to the TeV shape, we computed  $\text{TS}_{GeV/TeV}$  as Equation 8 where  $\mathcal{L}_{TeV}$  corresponds  
 188 to the likelihood obtained by fitting the source assuming the TeV shape and  $\mathcal{L}_{GeV}$  to the  
 189 likelihood obtained by fitting the source using the best shape derived using *Fermi*-LAT data.

$$\text{TS}_{\text{GeV/TeV}} = 2 \times \log(\mathcal{L}_{\text{GeV}}/\mathcal{L}_{\text{TeV}}) \quad (8)$$

The correspondence between  $\text{TS}_{\text{GeV/TeV}}$  and the significance is evaluated from a  $\chi^2$  distribution with 2 supplementary d.o.f if the best GeV source is a point-like source and 3 supplementary d.o.f if the best GeV source is an extended source. We considered the GeV morphology to be significantly better than the TeV morphology when the likelihood of the fit is better at more than  $3\sigma$  level, which means  $\text{TS}_{\text{GeV/TeV}} > 12$  for a point-like source in GeV, or  $\text{TS}_{\text{GeV/TeV}} > 14$  for an extended source (uniform disk) in GeV. All values of TS,  $\text{TS}_{\text{ext}}$  and  $\text{TS}_{\text{GeV/TeV}}$  quoted in the following are obtained using **gtlike**.

#### 4.5. Procedure followed

The 58 regions summarized in Table 1 were all analyzed using the same procedure with both **gtlike** and **pointlike**:

1. We fitted each source assuming its TeV shape summarized in Table 1. Here, we fixed the position and morphology and fit the spectrum assuming a pure power-law leading the TS to follow a  $\chi^2$  distribution with only 2 d.o.f.
  - For sources with significance above  $3.6 \sigma$  ( $\text{TS} > 16$  with 2 d.o.f.) we applied steps 2 and 3.
  - For sources with  $\text{TS} < 16$  we derived a 99 % upper limit on the flux assuming the TeV morphology and a power-law index of 2.
2. We fitted the source assuming a point source localized with **pointlike** as well as the neighbouring sources within  $2^\circ$ .
3. We fitted the source assuming a disk shape derived using **pointlike** and compared this hypothesis to the point source hypothesis.

To have a self consistent analysis between all regions studied, we performed a third iteration where we used the best shape found in our pipeline for all sources located in the region of interest.

For the significant sources ( $\text{TS}_{\text{TeV}} > 16$ ) we derived both the photon and energy fluxes inferred by the fit with the 1 sigma statistical errors, assuming the best morphology. When the source was not significant ( $\text{TS}_{\text{TeV}} < 16$ ), we derived a 99 % Confidence Level (C.L.)



Bayesian upper limit on the flux using a pure power-law model with an index fixed at 2, assuming the TeV shape.

*Fermi*-LAT spectral points were obtained by splitting the 10–316 GeV range into 3 logarithmically spaced energy bins. A 99 % C.L. upper limit is computed when  $TS < 10$  using the approach used by Nolan et al. (2012). The errors on the spectral points represent the statistic and systematic uncertainties as discussed below.

#### 4.6. Systematics on the extension

Two main systematic uncertainties can affect the extension fit of the sources: uncertainties in our model of the Galactic diffuse emission and uncertainties on our knowledge of the LAT PSF.

To estimate the systematics due to the uncertainty in our knowledge of the PSF, we used the pre-flight Monte Carlo representation of the PSF. Indeed, before launch, the LAT PSF was determined by detector simulations which we verified in accelerator beam tests (Atwood et al. 2009). However, in-flight data revealed a discrepancy above 3 GeV in the PSF compared to the angular distribution of photons. To account for this uncertainty, we refit our extended source candidates using the pre-flight PSF and consider the difference in extension found using the two PSFs as a systematic error on the extension of a source. This procedure was already used by Lande et al. (2012).

To estimate the uncertainties on the Galactic diffuse emission, we used a GALPROP-based model and considered the various components of the diffuse emission model separately. We then individually fit the normalizations of each of them in our likelihood analysis. These various components are  $\gamma$ -rays produced by IC emission,  $\gamma$ -rays produced by interactions of CRs with atomic and ionized interstellar gas, and  $\gamma$ -rays produced in the interactions of CRs with molecular gas. The model component describing the  $\gamma$ -ray intensity from interactions with molecular gas is further subdivided into seven ranges of Galactocentric distance. It is not expected that this diffuse model is superior to the standard LAT model obtained through an all-sky fit. However, adding degrees of freedom to the background model can remove likely spurious sources that correlate with features in the Galactic diffuse emission. Therefore, this tests systematics that may be due to imperfect modeling of the diffuse emission in the region. This procedure was also used by Lande et al. (2012).

The total systematic error on the extension of a source was obtained by adding the two errors in quadrature.

#### 4.7. Systematics on the spectral parameters

Three main systematic uncertainties can affect the LAT flux estimate for an extended source: uncertainties in the Galactic diffuse background, uncertainties on the effective area and uncertainties on the shape of the source.

The dominant uncertainty comes from the Galactic diffuse emission and was estimated by using the GALPROP-based model described in Section 4.6.

The second systematic was determined by using modified IRFs whose effective areas bracket the nominal ones. These bracketing IRFs are defined by envelopes above and below the nominal energy dependence of the effective area by linearly connecting differences of (10%, 5%, 20%) at  $\log_{10}(E/\text{MeV})$  of (2, 2.75, 4), respectively.

The imperfect knowledge of the true  $\gamma$ -ray morphology introduces a last source of error. We derived an estimate of the uncertainty on the shape of the source by using the best model obtained by TeV experiments and compared it to the best extension value obtained in this analysis. We did not compute this component for the sources where the GeV emission is clearly associated to a contamination by the pulsar.

We combined these various errors in quadrature to obtain our best estimate of the total systematic uncertainty at each energy and propagated through to the fit model parameters.

### 5. Results

Using the procedure described above, we detected 30 sources among the 58 PWNe candidates selected. For each of these detected sources, as explained in Section 4.4, we determined the best morphology by comparing the likelihood of our fit obtained under three different hypotheses: TeV shape, point-like source and extended source. The results of the spatial analysis are shown in Table 4, the last column summarizing the best shape found for each source. Once the best morphology found, we performed a spectral analysis whose results are reported in Tables 6 & 7, while upper limits on non-detections are presented in Tables 8 & 9.

#### 5.1. Extended sources detected above 10 GeV

Most sources are better described using the TeV morphology as a template. This is partly due to the 2 (3 for an extended source) additional degrees of freedom to take into

account but also to the low statistics above 10 GeV. Indeed, these sources have on average a low TS value or are at the limit of our extension threshold, such as HESS J1514-591.

Interestingly, 11 sources are better described using the morphology obtained at GeV energies using the LAT data, 5 of them being extended. Table 5 summarizes the spatial fits in such a case. The results presented here are consistent with Tables 3 and 4 of Lande et al. (2012). One can note that the agreement for HESS J1632–478 is not excellent. The difference in extension ( $0.35 \pm 0.06$  vs  $0.45 \pm 0.04$  in our analysis) certainly comes from the 3 additional 2FGL sources (2FGL J1631.7–4720c, 2FGL J1630.2–4752 and 2FGL J1632.4–4820c) in the model used by Lande et al. (2012). These sources were below our TS >25 threshold to add a source, and being unidentified, we found no physical reason to add them in our model.

HESS J1303–631 is a new extended source detected at GeV energies. However, Figure 2 shows that the *Fermi*-LAT excess observed for this source is likely due to 2 point-like sources (one associated with HESS J1303–631 and one associated with Kes 17 (Wu et al. 2011)) but the limited statistics at high energy does not allow us to separate them. When the region is fitted assuming the TeV morphology for HESS J1303–631 and a separate source for Kes 17, the latter hardly reaches TS  $\sim 20$  and is therefore too faint to be added to our model. Nevertheless, the difference between the true spectrum and the spectrum derived in this work will be included in the systematics on the flux taking into account the fact that we do not know the true morphology of the source.

## 5.2. Pulsars detected above 10 GeV

Only six sources are better described by a point-source model above 10 GeV than by a uniform disk or by the TeV template reported in Table 1: HESS J1708–443, MGRO J0632+17, MGRO J1908+06, MGRO J2019+37, MGRO J2228+61 and VER J0006+727. It is not a surprise to see in Figure 4 and Table 6 that these sources have a rather soft spectrum in comparison to the average index of TeV detected sources and that they are all coincident with bright  $\gamma$ -ray pulsars. As can be seen on Figure 5, the spectrum obtained above 10 GeV for these sources is in good agreement with the spectrum derived in the 2FGL Catalog released by the Fermi collaboration (Nolan et al. 2012). The  $\gamma$ -ray emission detected by the LAT above 10 GeV is therefore very likely due to the pulsar itself than to its associated PWN.

Three other sources are coincident with bright Fermi pulsars and present a very soft spectrum in agreement with the 2FGL Catalog as well: HESS J1418-609, MGRO J1958+2848 and MGRO J2031+41. Again, the  $\gamma$ -ray signal is very likely due to magnetospheric emission.

The faintness of these sources above 10 GeV and their almost point-like shape in the TeV energy range can explain why the improvement obtained using a point source model is not significant in comparison to the simple TeV morphology.

To study the contamination of these pulsars to our sources of interest, we used the procedure described in Section 4 but including the pulsars in our models of the regions. The spectra of *Fermi*-LAT pulsars are well characterized by exponentially cutoff power laws with photon indices near 1.5 and cutoff energies between 0.5 and 6 GeV (Abdo et al. in prep.c). As we selected the data above 10 GeV, we cannot fit the spectral parameters of these pulsars. Therefore we included them in our model assuming the fixed photon index, cutoff energy and normalization extracted from the 2FGL Catalog. It should be noted that some pulsars may deviate from the simple exponential cutoff power law above 10 GeV. This has been proposed for instance for the famous case of the Crab pulsar (Aliu et al. 2011, 2008). In such cases, our fit could still be contaminated by the pulsar, especially in the first energy interval (between 10 and 31.6 GeV).

Table 10 and Figures 5, 6 & 7 show the results of this new fit using the conventions presented in Table 2. As expected for the six point-like sources presented in Figure 5, the low energy part of the spectrum tends to disappear confirming that we only detected a pulsar emission. In the case of MGRO J1908+06, the detection is not significant anymore. To present conservative results, we derived the upper limits assuming the TeV shape of this source.

Figures 6 & 7 show the same behaviour for HESS J1418-609 confirming that the signal observed was dominated by the pulsar emission. In the case of HESS J1420-607 and HESS J1119-614, the spectra are now slightly harder but still in very good agreement with the previous ones, which is a good indication that we are mainly seeing the emission from the PWNe and not from their associated pulsars.

### 5.3. Detections of PWNe candidates

In this section we will describe the new PWNe candidates found in this analysis. We chose them by looking for signal connecting to the TeV spectrum and showing a hard spectrum. HESS J1420-607, HESS J1303-631, HESS J1356-645 & HESS J1119-614 were already proposed as PWNe by analyses at other wavelength. The detection of these sources by the *Fermi*-LAT tends to confirm this hypothesis.

HESS J1848-018, is classified as UNID. The detection presented in Table 6 shows a faint source with a soft spectrum. We will discuss this source in a PWN scenario.

*HESS J1420–607*

The complex of compact and extended radio/X-ray sources, called Kookaburra (Roberts et al. 1999), spans over about one square degree along the Galactic plane. It has been extensively studied to explain the EGRET source: 3EG J1420–6038/GeV J1417–6100 (Hartman et al. 1999). Within the North-East excess of this complex, labeled ‘K3’, was discovered the pulsar PSR J1420–6048, a young and energetic pulsar with period 68 ms, characteristic age of 13 kyr, and spin down energy of  $10^{37}$  erg s $^{-1}$  (D’Amico et al. 2001). Following X-ray observations by ASCA and later by *Chandra* and *XMM-Newton* revealed an extended X-ray emission around this pulsar identified as a potential PWN (Roberts et al. 2001; Ng et al. 2005). In the South-West side of the large Kookaburra complex lies a bright nebula exhibiting an extended hard X-ray emission, G313.1+0.1, called the ‘Rabbit’ (Roberts et al. 1999). This X-ray excess was also proposed as a plausible PWN contributing to the  $\gamma$ -ray emission detected by EGRET.

In the TeV energy range, the survey of the Galactic plane by H.E.S.S. revealed two very high energy sources in this region: HESS J1420–607 and HESS J1418–609 (Aharonian et al. 2006a). HESS J1420–607 is centered North of PSR J1420–6048 (nearby the K3 nebula), while HESS J1418–609 is coincident with the Rabbit nebula. More recently, *Fermi*-LAT detected pulsed  $\gamma$ -ray emission from PSR J1420–6048 and PSR J1418–6058, the latter being a new  $\gamma$ -ray pulsar found through blind frequency searches (Abdo et al. 2010f, 2009a). This new pulsar is coincident with an X-ray source in the Rabbit PWN and has a spin-down power high enough to power the TeV PWN candidate HESS J1418–609.

In our analysis, HESS J1420–607 is detected with a TS of 41 which corresponds to a significance of  $\sim 6\sigma$ . Figure 8 shows two smoothed counts map centered on the location of the K3 nebula represented by the crossed circle. The Galactic and the isotropic diffuses emission were subtracted in order to show the excesses coming from HESS J1420–607 (represented by the crossed circle) and HESS J1418–609 (represented by the crossed ellipse). The first counts map (Top) represents the excesses of the two sources above 10 GeV and the second (Bottom) represents the excesses above 30 GeV. One can see an apparent emission of the region of HESS J1418–609 close to HESS J1420–607 above 10 GeV. Therefore, above 10 GeV, the observed spectrum of HESS J1420–607 is potentially contaminated by the residual emission from HESS J1418–607. However, on the counts map above 30 GeV, the residual emission from HESS J1418–609 disappears. This confirms the soft spectral index and the pulsar behaviour of the emission coming from the region of HESS J1418–609.

With a TS of 41.2, the point source hypothesis does not significantly improve the likelihood of our fit in comparison to the TeV morphology (Gaussian of  $0.06^\circ$ ) presented in Aharonian et al. (2006a). Therefore, assuming the TeV shape, we found an integrated

flux  $F(10\text{--}316\text{ GeV}) = (3.2 \pm 0.9_{\text{stat}} \pm 1.0_{\text{syst}}) \times 10^{-10} \text{ ph cm}^{-2} \text{ s}^{-1}$ , a spectral index of  $\Gamma = 1.91 \pm 0.27_{\text{stat}} \pm 0.31_{\text{syst}}$  and an energy flux of  $G(10\text{--}316\text{ GeV}) = (23.1 \pm 5.7_{\text{stat}} \pm 6.3_{\text{syst}}) \times 10^{-12} \text{ erg cm}^{-2} \text{ s}^{-1}$ . In a second step, following the procedure presented in Section 5.2, we refitted the spectrum of HESS J1420–607 including PSR J1420–6048 in our model and fixing its spectral parameters found in the 2FGL Catalog. The fit of HESS J1420–607 leads a lower significance of  $5.6\sigma$  (TS=35.8, 2 d.o.f) with an integrated flux of  $F(10\text{--}316\text{ GeV}) = (3.4 \pm 0.9_{\text{stat}} \pm 1.0_{\text{syst}}) \times 10^{-10} \text{ ph cm}^{-2} \text{ s}^{-1}$  and an index of  $\Gamma = 1.80 \pm 0.29_{\text{stat}} \pm 0.32_{\text{syst}}$ .

Van Etten & Romani (2010) used a two-zone time dependent numerical model with constant injection luminosity to investigate the physical properties of HESS J1420–607. The authors injected relativistic particles following a power-law spectrum into the inner nebula zone, they evolved this spectrum over time and injected the resultant spectrum into the outer nebula zone. On Figure 9 we reported in solid line the results obtained for a hadronic + leptonic model assuming a low density environment ( $n \sim 1 \text{ cm}^{-3}$ ) and a magnetic field of  $\sim 12\mu\text{G}$  and  $\sim 9\mu\text{G}$  respectively in the inner and outer nebula. We also reported in dashed line the model proposed for a leptonic scenario assuming a magnetic field of  $\sim 12\mu\text{G}$  and  $\sim 8\mu\text{G}$  respectively in the inner and outer nebula. This magnetic field implied a lepton spectral break at  $\sim 100 \text{ TeV}$  after evolution in the inner nebula. More recently Kishishita et al. (2012) proposed a one-zone leptonic model assuming a power-law injection spectrum with an index of 2.3 with a cut-off around 40 TeV and a magnetic field around  $\sim 3\mu\text{G}$ . We represented this model in dotted line on the same figure. All these models show a good agreement with the observed spectrum.

However, as noted above, the low energy part of the *Fermi*-LAT spectrum may be contaminated by the pulsed emission from PSR J1420–6048. This implies that, with the current statistics, all models reproduce reasonably well the GeV and TeV data. A future *Fermi*-LAT off-pulse analysis of this pulsar performed with more statistics could help discriminate between the models.

### HESS J1356–645

HESS J1356–645 is a source detected in the TeV energy range by H.E.S.S. during the Galactic Plane Survey (Abramowski et al. 2011c). This extended source lies close to the pulsar PSR J1357–6429 which was discovered during the Parkes multibeam survey of the Galactic Plane (Camilo et al. 2004). Its high spin-down power of  $\dot{E} = 3.1 \times 10^{36} \text{ erg s}^{-1}$  makes it a good candidate to power a PWN. Archival radio and analysis of X-ray data from *ROSAT/SPPC* and *XMM/Newton* have revealed a faint extended structure coincident with the VHE emission (Abramowski et al. 2011c) providing another argument in favor of the

PWN scenario. In parallel, Lemoine-Goumard et al. (2011b) announced the detection of a pulsed signal from PSR J1357–6429 in the  $\gamma$ -ray and X-ray energy ranges using *Fermi*-LAT and *XMM-Newton* data. However, using 29 months of LAT data between 0.1 and 100 GeV, no counterpart to the TeV emission was found in the off pulse window of the pulsar.

The 16 additional months of observations by *Fermi*-LAT and the higher maximal energy used (316 GeV instead of 100 GeV) in our dataset now enables the detection of a faint counterpart to the TeV emission with a TS = 25.8 (4.7  $\sigma$  assuming 2 d.o.f.). Since the best GeV morphology does not improve the fit significantly, we used the TeV Gaussian of 0.17° (Abramowski et al. 2011c) for the spectral analysis and derived an integrated flux of  $F(10\text{--}316 \text{ GeV}) = (1.2 \pm 0.4_{\text{stat}} \pm 0.5_{\text{syst}}) \times 10^{-10} \text{ ph cm}^{-2} \text{ s}^{-1}$ , an energy flux of  $G(10\text{--}316 \text{ GeV}) = (16.8 \pm 6.9 \pm 6.8) \times 10^{-12} \text{ erg cm}^{-2} \text{ s}^{-1}$  and a hard spectral index of  $\Gamma = 0.99 \pm 0.39 \pm 0.40$ .

It should also be noted that, with its low energy cutoff at around 800 MeV in the *Fermi*-LAT energy range (Lemoine-Goumard et al. 2011b), PSR J1357–6429 is not significant anymore in the 10 to 316 GeV energy range. Therefore, we do not expect to see any changes in the spectral parameters when adding PSR J1357–6429 to the model of the region. This is verified in Table 10 as well as in Figure 10.

The combined GeV-TeV data as seen in Figure 10 provide new information concerning the spectral shape of the  $\gamma$ -ray emission. It is clearly visible in this figure that the *Fermi*-LAT spectral points nicely match the H.E.S.S. ones, proving that the GeV and the TeV emission have a common origin. Assuming that the  $\gamma$ -ray signal is coming from the PWN powered by PSR J1357–6429, Abramowski et al. (2011c) proposed a leptonic scenario (black curve) which provides an excellent fit of the new multi-wavelength data. This one-zone model is based on the evolution of an electron population injected following an exponentially cutoff power-law spectrum of index 2.5 and cut-off energy of 350 TeV. These electrons cool radiatively through of IC scattering on the Cosmic Microwave Background (CMB), Galactic infrared ( $T \sim 35\text{K}$  and  $350 \text{ K}$ ), optical ( $T \sim 4600\text{K}$ ) photons and through synchrotron emission in a magnetic field  $\sim 3.5\mu\text{G}$ .

The similarities between PSR J1357–6429 and the Vela pulsar and between their PWNe lead Abramowski et al. (2011c) to discuss a potential two leptonic-components emission. However, in the case of Vela-X, the "halo" is seen in the GeV and radio energy ranges and the "cocoon" in the TeV and X-ray energy ranges, while in the case of HESS J1356–645, a single lepton population explain the broad-band spectrum with reasonable parameters. However, unlike Vela-X, the current radio and X-ray data are very faint and do not provide any morphological constraints. Future multi-wavelength data are highly needed to better describe this source.

*HESS J1119–614*

450

451 During the Parkes multibeam pulsar survey, Camilo et al. (2000) discovered  
 452 PSR J1119–6127, a young ( $\tau = 1.6$  kyr) pulsar with a high spin-down power  $\dot{E} =$   
 453  $2.3 \times 10^{36}$  erg s $^{-1}$  within the supernova remnant G292.2–0.5. Using *Chandra* observations,  
 454 Gonzalez & Safi-Harb (2003) and Safi-Harb & Kumar (2008) revealed the presence of a faint  
 455 and compact PWN close to this pulsar. More recently, a TeV  $\gamma$ -ray source coincident with  
 456 PSR J1119–6127 and G292.2–0.5 was announced<sup>3</sup>.

457 Using the method described above, a faint signal consistent with the location of the  
 458 composite SNR G292.2–0.5 is detected with a TS of 27.3 (4.9  $\sigma$  with 2 d.o.f.). Since the  
 459 best GeV morphology does not improve the fit significantly, we used the TeV Gaussian  
 460 of  $0.05^\circ$  for the spectral analysis and derived an integrated flux of  $F(10 - 316 \text{ GeV}) =$   
 461  $(2.1 \pm 0.6_{stat} \pm 0.7_{syst}) \times 10^{-10}$  ph cm $^{-2}$  s $^{-1}$ , an energy flux of  $G(10-316 \text{ GeV}) = (10.4 \pm$   
 462  $3.9_{stat} \pm 4.0_{syst}) \times 10^{-10}$  erg cm $^{-2}$  s $^{-1}$  and a soft index of  $\Gamma = 2.15 \pm 0.37_{stat} \pm 0.38_{syst}$ .

463 Nevertheless, as can be seen on Figure 11 and in Table 10, these parameters are con-  
 464 taminated by a low energy component associated to PSR J1119–6127. Once the source  
 465 2FGL J1118.8–6128, associated with PSR J1119–6127, included in our model of the region,  
 466 this contamination decreases and the significance of our GeV source is now just above the  
 467 detection threshold that we fixed in Section 4.4, with TS = 16 (3.6  $\sigma$  with 2 d.o.f.). As can be  
 468 seen in Figure 11, the low energy point of the SED is now an upper limit. The best fit param-  
 469 eters in this hypothesis are an integrated flux of  $F(10-316 \text{ GeV}) = (1.5 \pm 0.6_{stat} \pm 0.6_{syst}) \times 10^{-10}$   
 470 ph cm $^{-2}$  s $^{-1}$  and an harder index of  $\Gamma = 1.80 \pm 0.48_{stat} \pm 0.50_{syst}$ .

471 Figure 11 shows the multi-wavelength SED of HESS J1119–614 along with the H.E.S.S.  
 472 points from Mayer (2010). The leptonic model proposed by Mayer (2010) (solid line) is a one-  
 473 zone model where accelerated electrons cool radiatively by IC scattering on CMB photons,  
 474 starlight photons radiated in the vicinity and photons radiated by dust and by synchrotron  
 475 losses. It implies an initial period of the pulsar  $P_0 = 21.4$  ms, an initial magnetic field inside  
 476 the PWN  $B_0 = 406.1 \mu\text{G}$  (leading to a current magnetic field of  $B \sim 32 \mu\text{G}$ ), a braking index of  
 477  $n=2.91$  (Camilo et al. 2000) and a conversion efficiency of spin-down power into relativistic  
 478 particles of  $\eta = 0.3$ . The model well matches the LAT and H.E.S.S. points.

479 The presence of PSR J1119-6127, the detection of a compact PWN in X-ray and the  
 480 leptonic model proposed by Mayer (2010) point toward the hypothesis in which the GeV-TeV  
 481 emission comes from the PWN inside G292.2–0.5. Furthermore, the parameters derived in  
 482 Mayer (2010) and the presence of jets in the X-ray data remind the case of MSH 15–52

---

<sup>3</sup>[http://cxc.harvard.edu/cdo/snr09/pres/DjannatiAtai\\_Arache\\_v2.pdf](http://cxc.harvard.edu/cdo/snr09/pres/DjannatiAtai_Arache_v2.pdf)



(Abdo et al. 2010a; Tamura et al. 1996).

### HESS J1303–631

HESS J1303–631 was serendipitously discovered in 2004 (Aharonian et al. 2005c) during an observation campaign of the pulsar binary system PSR B1259–63. It was originally classified as a ”dark” accelerator due to the lack of detected counterparts in radio and X-rays with *Chandra* (Mukherjee & Halpern 2005). Abramowski (in prep.) found only one plausible counterpart in the vicinity of HESS J1303-631 : PSR J1301–6305 with a spin-down power of  $\dot{E} = 1.70 \times 10^{36}$  erg s<sup>−1</sup>. The authors also presented the detection of a very weak X-ray PWN using *XMM-Newton* observations and the energy dependent morphology at TeV energies leading to the conclusion that HESS J1303-631 is an old PWNe offset from the pulsar powering it.

Figures 1 & 3 in Wu et al. (2011) show no significant emission coming from the location of HESS J1303–631 using 30 months of *Fermi*-LAT data between 1 and 20 GeV. With 15 months of additional data and a higher energy threshold, our analysis now provides a first detection of GeV emission coincident with the TeV source. Nevertheless as discussed in Section 5.1, Figure 2 shows that the detected emission might be contaminated by a source associated to Kes 17. Since we cannot separate these two sources using our strategy with the current statistics, we decided to take into account this effect of source confusion in our systematics on HESS J1303–631. Therefore, we ran the analysis again, adding a source spatially consistent with Kes 17 and we performed a second fit. The maximal variation is seen for the lower energy bin of the SED.

Assuming our best GeV morphology represented by a Disk shape of 0.5° (see Table 4), we obtained an integrated flux of  $F(10-316 \text{ GeV}) = (5.9 \pm 1.1_{\text{stat}} \pm 4.0_{\text{syst}}) \times 10^{-10}$  ph cm<sup>−2</sup> s<sup>−1</sup>, an energy flux of  $G(10-316 \text{ GeV}) = (43.5 \pm 10.0_{\text{stat}} \pm 23.4_{\text{syst}}) \times 10^{-12}$  erg cm<sup>−2</sup> s<sup>−1</sup> and an index of  $\Gamma = 1.71 \pm 0.19_{\text{stat}} \pm 0.39_{\text{syst}}$ . This hard index is in the range of values obtained for PWNe as seen with *Fermi*-LAT and is inconsistent with the spectral index of  $\sim 2.4$  derived by Wu et al. (2011) for Kes 17. This is a good evidence that the  $\gamma$ -ray emission above 10 GeV is dominated by the PWN candidate. As can be seen in Figure 12, even though the connection between the GeV and the TeV energy range is not perfect, there is little doubt that we have detected a counterpart to the TeV signal.

Figure 12 shows the SED of HESS J1303-631 together with the one-zone leptonic model proposed by Abramowski (in prep.). In this model, VHE  $\gamma$ -rays are created via IC scattering of electrons on the CMB photons, infrared and optical target photons being neglected. The

model reproduces the radio, X-ray and TeV data with an electron spectral index of  $1.8^{+0.1}_{-0.1}$ , a cut-off energy of  $31^{+5}_{-4}$  TeV, and an average magnetic field of  $1.4^{+0.2}_{-0.2}$   $\mu$ G. However, the flux predicted in the GeV energy range is well below the flux detected by the *Fermi*-LAT. This may be due to the absence of infrared and optical photon field or to contamination produced by Kes 17. A specific analysis is needed to conclude on the constraints that the *Fermi*-LAT could bring on the  $\gamma$ -ray emission of this source.

### HESS J1841–055

HESS J1841–055 was discovered during the H.E.S.S. Galactic Plane Survey (Aharonian et al. 2008b) and remained unidentified since then. The emission is highly extended and shows possibly three peaks suggesting that the TeV emission is composed of more than one source. Using *INTEGRAL* data, Sguera et al. (2009) proposed the high-mass X-ray binary HMXB system AX J1841.0–0536 as a potential counterpart, at least for a part of the emission. Tibolla (2011) proposed the association of HESS J1841–055 to an ancient PWN powered by PSR J1841–0524, PSR J1838–0549 or both as each pulsar taken independently would need an efficiency greater than 100% to power alone a potential PWN associated to the TeV source. More recently, the blind search detection of the new  $\gamma$ -ray pulsar PSR J1838–0537 with *Fermi*-LAT provided another good counterpart of the TeV source. Indeed, assuming a distance of 2 kpc, Pletsch et al. (2012) estimated that PSR J1838–0537 is sufficiently energetic to power the whole TeV source with a conversion efficiency of 0.5%, similar to other suggested pulsar/PWN associations (Hessels et al. 2008).

In this work, HESS J1841–055 is detected as a significantly extended source ( $TS_{ext}=38.3$ ) at a position consistent with the TeV source but with a larger extension ( $0.57^\circ$  with respect to  $0.41^\circ \times 0.25^\circ$  for the TeV source). However, the GeV best morphology does not significantly improve the fit compared to the TeV morphology ( $TS_{GeV/TeV}=13.0$ ,  $2.8\sigma$  with 3 d.o.f.). Therefore assuming the TeV shape, our best fit yielded an integrated flux of  $F(10-316 \text{ GeV}) = (9.3 \pm 1.9_{stat} \pm 3.9_{syst}) \times 10^{-10}$  for an energy flux of  $G(10-316 \text{ GeV}) = (79.6 \pm 16.0_{stat} \pm 19.1_{syst}) \times 10^{-12} \text{ erg cm}^{-2} \text{ s}^{-1}$  and a hard index of  $\Gamma = 1.56 \pm 0.20_{stat} \pm 0.32_{syst}$  consistent with the average value for PWNe detected by the *Fermi*-LAT.

As can be seen in Figure 13, the *Fermi*-LAT spectral points nicely match the H.E.S.S. ones, suggesting a common origin. The hard *Fermi*-LAT spectrum detected imply that a curvature must arise between the TeV energy range and the GeV energy range. This is typical of most PWNe detected by *Fermi*-LAT and H.E.S.S. which present IC emission peaking at few hundreds of GeV and would favor the PWN scenario. However, this source is extremely extended in both wavelengths and could be composed of several  $\gamma$ -ray sources. Follow-up

observations with IACTs and *Fermi*-LAT would be needed to unveil the real nature of HESS J1841–055.

### HESS J1848–018

HESS J1848–018 (*TeV J1848–017*) was discovered during the extended H.E.S.S. Galactic Plane Survey (Chaves 2010), in the direction of, but slightly offset from, the star forming region W43 (=G30.8-0.2). The TeV emission is characterized by a significant extension ( $0.32^\circ$ ) and a power-law spectrum of index  $\sim 2.8$  and an integrated flux above 1 TeV  $\sim 2 \times 10^{-12} \text{ cm}^{-2} \text{ s}^{-1}$ . The absence of energetic pulsar or SNR within  $0.5^\circ$  from HESS J1848–018 favor an association with the star forming region W43. No obvious counterparts were found in radio and X-ray in the region of the TeV source except the Wolf-Rayet star WR 121a.

Located  $0.2^\circ$  from the centroid of HESS J1848–028, WR 121a is a WN7 subtype star, in a binary system (Luque-Escamilla et al. 2011), associated with W43 and characterized by extreme mass loss rates. Chaves (2010) also proposed an association with the molecular clouds contained in W43. These molecular clouds could lead to the production of high energy  $\gamma$ -rays from the  $\pi^0$ -meson decays following  $p$ - $p$  collisions in the ambient gas.

In the GeV energy ranges, Tam et al. (2010) proposed an association with the spatially coincident source 0FGL J1848.6–0138. Lemoine-Goumard et al. (2011a) analyzed the *Fermi*-LAT data around HESS J1848–018 and found a  $3.7\sigma$  evidence for an extension ( $\sigma \sim 0.3^\circ$ ). This disfavors models in which the GeV emission would be produced by a pulsar alone. However, the statistic was not large enough to discriminate between one extended source and several point sources. Moreover, the spectrum was well described by a log-parabola and the SED was very similar to those obtained for most pulsars detected by *Fermi*-LAT. Therefore, the emission observed by the *Fermi*-LAT could be an extended source contaminated by a radio-faint pulsar not yet detected.

In our analysis, HESS J1848–018 is detected as a faint source and the GeV best morphology does not significantly improve the fit in comparison to the TeV morphology. Therefore assuming the TeV shape, our best fit yielded an integrated flux of  $F(10\text{-}316 \text{ GeV}) = (7.4 \pm 1.9_{\text{stat}} \pm 3.2_{\text{syst}}) \times 10^{-10} \text{ cm}^{-2} \text{ s}^{-1}$  for an energy flux of  $G(10\text{-}316 \text{ GeV}) = (30.0 \pm 10.1_{\text{stat}} \pm 16.5_{\text{syst}}) \times 10^{-12} \text{ erg cm}^{-2} \text{ s}^{-1}$  and an index of  $\Gamma = 2.46 \pm 0.80_{\text{stat}} \pm 0.52_{\text{syst}}$  consistent with the average value for PWNe detected by the *Fermi*-LAT.

On Figure 14, we reported the H.E.S.S. spectral points from Chaves (2010) and the radio points corresponding to the W43 central cluster from Luque-Escamilla et al. (2011).

It is important to note that the point obtained in our analysis, is consistent with the red dashed curve which represent the spectrum derived by Lemoine-Goumard et al. (2011a). It is not absolutely clear from this Figure if the GeV and TeV spectra have a common or a distinct origin and future multi-wavelength data would be needed to discriminate between the Pulsar/PWN and massive star formation region and conclude on the nature of HESS J1848–018.

#### 5.4. Constraints obtained from non-detections

This section will present the sources for which the emission was not significant but for which the upper limits show an interesting behaviour to bring new constraints on the models.

##### *HESS J1026–582*

HESS J1026–582 is a source discovered by H.E.S.S. during a new analysis of the region of HESS J1023–577 (Abramowski et al. 2011d). Abramowski et al. (2011d) have shown that the emission coming from this region could be splitted into two independent sources. While HESS J1023–577 is located close to PSR J1022–5746, the authors proposed an association between HESS J1026–582 and PSR J1028–5819, a pulsar detected by the Parkes Radio telescope Keith et al. (2008). The proximity of the pulsar suggested a PWN scenario to explain the VHE emission. This hypothesis is consolidated by the spin-down power energy of PSR J1028–5819,  $\dot{E} = 8.43 \times 10^{35} \text{ erg s}^{-1}$  (Abdo et al. 2009b), which is high enough to power a PWN. Mignani et al. (2012) compared the X-ray marginal emission observed in Suzaku data to a PWN scenario and conclude on a possible future detection. However, follow-up observations with *XMM-Newton* and *Chandra* are needed to confirm this detection.

No significant GeV emission coming from the location of the TeV excess was detected in our analysis. The very low TS value of 1.0 with an integrated flux below  $1.6 \times 10^{-10} \text{ ph cm}^{-2} \text{ s}^{-1}$  (see Tables 8 & 9) give few hope for a future detection of this source by the LAT. The upper limits presented on Figure 15 show that a curvature is needed between the TeV and the GeV energy range. This suggests an IC peak at energies higher than 100 GeV consistent with *Fermi*-LAT observations of other PWNe. However, the lack of multi-wavelength data (especially in radio and X-ray), prevent any conclusion on this source.

### HESS J1458–608

PSR J1459–60 (Abdo et al. 2010f) is an energetic and old pulsar with a spin-down power of  $\dot{E} = 9.2 \times 10^{35} \text{ erg s}^{-1}$ , high enough to power a PWN, and a characteristic age of 64 kyr. X-ray observations with *Swift* (Ray et al. 2011) and *Suzaku* (Kanai 2007) yielded the discovery of an X-ray counterpart to PSR J1459–60. HESS J1458–608, was discovered 9.6′ from PSR J1459–60 using H.E.S.S. data after a dedicated observation (de los Reyes et al. 2012) triggered by marginal detection in the 2004 Galactic Plane Survey. The proximity to the pulsar and the extension of HESS J1458–608 suggested that both object could be related in a PSR/PWN scenario. In this case, the lack of observable radio and X-ray emission could be explained by the age of the system.

In our work HESS J1458–608 was not significantly detected above 10 GeV (TS = 12.3) with an integrated flux below  $2.5 \times 10^{-10} \text{ ph cm}^{-2} \text{ s}^{-1}$ . Furthermore, Table 9 shows that the observed marginal emission comes from the energy bin between 10 and 31 GeV. This means that the emission is more likely due to the pulsar than linked to the TeV source. Figure 16 shows that even taking into account the pulsar in our model of the region, the SED is still contaminated at low energy. Nevertheless, the upper limits computed in the energy bins between 31 and 316 GeV, where no pulsar emission is expected anymore, show that a change in the slope of the spectrum is needed between the TeV and the GeV component. This could be consistent with an IC peak above 100 GeV which is the range observed for the PWN observed with the *Fermi*-LAT.

### HESS J1626–490

HESS J1626–490 is another unidentified source detected during the H.E.S.S. Galactic Plane Survey (Aharonian et al. 2008b). In their search for counterparts, Eger et al. (2011) found no X-ray source fulfilling the energetic requirement to explain the TeV emission using *XMM-Newton* observations. However, the author suggested that a hadronic scenario based on the interaction of the SNR G335.2+00.1 with a  $^{12}\text{CO}$  molecular cloud could explain the TeV emission. This hypothesis is supported by a density depression in H I which could be explained by a recent event such as a SNR.

With a TS of 1.5, HESS J1626–490 is not significantly detected in our analysis. The model presented in Eger et al. (2011) and reported on Figure 17 reproduces the H.E.S.S. SED and is clearly below the upper limits obtained using *Fermi*-LAT data. Only a radio or/and X-ray detection of synchrotron emission from a PWN or the detection of a pulsar could call this model into question.

# HESS J1813–178

HESS J1813-178 was discovered during the H.E.S.S. Survey of the Inner Galaxy (Aharonian et al. 2005a) and remained unidentified until the discovery of the SNR G12.8-0.0 (Brogan et al. 2005) in the radio band. Using *XMM-Newton* observations, Funk et al. (2007b) detected a complex morphology composed of a point-like source and an extended nebula. The morphological and spectral resemblance of the central object with a PWN, lead Funk et al. (2007b) to propose a PWN/SNR scenario to describe the X-ray sources. This hypothesis was strengthened by the discovery of PSR J1813–1749 (Gotthelf & Halpern 2009), one of the most energetics pulsar in our Galaxy with a spin-down power of  $\dot{E} = 5.6 \times 10^{37}$  erg s<sup>−1</sup>. However, the nature of the TeV emission remains unclear as both the SNR or the PWN could produce emission at these energies.

Our analysis yielded a TS of 2.5 with an upper limit on the integrated flux of  $2.4 \times 10^{-10}$  ph cm<sup>−2</sup> s<sup>−1</sup> assuming the TeV morphology as spatial shape. Figure 18 shows the multi-wavelength SED of HESS J1813–178. The red and blue points corresponds to the *Fermi*-LAT and H.E.S.S. spectral points. The green and magenta show respectively the X-ray and radio points derived using the PWN region in Figure 18 (Top) and the SNR region in Figure 18 (Bottom). The upper limits derived using the procedure described in Section 4 show that the spectrum of HESS J1813–178 cannot be flat between the TeV and the GeV energy ranges and suggest a peak with an energy cutoff located between the two energy ranges.

Funk et al. (2007b) and Fang & Zhang (2010) investigated a leptonic model, in which the core X-ray and VHE  $\gamma$ -ray emission are associated. Both take into account IC scattering on CMB, infrared and near infrared photon fields and synchrotron emission produced with a rather low magnetic field ( $B \sim 7 \mu\text{G}$ ). The main difference between these two models lies in the injected electron population which follows power-law spectrum with an index of 2.0 in Funk et al. (2007b) and a maxwellian + power-law tail spectrum (Spitkovsky 2008) with an index of 2.4 in Fang & Zhang (2010).

Both also investigated the possibility for the TeV energy to be created by the SNR shell. We overlaid in solid line on Figure 18 (Top) the model proposed by Funk et al. (2007b) assuming a hadronic scenario. The main differences between these two models lies in the injected protons and electron populations which follows power-law spectrum with an index of 2.1 in Funk et al. (2007b) and is computed in a semi-analytical nonlinear model in Fang & Zhang (2010).

The upper limits derived in our analysis rejected one of the two model proposed in each hypothesis. Therefore, no conclusion can be reached on the nature of the TeV emission, being a PWN or a SNR. However, at the light of the different model discussed on can exclude

a model assuming a maxwellian + power-law tail injection spectrum with an index of 2.4 assuming the same parameters than those derived in Fang & Zhang (2010) in the case where the TeV emission comes from the PWN core. These upper limits also constrain the hadronic model by rejecting a power-law injection spectrum of 2.1 with the parameters proposed by Funk et al. (2007b). Therefore, whatever the origin of the  $\gamma$ -ray emission, the injected spectrum of the primary electron and protons need to be relatively hard to reproduce the *Fermi*-LAT upper limits ( $\Gamma \leq 2.1$ ).

## 6. Discussion

In this section we investigate the correlations between the pulsar/PWN system parameters (age, spin-down power) and the flux in GeV, TeV and X-ray energy ranges. Tables 11 & 12 summarize the pulsar characteristics and the multi-wavelength informations on each source. To allow the comparison between Mattana et al. (2009) and our work, we studied the expected differences between the TeV energy range and the GeV energy range. We assumed that the TeV and the GeV emission coming from these sources were the two sides of the IC emission produced by the same population of electrons and we studied the spectral shape of this IC peak.

Figure 19 shows the TeV spectral index as a function of the GeV spectral index. This figure perfectly show that sources having a hard index in the GeV energy range ( $\Gamma < 2$ ) have a harder index in the TeV energy range as well, confirming that we may be detecting the two sides of the same  $\gamma$ -ray peak.

To quantify the expected differences seen in GeV and TeV, we estimated the average energy of the IC peak. For that, we assumed that the  $\gamma$ -ray energy spectra can be described by a log-normal representation (Equation 9) as done in Albert et al. (2008).

$$\frac{dN}{dE} = N_0 \times \left( \frac{E}{E_0} \right)^{-\left[ \alpha + \beta \times \log\left( \frac{E}{E_b} \right) \right]} \quad (9)$$

We fixed  $E_0$  at 300 GeV and  $\beta$  at 0.2 and fitted the prefactor  $N_0$ , the index  $\alpha$  and the energy break  $E_b$  using our *Fermi*-LAT results and the TeV spectra. Then, we defined the energy of the peak ( $E_{peak}$ ) as the energy at which the energy flux of the modeled peak is maximal. This also corresponds to Equation 10.

$$\alpha + \beta \times \log\left( \frac{E}{E_b} \right) = 2.0 \quad (10)$$

The fit results as well as the peak position are presented in Table 13. Figure 20 presents the TeV spectral index as a function of the energy of the maximum of the IC peak. This figure highlights a correlation between the TeV spectral index and the peak energy. The TeV index increases with decreasing peak energy except for HESS J1632–472. This means that the closer the energy peak is from the GeV energy range, the softer the index will be in the TeV energy range, which is consistent with our log parabola model. The exception of HESS J1632–472 could be due to the uncertainties due to the presence of neighbouring sources. As discussed in Section 5.1, three sources are detected at lower energies (Nolan et al. 2012). These sources are not significantly detected above 10 GeV. It means that these sources can contaminate the low energy of the spectrum derived in this analysis and therefore artificially decrease the fitted energy of the maximum of the IC peak.

Figure 21 shows the peak energy as a function of the pulsar characteristic age. This Figure presents no obvious correlation between the energy of the peak and the pulsar characteristic age as it would be expected from evolution models and presented in Mayer et al. (2012). However, it is important to note that this Figure suffers two main biases. First, the characteristic age may not be a good age estimator for the PWN. For instance, MSH 15–52 is a known case where two ages are proposed, either the characteristic age of the pulsar 1.7 kyr or an age between 20 and 40 kyr as suggested by the size and general appearance of the SNR (Gvaramadze 2001). Second, our sample is relatively restricted to PWNe with a characteristic age close to 10 kyr, except for MSH 15–52 and HESS J1119–614. In this context it is not surprising that no correlation is found between  $E_{peak}$  and the characteristic age.

From Table 13 we derived the mean parameters corresponding to our sources of interest :  $\bar{\alpha} = 2.1 \pm 0.2$  and  $\log_{10} (E_{peak}^-) = 5.7 \pm 0.6$ . Using these parameters we computed the mean expected ratio between the GeV and the TeV fluxes :  $\bar{R} = 1.9 \pm xx$ . Figure 22 presents the ratio of the luminosity in the GeV energy range over the luminosity found in the TeV energy range summarized in Table 12. We represented the mean ratio found between the GeV and TeV energy ranges as a dashed line. This figure shows that no sources are located at more than  $2\sigma$  from this mean ratio except HESS J1804–216. Ajello et al. (2012) studied the link between the TeV and the GeV emission and concluded that a theory assuming the energy-dependent diffusion of particles accelerated in the SNR is more likely than a PWN scenario. Therefore, the emission is not clearly associated to an IC peak and could have an hadronic origin, which would explain why this source is an outlier.

As described in Mattana et al. (2009), the  $\gamma$ -ray and the X-ray luminosities are expected to decrease with time, but the evolution should be different following the age and the pulsar spin-down power. From Table 12 we represent the ratio of the  $\gamma$ -ray luminosity over the X-



ray luminosity as a function of the age and as a function of the pulsar spin-down power. We also represented respectively in solid and dashed line the relations derived in Mattana et al. (2009) multiplied by  $\bar{R}$  for the whole sample of sources and for the sources clearly identify to PWNe.

This figure show two correlations : one between the fluxes ratio and the spin-down power and the other between the same flux ratio and the characteristic age. These correlations are expected since the magnetic field depends on these two parameters. However, for each correlation, a sample of four upper limits consistent with fluxes measured at TeV energies are well below the correlation relations derived by Mattana et al. (2009). The overall agreement with the relations proposed by Mattana et al. (2009) is relatively good but it can already be predicted that the GeV points will have a larger dispersion once these sources will be detected.

It seems clear from these figures that *Fermi*-LAT mainly detect young and middle-aged PWNe (1-30 kyr) around energetic pulsars with a spin-down power between  $10^{36}$  and  $10^{37}$  erg  $s^{-1}$ . Figure 24 shows the  $\gamma$ -ray luminosity of the PWN as a function of the pulsar spin-down power assuming the distances summarized in Table 11. The solid, dashed and dot dashed lines respectively show the lines where the luminosity corresponds to 100%, 10% and 1% of the spin-down power. Full and hollow markers respectively represent sources for which the TeV emission is clearly associated to a PWNe and sources for which the association is less clear. Sources with a pulsar-like spectrum are represented in green pentagons. For all sources in Table 2 the pulsar are included in the models. Among the detected sources, eight show a  $\gamma$ -ray efficiency below 1% and five are consistent within uncertainties with an efficiency between 1 and 10 %. HESS J1303–631 is also consistent with an efficiency of 100% assuming a distance of 15 kpc. This can be due to the large uncertainty on the distance measured which can lead to a factor 3 between the estimated distance and the true distance and by the contamination by Kes 17 as discussed in Section 5.1. Six upper limits on the luminosity of TeV sources clearly associated to PWNe are well below an efficiency of 1%.

## 7. Conclusion

45 months of *Fermi*-LAT observations have been used to look for counterparts to the TeV sources potentially associated to PWNe. Among the 58 sources studied, 31 have been detected. Among these 31, 23 were also detected in Abdo et al. (in prep.a) and 15 in Neronov & Semikoz (2012). Interestingly five new sources are detected in our analysis (HESS J1119–614, HESS J1303–631, HESS J1356–645, HESS J1841–055 and HESS J1848–018). We analyzed the morphology of the 31 sources detected and found that for 19 of them the

GeV shape did not significantly improve the fit in comparison to the TeV shape. For five sources, we found a significant extension larger than the TeV morphology. Six sources are well fitted by a point-like source; all of them have a high index and are probably associated to pulsars emitting above 10 GeV.

Since Ackermann et al. (2011) the number of PWNe detected by *Fermi*-LAT increased to 5 (Crab Nebula, Vela-X, MSH 15–52, HESS J1640–465, HESS J1825–137). This number must be considered with the growing number of PWNe candidates (HESS J1023–577, HESS J1119–614, HESS J1303–631, HESS J1356–645, HESS J1420–607, HESS J1841–055, HESS J1848–018 and HESS J1857+026). These PWNe and PWNe candidates are powered by young (between 1 and 30 kyr) and powerful pulsars (spin down power between  $10^{36}$  and  $10^{39}$  erg s<sup>−1</sup> with an efficiency below 10%).

The *Fermi* LAT Collaboration acknowledges generous ongoing support from a number of agencies and institutes that have supported both the development and the operation of the LAT as well as scientific data analysis. These include the National Aeronautics and Space Administration and the Department of Energy in the United States, the Commissariat à l’Energie Atomique and the Centre National de la Recherche Scientifique / Institut National de Physique Nucléaire et de Physique des Particules in France, the Agenzia Spaziale Italiana and the Istituto Nazionale di Fisica Nucleare in Italy, the Ministry of Education, Culture, Sports, Science and Technology (MEXT), High Energy Accelerator Research Organization (KEK) and Japan Aerospace Exploration Agency (JAXA) in Japan, and the K. A. Wallenberg Foundation, the Swedish Research Council and the Swedish National Space Board in Sweden.

Additional support for science analysis during the operations phase is gratefully acknowledged from the Istituto Nazionale di Astrofisica in Italy and the Centre National d’Études Spatiales in France.

This research has made use of `pywcsgrid2`, an open-source plotting package for Python<sup>4</sup>. The authors acknowledge the use of `HEALPix`<sup>5</sup> (Górski et al. 2005).

The authors acknowledge the use of the TeV catalog website<sup>6</sup> provided by the university of Chicago.

The authors acknowledge the use of the *Australia Telescope National Facility* pulsar

---

<sup>4</sup><http://leejjoon.github.com/pywcsgrid2/>

<sup>5</sup><http://healpix.jpl.nasa.gov/>

<sup>6</sup><http://tevcat.uchicago.edu/>

<sup>806</sup> catalog<sup>7</sup>.

---

<sup>7</sup><http://www.atnf.csiro.au/people/pulsar/psrcat/>

## REFERENCES

- Abdo, A. A., Ackermann, M., Ajello, M., Allafort, A., Asano, K., Baldini, L., Ballet, J., & Fermi LAT Collaboration. in prep.a, ApJ
- . in prep.b, ApJ
- . in prep.c, ApJ
- Abdo, A. A., et al. 2007a, ApJ, 658, L33
- . 2007b, ApJ, 664, L91
- . 2009a, Science, 325, 840
- . 2009b, ApJ, 695, L72
- . 2009c, ApJ, 706, 1331
- . 2009d, Phys. Rev. D, 80, 122004
- . 2009e, ApJ, 696, 1084
- . 2009f, ApJ, 700, L127
- . 2010a, ApJ, 714, 927
- . 2010b, ApJS, 188, 405
- . 2010c, ApJ, 708, 1254
- . 2010d, ApJ, 713, 146
- . 2010e, ApJ, 722, 1303
- . 2010f, ApJS, 187, 460
- Abramowski, A., et al. 2011a, A&A, 531, A81
- . 2011b, A&A, 528, A143
- . 2011c, A&A, 533, A103
- . 2011d, A&A, 525, A46
- . 2012a, A&A, 537, A114

- 831 —. 2012b, ArXiv e-prints
- 832 Abramowski, A., A. F. A. F. A. A. G. A. G. B. S. f. in prep., A&A
- 833 Acciari, V. A., et al. 2010, ApJ, 719, L69
- 834 Acero, F., Djannati-Ataï, A., Förster, A., Gallant, Y., Renaud, M., & for the H. E. S. S. col-  
835 laboration. 2012, ArXiv e-prints
- 836 Acero, F., et al. 2011, A&A, 525, A45
- 837 Ackermann, M., et al. 2011, ApJ, 726, 35
- 838 Aharonian, F., et al. 2005a, Science, 307, 1938
- 839 —. 2005b, A&A, 435, L17
- 840 —. 2005c, A&A, 439, 1013
- 841 —. 2006a, A&A, 456, 245
- 842 —. 2006b, A&A, 460, 365
- 843 —. 2006c, A&A, 457, 899
- 844 —. 2006d, ApJ, 636, 777
- 845 —. 2007, A&A, 472, 489
- 846 —. 2008a, A&A, 484, 435
- 847 —. 2008b, A&A, 477, 353
- 848 —. 2009, A&A, 499, 723
- 849 Ajello, M., et al. 2012, ApJ, 744, 80
- 850 Albert, J., et al. 2008, ApJ, 674, 1037
- 851 Aleksić, J., et al. 2012, Astroparticle Physics, 35, 435
- 852 Aliu, E., et al. 2008, Science, 322, 1221
- 853 —. 2011, Science, 334, 69
- 854 Aliu, E. e. a. 2011, ArXiv e-prints

- Atkins, R., et al. 2004, *ApJ*, 608, 680
- Atwood, W. B., et al. 2009, *ApJ*, 697, 1071
- Balbo, M., Saouter, P., Walter, R., Pavan, L., Tramacere, A., Pohl, M., & Zurita-Heras, J.-A. 2010, *A&A*, 520, A111
- Bartoli, B., et al. 2012, *ApJ*, 745, L22
- Blum, R. D., Daminieli, A., & Conti, P. S. 1999, *AJ*, 117, 1392
- Brogan, C. L., Gaensler, B. M., Gelfand, J. D., Lazendic, J. S., Lazio, T. J. W., Kassim, N. E., & McClure-Griffiths, N. M. 2005, *ApJ*, 629, L105
- Brun, F., de Naurois, M., Hofmann, W., Carrigan, S., Djannati-Ataï, A., Ohm, S., & for the H. E. S. S. Collaboration. 2011, *ArXiv e-prints*
- Buehler, R., et al. 2012, *ApJ*, 749, 26
- Camilo, F., Kaspi, V. M., Lyne, A. G., Manchester, R. N., Bell, J. F., D’Amico, N., McKay, N. P. F., & Crawford, F. 2000, *ApJ*, 541, 367
- Camilo, F., Ransom, S. M., Gaensler, B. M., Slane, P. O., Lorimer, D. R., Reynolds, J., Manchester, R. N., & Murray, S. S. 2006, *ApJ*, 637, 456
- Camilo, F., et al. 2004, *ApJ*, 611, L25
- Caswell, J. L., McClure-Griffiths, N. M., & Cheung, M. C. M. 2004, *MNRAS*, 352, 1405
- Chaves, R. 2010, *PhD Thesis*
- Chaves, R. C. G., Renaud, M., Lemoine-Goumard, M., & Goret, P. 2008, in *American Institute of Physics Conference Series*, Vol. 1085, American Institute of Physics Conference Series, ed. F. A. Aharonian, W. Hofmann, & F. Rieger, 372–375
- D’Amico, N., et al. 2001, *ApJ*, 552, L45
- de Jager, O. C., & Djannati-Ataï, A. 2009, in *Astrophysics and Space Science Library*, Vol. 357, *Astrophysics and Space Science Library*, ed. W. Becker, 451
- de Jager, O. C., Slane, P. O., & LaMassa, S. 2008, *ApJ*, 689, L125
- de Jager, O. C., et al. 2009, *ArXiv e-prints*

- 881 de los Reyes, R., Zajczyk, A., Chaves, R. C. G., & for the H. E. S. S. collaboration. 2012,  
882 ArXiv e-prints
- 883 de Naurois, M. 2011, ArXiv e-prints
- 884 Djannati-Ataï, A., de Jager, O. C., Terrier, R., & et al. 2008, in International Cosmic Ray  
885 Conference, Vol. 2, International Cosmic Ray Conference, 823–826
- 886 Dodson, R., Legge, D., Reynolds, J. E., & McCulloch, P. M. 2003, ApJ, 596, 1137
- 887 Duncan, A. R., Stewart, R. T., Haynes, R. F., & Jones, K. L. 1995, MNRAS, 277, 36
- 888 Eger, P., Rowell, G., Kawamura, A., Fukui, Y., Rolland, L., & Stegmann, C. 2011, in  
889 International Cosmic Ray Conference, Vol. 7, International Cosmic Ray Conference,  
890 44
- 891 Ergin, T., Nuss, E., & Fermi-LAT collaboration. in prep., ApJ?
- 892 Esposito, P., Tiengo, A., de Luca, A., & Mattana, F. 2007, A&A, 467, L45
- 893 Falleti, L., Nuss, E., Johann Cohen-tanugi, J., Caliendo, A., & Fermi-LAT collaboration.  
894 in prep., A&A
- 895 Fang, J., & Zhang, L. 2010, ApJ, 718, 467
- 896 Funk, S., Hinton, J. A., Pühlhofer, G., Aharonian, F. A., Hofmann, W., Reimer, O., &  
897 Wagner, S. 2007a, ApJ, 662, 517
- 898 Funk, S., et al. 2007b, A&A, 470, 249
- 899 Gonzalez, M., & Safi-Harb, S. 2003, ApJ, 591, L143
- 900 Górski, K. M., Hivon, E., Banday, A. J., Wandelt, B. D., Hansen, F. K., Reinecke, M., &  
901 Bartelmann, M. 2005, ApJ, 622, 759
- 902 Gotthelf, E. V., & Halpern, J. P. 2009, ApJ, 700, L158
- 903 Gotthelf, E. V., Halpern, J. P., Terrier, R., & Mattana, F. 2011, ApJ, 729, L16
- 904 Griffith, M. R., & Wright, A. E. 1993, AJ, 105, 1666
- 905 Grondin, M.-H., Fermi-LAT collaboration, & Pulsar Timing Consortium. in prep., ApJ
- 906 Grondin, M.-H., et al. 2011, ApJ, 738, 42

- 907 Gvaramadze, V. V. 2001, *A&A*, 374, 259
- 908 Hall, T. A., et al. 2003, *ApJ*, 583, 853
- 909 Halpern, J. P., Gotthelf, E. V., & Camilo, F. 2012, *ApJ*, 753, L14
- 910 Hartman, R. C., et al. 1999, *ApJS*, 123, 79
- 911 Hessels, J. W. T., Roberts, M. S. E., Ransom, S. M., Kaspi, V. M., Romani, R. W., Ng,  
912 C.-Y., Freire, P. C. C., & Gaensler, B. M. 2004, *ApJ*, 612, 389
- 913 Hessels, J. W. T., et al. 2008, *ApJ*, 682, L41
- 914 Hofverberg, P. 2011, in *International Cosmic Ray Conference*, Vol. 7, *International Cosmic*  
915 *Ray Conference*, 247
- 916 Hofverberg, P., Chaves, R. C. G., Méhault, J., de Naurois, M., & for the H. E. S. S. Collab-  
917 oration. 2011, *ArXiv e-prints*
- 918 Hoppe, S. 2008, in *International Cosmic Ray Conference*, Vol. 2, *International Cosmic Ray*  
919 *Conference*, 579–582
- 920 James, F., & Roos, M. 1975, *Comput. Phys. Commun.*
- 921 Johnston, S., Manchester, R. N., Lyne, A. G., Kaspi, V. M., & D’Amico, N. 1995, *A&A*,  
922 293, 795
- 923 Kanai, Y. 2007, phd thesis
- 924 Keith, M. J., Johnston, S., Kramer, M., Weltevrede, P., Watters, K. P., & Stappers, B. W.  
925 2008, *MNRAS*, 389, 1881
- 926 Kerr, M. 2011, *ArXiv e-prints*
- 927 Kishishita, T., Bamba, A., Uchiyama, Y., Tanaka, Y., & Takahashi, T. 2012, *ApJ*, 750, 162
- 928 Kothes, R., Uyaniker, B., & Pineault, S. 2001, *ApJ*, 560, 236
- 929 Kramer, M., et al. 2003, *MNRAS*, 342, 1299
- 930 Lande, J., et al. 2012, *ArXiv e-prints*
- 931 Leahy, D. A., Tian, W., & Wang, Q. D. 2008, *AJ*, 136, 1477
- 932 Lemiére, A., Slane, P., Gaensler, B. M., & Murray, S. 2009, *ApJ*, 706, 1269



- 933 Lemoine-Goumard, M., Ferrara, E., Grondin, M.-H., Martin, P., & Renaud, M. 2011a,  
934 Mem. Soc. Astron. Italiana, 82, 739
- 935 Lemoine-Goumard, M., et al. 2011b, A&A, 533, A102
- 936 Lorimer, D. R., et al. 2006, MNRAS, 372, 777
- 937 Luque-Escamilla, P. L., Muñoz-Arjonilla, A. J., Sánchez-Sutil, J. R., Martí, J., Combi, J. A.,  
938 & Sánchez-Ayaso, E. 2011, A&A, 532, A92
- 939 Manchester, R. N., Hobbs, G. B., Teoh, A., & Hobbs, M. 2005, VizieR Online Data Catalog,  
940 7245, 0
- 941 Manchester, R. N., et al. 2001, MNRAS, 328, 17
- 942 Mattana, F., et al. 2009, ApJ, 694, 12
- 943 Mattox, J. R., et al. 1996, ApJ, 461, 396
- 944 Mayer, M. 2010, Diplomarbeit : Erlangen Centre for Astroparticle Physics Physikalisches  
945 Institut 2 Lehrstuhl für Physik Friedrich-Alexander-Universität Erlangen-Nürnberg
- 946 Mayer, M., Brucker, J., Jung, I., Valerius, K., & Stegmann, C. 2012, ArXiv e-prints
- 947 McArthur, S. e. a. 2011, ArXiv e-prints
- 948 Mignani, R. P., Razzano, M., Esposito, P., De Luca, A., Marelli, M., Oates, S. R., & Saz-  
949 Parkinson, P. 2012, A&A, 543, A130
- 950 Mukherjee, R., & Halpern, J. P. 2005, ApJ, 629, 1017
- 951 Murphy, T., Mauch, T., Green, A., Hunstead, R. W., Piestrzynska, B., Kels, A. P., &  
952 Sztajer, P. 2007, MNRAS, 382, 382
- 953 Neronov, A., & Semikoz, D. V. 2012, Phys. Rev. D, 85, 083008
- 954 Ng, C.-Y., Roberts, M. S. E., & Romani, R. W. 2005, ApJ, 627, 904
- 955 Nolan, P. L., et al. 2012, ApJS, 199, 31
- 956 Pineault, S., Landecker, T. L., Madore, B., & Gaumont-Guay, S. 1993, AJ, 105, 1060
- 957 Pletsch, H. J., et al. 2012, ApJ, 755, L20
- 958 Ray, P. S., et al. 2011, ApJS, 194, 17

- 959 Renaud, M., Goret, P., & Chaves, R. C. G. 2008, in American Institute of Physics Con-  
960 ference Series, Vol. 1085, American Institute of Physics Conference Series, ed. F. A.  
961 Aharonian, W. Hofmann, & F. Rieger, 281–284
- 962 Roberts, M. S. E., Romani, R. W., & Johnston, S. 2001, *ApJ*, 561, L187
- 963 Roberts, M. S. E., Romani, R. W., Johnston, S., & Green, A. J. 1999, *ApJ*, 515, 712
- 964 Rousseau, R., et al. 2012, *A&A*, 544, A3
- 965 Safi-Harb, S., & Kumar, H. S. 2008, *ApJ*, 684, 532
- 966 Saz Parkinson, P. M., et al. 2010, *ApJ*, 725, 571
- 967 Seward, F. D., Kearns, K. E., & Rhode, K. L. 1996, *ApJ*, 471, 887
- 968 Sguera, V., Romero, G. E., Bazzano, A., Masetti, N., Bird, A. J., & Bassani, L. 2009, *ApJ*,  
969 697, 1194
- 970 Sheidaei, F., Djannati-Ataï, A., Gast, H., & for the HESS Collaboration. 2011, ArXiv e-prints
- 971 Slane, P., Castro, D., Funk, S., Uchiyama, Y., Lemièrre, A., Gelfand, J. D., & Lemoine-  
972 Goumard, M. 2010, *ApJ*, 720, 266
- 973 Spitkovsky, A. 2008, *ApJ*, 682, L5
- 974 Sun, M., Wang, Z.-R., & Chen, Y. 1999, *ApJ*, 511, 274
- 975 Tam, P. H. T., Wagner, S. J., Tibolla, O., & Chaves, R. C. G. 2010, *A&A*, 518, A8
- 976 Tamura, K., Kawai, N., Yoshida, A., & Brinkmann, W. 1996, *PASJ*, 48, L33
- 977 Temim, T., Slane, P., Gaensler, B. M., Hughes, J. P., & Van Der Swaluw, E. 2009, *ApJ*, 691,  
978 895
- 979 Terrier, R., Mattana, F., Djannati-Atai, A., Marandon, V., Renaud, M., & Dubois, F. 2008,  
980 in American Institute of Physics Conference Series, Vol. 1085, American Institute of  
981 Physics Conference Series, ed. F. A. Aharonian, W. Hofmann, & F. Rieger, 312–315
- 982 Tibolla, O. 2011, in International Cosmic Ray Conference, Vol. 6, International Cosmic Ray  
983 Conference, 197
- 984 Trimble, V. 1973, *PASP*, 85, 579
- 985 Ubertini, P., et al. 2005, *ApJ*, 629, L109

- 986 Uchiyama, Y. 2011, ArXiv e-prints
- 987 van den Bergh, S., & Kamper, K. W. 1984, ApJ, 280, L51
- 988 van der Hucht, K. A. 2001, VizieR Online Data Catalog, 3215, 0
- 989 Van Etten, A., & Romani, R. W. 2010, ApJ, 711, 1168
- 990 Verbiest, J. P. W., Weisberg, J. M., Chael, A. A., Lee, K. J., & Lorimer, D. R. 2012, ApJ,  
991 755, 39
- 992 Weekes, T. C., et al. 2002, Astroparticle Physics, 17, 221
- 993 Weltevrede, P., et al. 2010, ApJ, 708, 1426
- 994 Wu, J. H. K., Wu, E. M. H., Hui, C. Y., Tam, P. H. T., Huang, R. H. H., Kong, A. K. H.,  
995 & Cheng, K. S. 2011, ApJ, 740, L12
- 996 Yadigaroglu, I.-A., & Romani, R. W. 1997, ApJ, 476, 347
- 997 Zavlin, V. E. 2007, ApJ, 665, L143

Table 1. List of TeV sources analyzed

| TeV source       | Type                 | (l,b) (°)       | TeV morphology           | Reference                   |
|------------------|----------------------|-----------------|--------------------------|-----------------------------|
| HESS J1018-589   | UNID                 | (284.23,-1.72)  | pointsource              | (Abramowski et al. 2012b)   |
| HESS J1023-577   | Massive Star Cluster | (284.22,-0.40)  | gaussian(0.18)           | (Abramowski et al. 2011d)   |
| HESS J1026-582   | PWN                  | (284.80,-0.52)  | gaussian(0.14)           | (Abramowski et al. 2011d)   |
| HESS J1119-614   | PWN                  | (292.10,-0.49)  | gaussian(0.05)           | <sup>8</sup>                |
| HESS J1303-631   | PWN                  | (304.24,-0.36)  | gaussian(0.16)           | (Aharonian et al. 2005c)    |
| HESS J1356-645   | PWN                  | (309.81,-2.49)  | gaussian(0.20)           | (Abramowski et al. 2011c)   |
| HESS J1418-609   | PWN                  | (313.25,0.15)   | Ell. gaussian(0.08,0.06) | (Aharonian et al. 2006a)    |
| HESS J1420-607   | PWN                  | (313.56,0.27)   | gaussian(0.06)           | (Aharonian et al. 2006a)    |
| HESS J1427-608   | UNID                 | (314.41,-0.14)  | Ell. gaussian(0.04,0.08) | (Aharonian et al. 2008b)    |
| HESS J1458-608   | PWN                  | (317.75, -1.7)  | gaussian(0.17)           | (de los Reyes et al. 2012)  |
| HESS J1503-582   | UNID                 | (319.62,0.29)   | gaussian(0.26)           | (Renaud et al. 2008)        |
| HESS J1507-622   | UNID                 | (317.95,-3.49)  | gaussian(0.15)           | (Acero et al. 2011)         |
| HESS J1514-591   | PWN                  | (320.33,-1.19)  | Ell. gaussian(0.11,0.04) | (Aharonian et al. 2005b)    |
| HESS J1554-550   | PWN                  | (327.16,-1.07)  | pointsource              | (Acero et al. 2012)         |
| HESS J1614-518   | massive star cluster | (331.52,-0.58)  | Ell. gaussian(0.23,0.15) | (Aharonian et al. 2006d)    |
| HESS J1616-508   | PWN                  | (332.39,-0.14)  | gaussian(0.14)           | (Aharonian et al. 2006d)    |
| HESS J1626-490   | UNID                 | (334.77,0.05)   | Ell. gaussian(0.07,0.10) | (Aharonian et al. 2008b)    |
| HESS J1632-478   | PWN                  | (336.38,0.19)   | Ell. gaussian(0.21,0.06) | (Aharonian et al. 2006d)    |
| HESS J1634-472   | UNID                 | (337.11,0.22)   | gaussian(0.11)           | (Aharonian et al. 2006d)    |
| HESS J1640-465   | PWN                  | (338.32,-0.02)  | gaussian(0.04)           | (Aharonian et al. 2006d)    |
| HESS J1646-458   | Massive Star Cluster | (339.57, -0.02) | gaussian(0.35)           | (Abramowski et al. 2012a)   |
| HESS J1646-458 B | Massive Star Cluster | (339.01, -0.79) | gaussian(0.25)           | (Abramowski et al. 2012a)   |
| HESS J1702-420   | UNID                 | (344.30,-0.18)  | Ell. gaussian(0.30,0.15) | (Aharonian et al. 2006d)    |
| HESS J1708-443   | PWN                  | (343.06,-2.38)  | gaussian(0.29)           | (Abramowski et al. 2011b)   |
| HESS J1718-385   | PWN                  | (348.83,-0.49)  | Ell. gaussian(0.15,0.07) | (Aharonian et al. 2007)     |
| HESS J1729-345   | UNID                 | (353.44,-0.13)  | gaussian(0.14)           | (Abramowski et al. 2011a)   |
| HESS J1804-216   | UNID                 | (8.40,-0.03)    | Ell. gaussian(0.16,0.27) | (Aharonian et al. 2006d)    |
| HESS J1809-193   | PWN                  | (11.18,-0.09)   | Ell. gaussian(0.53,0.25) | (Aharonian et al. 2007)     |
| HESS J1813-178   | PWN                  | (12.81,-0.03)   | gaussian(0.04)           | (Aharonian et al. 2006d)    |
| HESS J1818-154   | PWN                  | (15.41,0.17)    | gaussian(0.14)           | (Hofverberg et al. 2011)    |
| HESS J1825-137   | PWN                  | (17.71,-0.70)   | Ell. gaussian(0.13,0.12) | (Aharonian et al. 2006b)    |
| HESS J1831-098   | PWN                  | (21.85,-0.11)   | gaussian(0.15)           | (Sheidaei et al. 2011)      |
| HESS J1833-105   | PWN                  | (21.51,-0.88)   | pointsource              | (Djannati-Atai et al. 2008) |
| HESS J1834-087   | UNID                 | (23.24,-0.31)   | gaussian(0.09)           | (Aharonian et al. 2006d)    |
| HESS J1837-069   | UNID                 | (25.18,-0.12)   | Ell. gaussian(0.12,0.05) | (Aharonian et al. 2006d)    |
| HESS J1841-055   | UNID                 | (26.80,-0.20)   | Ell. gaussian(0.41,0.25) | (Aharonian et al. 2008b)    |
| HESS J1843-033   | UNID                 | (29.30,0.51)    | pointsource              | (Hoppe 2008)                |
| HESS J1846-029   | PWN                  | (29.70,-0.24)   | pointsource              | (Djannati-Atai et al. 2008) |
| HESS J1848-018   | Massive Star Cluster | (31.00,-0.16)   | gaussian(0.32)           | (Chaves et al. 2008)        |
| HESS J1849-000   | PWN                  | (32.64,0.53)    | pointsource              | (Terrier et al. 2008)       |
| HESS J1857+026   | UNID                 | (35.96,-0.06)   | Ell. gaussian(0.11,0.08) | (Aharonian et al. 2008b)    |
| HESS J1858+020   | UNID                 | (35.58,-0.58)   | Ell. gaussian(0.08,0.02) | (Aharonian et al. 2008b)    |
| HESS J1912+101   | PWN                  | (44.39,-0.07)   | gaussian(0.26)           | (Aharonian et al. 2008a)    |
| MGRO J0631+105   | PWN                  | (201.30,0.51)   | pointsource              | (Abdo et al. 2009f)         |
| MGRO J0632+17    | PWN                  | (195.34,3.78)   | gaussian(1.30)           | (Abdo et al. 2009f)         |
| MGRO J1844-035   | UNID                 | (28.91,-0.02)   | pointsource              | (Abdo et al. 2009f)         |

Table 1—Continued

| TeV source      | Type                | (l,b) ( $^{\circ}$ ) | TeV morphology | Reference               |
|-----------------|---------------------|----------------------|----------------|-------------------------|
| MGRO J1900+039  | UNID                | (37.42,-0.11)        | pointsource    | (Abdo et al. 2009f)     |
| MGRO J1908+06   | UNID                | (40.39,-0.79)        | gaussian(0.34) | (Aharonian et al. 2009) |
| MGRO J1958+2848 | PWN                 | (65.85,-0.23)        | pointsource    | (Abdo et al. 2009f)     |
| MGRO J2019+37   | PWN                 | (75.00,0.39)         | gaussian(0.55) | (Abdo et al. 2007b)     |
| MGRO J2031+41 A | UNID                | (79.53,0.64)         | gaussian(1.50) | (Abdo et al. 2007b)     |
| MGRO J2031+41 B | UNID                | (80.25,1.07)         | gaussian(0.10) | (Bartoli et al. 2012)   |
| MGRO J2228+611  | PWN                 | (106.57,2.91)        | pointsource    | (Abdo et al. 2009f)     |
| VER J0006+727   | PWN                 | (119.58,10.20)       | pointsource    | (McArthur 2011)         |
| VER J1930+188   | PWN                 | (54.10,0.26)         | pointsource    | (Acciari et al. 2010)   |
| VER J1959+208   | PSR                 | (59.20,-4.70)        | pointsource    | (Hall et al. 2003)      |
| VER J2016+372   | UNID                | (74.94,1.15)         | pointsource    | (Aliu 2011)             |
| W49A            | Star Forming Region | (43.27,-0.00)        | pointsource    | (Brun et al. 2011)      |

Note. — The first two columns list the TeV source names and types as defined in the TeV catalog provided by the university of Chicago: PWN for Pulsar Wind Nebula, PSR for Pulsars, UNID for Unidentified sources, Massive Star Cluster and Star Forming Regions. The 3<sup>rd</sup> column reports the Galactic coordinates for each source. The 4<sup>th</sup> column presents the shape that best describes the source at TeV energies, together with a reference in the 5<sup>th</sup> column.

Table 2. List of sources with a pulsar within  $0.5^\circ$

| Source name      | Pulsar Name    | distance ( $^\circ$ ) | pulsar 2FGL name   | Included in the model |
|------------------|----------------|-----------------------|--------------------|-----------------------|
| HESS J1018-589   | PSR J1016-5857 | 0.22                  | 2FGL J1016.5-5858  | N <sup>a</sup>        |
| HESS J1023-577   | PSR J1023-5746 | 0.05                  | 2FGL J1022.7-5741  | N <sup>b</sup>        |
| HESS J1026-5819  | PSR J1028-5819 | 0.27                  | 2FGL J1028.5-5819  | Y                     |
| HESS J1119-614   | PSR J1119-6127 | 0.07                  | 2FGL J1118.8-6128  | N <sup>a</sup>        |
| HESS J1356-645   | PSR J1357-6429 | 0.12                  | 2FGL J1356.0-6436  | N <sup>a</sup>        |
| HESS J1418-609   | PSR J1418-6058 | 0.05                  | 2FGL J1418.7-6058  | N <sup>b</sup>        |
| HESS J1420-607   | PSR J1420-6048 | 0.05                  | 2FGL J1420.1-6047  | N <sup>b</sup>        |
| HESS J1458-608   | PSR J1459-6053 | 0.17                  | 2FGL J1459.4-6054  | N <sup>a</sup>        |
| HESS J1514-591   | PSR J1513-5908 | 0.03                  | -                  | N <sup>b</sup>        |
| HESS J1646-458 B | PSR J1648-4611 | 0.42                  | 2FGL J1646-4611    | N <sup>c</sup>        |
| HESS J1702-420   | PSR J1702-4128 | 0.53                  | -                  | N <sup>c</sup>        |
| HESS J1708-443   | PSR J1709-4429 | 0.25                  | 2FGL J1709.7-4429  | N <sup>b</sup>        |
| HESS J1718-385   | PSR J1718-3825 | 0.13                  | 2FGL J1718.3-3827  | N <sup>a</sup>        |
| HESS J1804-216   | PSR J1803-2149 | 0.27                  | 2FGL J1803.3-2148  | N <sup>b</sup>        |
| HESS J1833-105   | PSR J1833-1034 | 0.01                  | 2FGL J1833.6-1032  | N <sup>a</sup>        |
| MGRO J0631+105   | PSR J0631+1036 | 0.10                  | 2FGL J0631.5+ 1035 | N <sup>a</sup>        |
| MGRO J0632+17    | PSR J0633+1746 | 0.00                  | 2FGL J0633.9+1746  | N <sup>a</sup>        |
| MGRO J1908+06    | PSR J1907+0602 | 0.23                  | 2FGL J1907.9+0602  | N <sup>a</sup>        |
| MGRO J1958+2848  | PSR J1958+2846 | 0.12                  | 2FGL J1958.6+2845  | N <sup>a</sup>        |
| MGRO J2019+37    | PSR J2021+3651 | 0.36                  | 2FGL J2021.0+3651  | N <sup>b</sup>        |
| MGRO J2228+61    | PSR J2229+6114 | 0.09                  | 2FGL J2229+6114    | N <sup>a</sup>        |
| VER J0006+727    | PSR J0007+7303 | 0.26                  | 2FGL J0007.0+7303  | N <sup>a</sup>        |

a- The distance between the pulsar and the source is lower than  $0.27^\circ$ .

b- The pulsar is located inside the edge of the TeV shape.

c- No significant excess above 10 GeV at the position of the pulsar.

Note. — List of sources having a known  $\gamma$ -ray pulsar within  $0.5^\circ$ . The two first columns list the TeV source and the pulsar name. The third column gives the distance between the TeV source and the GeV pulsar. The pulsar position comes from Abdo et al. (in prep.c). In the fourth column Y means that we added the pulsar to the model and N that we didn't added it.

Table 3. Locations and spectral parameters of additional background sources above 10 GeV

| Source name         | Galactic coordinates ( $^{\circ}$ ) | TS   | Prefactor                       | Index         |
|---------------------|-------------------------------------|------|---------------------------------|---------------|
| 2FGL J1504.5–6121   | (311.81,0.30)                       | 30.7 | $(1.2 \pm 0.4) \times 10^{-15}$ | $1.8 \pm 0.3$ |
| 2FGL J1836.8–0623c  | (25.41,0.42)                        | 25.1 | $(9.4 \pm 1.9) \times 10^{-16}$ | $2.0 \pm 0.4$ |
| 2FGL J1823.1–1338c  | (17.51,-0.12)                       | 30.4 | $(4.9 \pm 0.5) \times 10^{-15}$ | $2.9 \pm 0.7$ |
| PSR J1838–0536      | (26.28,0.62)                        | 16.1 | $(5.0 \pm 1.8) \times 10^{-17}$ | $4.1 \pm 1.0$ |
| Background Source 1 | (333.59,-0.31)                      | 29   | $(6.5 \pm 2.5) \times 10^{-17}$ | $4.3 \pm 0.9$ |
| Background Source 2 | (336.96, -0.07)                     | 25.0 | $(1.2 \pm 0.4) \times 10^{-15}$ | $1.9 \pm 0.4$ |

Note. — The first two columns describe the source names and their corresponding Galactic coordinates. The test statistic (TS) for the source significance is provided in the 3<sup>rd</sup> column. The spectral results are presented in columns 4 and 5 for a power-law model (Equation 2) with a scale parameter  $E_0 = 56234$  MeV which corresponds to the middle of the 10–316 GeV interval in log scale. PSR J1838–0536 has been added to help the morphology fit of HESS J1841–055 which is a diffuse source. The spectral fit is consistent with the pulsar component (index of  $\sim 5$ ).

Table 4. Morphological results for LAT-detected TeV sources above 10 GeV

| TeV source      | $TS_{TeV}$ | $TS_{GeV}$ | $TS_{ext}$ | $TS_{GeV/TeV}$ | Significance | Morphology |
|-----------------|------------|------------|------------|----------------|--------------|------------|
| HESS J1018-589  | 29.1       | 29.1       | 0          | 0              | 0            | TeV        |
| HESS J1023-575  | 52.0       | 49.4       | 1.5        | -              | -            | TeV        |
| HESS J1119-614  | 27.3       | 27.3       | 12.2       | 0              | 0            | TeV        |
| HESS J1303-631  | 37.2       | 52.5       | 24.9       | 15.3           | 3.1          | Disk       |
| HESS J1356-645  | 25.8       | 28.8       | 2.5        | 3.0            | 1.2          | TeV        |
| HESS J1418-609  | 30.4       | 30.9       | 0.1        | 0.5            | 0.2          | TeV        |
| HESS J1420-607  | 41         | 41.2       | 1.8        | 0.2            | 0            | TeV        |
| HESS J1507-622  | 20.9       | 22.1       | 7.2        | 1.2            | 0.6          | TeV        |
| HESS J1514-591  | 169.5      | 147.3      | 10.4       | -              | -            | TeV        |
| HESS J1614-518  | 119.6      | 146.3      | 59.6       | 26.7           | 4.5          | Disk       |
| HESS J1616-508  | 76.2       | 79.6       | 19.9       | 3.4            | 1.0          | TeV        |
| HESS J1632-478  | 120.8      | 143        | 52.4       | 22.2           | 4.3          | Disk       |
| HESS J1634-472  | 28.7       | 29.6       | 5.2        | 0.9            | 0.5          | TeV        |
| HESS J1640-465  | 45.4       | 48.9       | 0          | 3.5            | 1.4          | TeV        |
| HESS J1708-443  | 721.8      | 1153.3     | 0          | 431.5          |              | point-like |
| HESS J1804-216  | 131        | 137.8      | 41.1       | 6.8            | 1.8          | TeV        |
| HESS J1825-137  | 55.7       | 78.1       | 27.9       | 22.4           | 4.0          | Disk       |
| HESS J1834-087  | 31         | 28.7       | 2.6        | -              | -            | TeV        |
| HESS J1837-069  | 74         | 106.7      | 45.8       | 32.7           | 5.1          | Disk       |
| HESS J1841-055  | 52         | 65         | 38.3       | 13.0           | 2.8          | TeV        |
| HESS J1848-018  | 18.7       | 18.9       | 0          | 0.2            | 0            | TeV        |
| HESS J1857+026  | 52.5       | 53.1       | 12.1       | 0.6            | 0.3          | TeV        |
| MGRO J0632+17   | 698.8      | 2056.3     | 2.5        | 1357.5         |              | point-like |
| MGRO J1908+06   | 16.4       | 37.2       | 0.2        | 20.8           | 4.2          | point-like |
| MGRO J1958+2848 | 20.8       | 23.5       | 0.2        | 2.7            | 1.1          | TeV        |
| MGRO J2019+37   | 31.1       | 98.5       | 0          | 61.3           | 8.0          | point-like |
| MGRO J2031+41 B | 72.1       | 66.4       | 6.9        | -              | -            | TeV        |
| MGRO J2228+61   | 94.5       | 114        | 0          | 19.5           | 4.0          | point-like |
| VER J0006+727   | 654.5      | 1205.6     | 1.3        | 551.1          |              | point-like |
| VER J2016+372   | 31.4       | 32.9       | 0.3        | 1.5            | 0.7          | TeV        |

Note. — Results of the morphological analysis for all LAT-detected TeV sources. The fits assumed either the TeV template defined in Table 1, a point-source model or a uniform disk model (see Equation 1). The definition of  $TS_{TeV}$ ,  $TS_{GeV}$ ,  $TS_{ext}$  and  $TS_{GeV/TeV}$  is reported in Section 4.4. The significance of the extension is measured using the  $TS_{ext}$  criterium defined in Section 4.4.



Table 5. Morphological results for LAT-detected TeV sources for which  $\text{TS}_{GeV}$  is significantly better than  $\text{TS}_{TeV}$  above 10 GeV

| TeV source     | Morphology | $\text{TS}_{ext}$ | (l,b) °         | extension(°)                           |
|----------------|------------|-------------------|-----------------|--|
| HESS J1303-631 | Disk       | 24.9              | (304.44, -0.18) | $0.50 \pm 0.05_{stat} \pm 0.07_{syst}$ |
| HESS J1614-518 | Disk       | 59.8              | (331.66, -0.66) | $0.42 \pm 0.06_{stat} \pm 0.04_{syst}$ |
| HESS J1632-478 | Disk       | 52.4              | (336.38, 0.19)  | $0.45 \pm 0.04_{stat} \pm 0.05_{syst}$ |
| HESS J1708-443 | point-like | 0                 | (343.11, -2.70) | -                                      |
| HESS J1825-137 | Disk       | 27.9              | (17.56, -0.47)  | $0.65 \pm 0.04_{stat} \pm 0.06_{syst}$ |
| HESS J1837-069 | Disk       | 45.8              | (25.08, -0.13)  | $0.32 \pm 0.05_{stat} \pm 0.07_{syst}$ |
| MGRO J0632+17  | point-like | 2.5               | (195.13, 4.27)  | -                                      |
| MGRO J1908+06  | point-like | 0.2               | (40.39, -0.79)  | -                                      |
| MGRO J2019+37  | point-like | 0                 | (75.27, 0.14)   | -                                      |
| MGRO J2228+61  | point-like | 0                 | (106.67, 2.93)  | -                                      |
| VER J0006+727  | point-like | 1.3               | (119.69, 10.47) | -                                      |

Note. — Results of the morphological analysis for LAT-detected TeV sources better described using the shape fitted at GeV energies. The fits assumed either a point-source model or a uniform disk model (see Equation 1) whose centroid and extension are provided in columns 4 and 5 respectively. The significance of the extension is measured using the  $\text{TS}_{ext}$  criterium defined in Section 4.4.

Table 6. Spectral fitting results for LAT-detected TeV sources above 10 GeV

| TeV source      | TS     | F(10–316 GeV)<br>( $10^{-10}$ ph cm $^{-2}$ s $^{-1}$ ) | E(10–316 GeV)<br>( $10^{-12}$ erg cm $^{-2}$ s $^{-1}$ ) | $\Gamma$                               |
|-----------------|--------|---|--|--|
| HESS J1018-589  | 29.1   | $1.7 \pm 0.5_{stat} \pm 0.6_{syst}$                     | $7.1 \pm 3.1_{stat} \pm 3.4_{syst}$                      | $2.41 \pm 0.49_{stat} \pm 0.49_{syst}$ |
| HESS J1023-575  | 52.0   | $4.5 \pm 0.9_{stat} \pm 2.1_{syst}$                     | $24.6 \pm 6.8_{stat} \pm 9.5_{syst}$                     | $2.04 \pm 0.26_{stat} \pm 0.32_{syst}$ |
| HESS J1119-614  | 27.3   | $2.1 \pm 0.6_{stat} \pm 0.7_{syst}$                     | $10.4 \pm 3.9_{stat} \pm 4.0_{syst}$                     | $2.15 \pm 0.37_{stat} \pm 0.38_{syst}$ |
| HESS J1303-631  | 52.5   | $5.9 \pm 1.1_{stat} \pm 4.0_{syst}$                     | $43.5 \pm 10.0_{stat} \pm 23.4_{syst}$                   | $1.71 \pm 0.19_{stat} \pm 0.39_{syst}$ |
| HESS J1356-645  | 25.3   | $1.2 \pm 0.4_{stat} \pm 0.5_{syst}$                     | $16.8 \pm 6.9_{stat} \pm 6.9_{syst}$                     | $0.99 \pm 0.39_{stat} \pm 0.40_{syst}$ |
| HESS J1418-609  | 30.4   | $4.1 \pm 1.0_{stat} \pm 1.3_{syst}$                     | $10.7 \pm 3.8_{stat} \pm 4.3_{syst}$                     | $3.54 \pm 0.81_{stat} \pm 0.57_{syst}$ |
| HESS J1420-607  | 41.0   | $3.2 \pm 0.9_{stat} \pm 1.0_{syst}$                     | $23.1 \pm 5.7_{stat} \pm 6.3_{syst}$                     | $1.91 \pm 0.27_{stat} \pm 0.31_{syst}$ |
| HESS J1507-622  | 20.9   | $1.5 \pm 0.5_{stat} \pm 0.5_{syst}$                     | $6.7 \pm 1.8_{stat} \pm 3.0_{syst}$                      | $2.33 \pm 0.43_{stat} \pm 0.48_{syst}$ |
| HESS J1514-591  | 169.5  | $6.4 \pm 0.9_{stat} \pm 1.3_{syst}$                     | $46.8 \pm 8.7_{stat} \pm 9.4_{syst}$                     | $1.72 \pm 0.15_{stat} \pm 0.17_{syst}$ |
| HESS J1614-518  | 146.3  | $12.1 \pm 1.4_{stat} \pm 3.1_{syst}$                    | $78.7 \pm 12.2_{stat} \pm 19.7_{syst}$                   | $1.85 \pm 0.14_{stat} \pm 0.18_{syst}$ |
| HESS J1616-508  | 76.2   | $9.4 \pm 1.4_{stat} \pm 2.3_{syst}$                     | $47.1 \pm 9.3_{stat} \pm 10.5_{syst}$                    | $2.16 \pm 0.19_{stat} \pm 0.20_{syst}$ |
| HESS J1632-478  | 144.0  | $15.3 \pm 1.7_{stat} \pm 5.3_{syst}$                    | $94.8 \pm 13.8_{stat} \pm 14.2_{syst}$                   | $1.91 \pm 0.14_{stat} \pm 0.19_{syst}$ |
| HESS J1634-472  | 28.7   | $5.1 \pm 1.2_{stat} \pm 2.5_{syst}$                     | $30.1 \pm 8.7_{stat} \pm 12.5_{syst}$                    | $1.97 \pm 0.26_{stat} \pm 0.29_{syst}$ |
| HESS J1640-465  | 45.4   | $4.9 \pm 1.0_{stat} \pm 1.7_{syst}$                     | $29.4 \pm 7.6_{stat} \pm 8.2_{syst}$                     | $1.95 \pm 0.23_{stat} \pm 0.20_{syst}$ |
| HESS J1708-443  | 1153.2 | $21.8 \pm 1.5_{stat} \pm 3.7_{syst}$                    | $51.5 \pm 4.2_{stat} \pm 11.0_{syst}$                    | $4.09 \pm 0.23_{stat} \pm 0.35_{syst}$ |
| HESS J1804-216  | 131.2  | $13.7 \pm 1.6_{stat} \pm 2.9_{syst}$                    | $75.2 \pm 12.5_{stat} \pm 16.3_{syst}$                   | $2.05 \pm 0.16_{stat} \pm 0.21_{syst}$ |
| HESS J1825-137  | 78.1   | $13.4 \pm 2.1_{stat} \pm 8.7_{syst}$                    | $10.9 \pm 2.0_{stat} \pm 2.1_{syst}$                     | $1.61 \pm 0.15_{stat} \pm 0.39_{syst}$ |
| HESS J1834-087  | 30.3   | $5.3 \pm 1.2_{stat} \pm 2.3_{syst}$                     | $25.2 \pm 8.1_{stat} \pm 11.9_{syst}$                    | $2.22 \pm 0.35_{stat} \pm 0.41_{syst}$ |
| HESS J1837-069  | 106.7  | $10.8 \pm 1.6_{stat} \pm 4.4_{syst}$                    | $92.6 \pm 16.8_{stat} \pm 17.6_{syst}$                   | $1.74 \pm 0.15_{stat} \pm 0.32_{syst}$ |
| HESS J1841-055  | 52.0   | $9.3 \pm 1.9_{stat} \pm 3.9_{syst}$                     | $79.6 \pm 16.0_{stat} \pm 19.1_{syst}$                   | $1.56 \pm 0.20_{stat} \pm 0.32_{syst}$ |
| HESS J1848-018  | 18.7   | $7.4 \pm 1.9_{stat} \pm 3.2_{syst}$                     | $30.0 \pm 10.1_{stat} \pm 16.5_{syst}$                   | $2.46 \pm 0.80_{stat} \pm 0.52_{syst}$ |
| HESS J1857+026  | 52.5   | $3.7 \pm 0.5_{stat} \pm 1.6_{syst}$                     | $54.0 \pm 6.9_{stat} \pm 9.1_{syst}$                     | $0.99 \pm 0.25_{stat} \pm 0.27_{syst}$ |
| MGRO J0632+17   | 2056.8 | $25.6 \pm 1.5_{stat} \pm 9.8_{syst}$                    | $54.4 \pm 3.7_{stat} \pm 14.4_{syst}$                    | $5.06 \pm 0.26_{stat} \pm 0.56_{syst}$ |
| MGRO J1908+06   | 37.2   | $2.3 \pm 0.7_{stat} \pm 1.2_{syst}$                     | $26.2 \pm 2.3_{stat} \pm 3.4_{syst}$                     | $6.17 \pm 1.17_{stat} \pm 1.50_{syst}$ |
| MGRO J1958+2848 | 20.8   | $1.3 \pm 0.4_{stat} \pm 0.6_{syst}$                     | $3.0 \pm 1.1_{stat} \pm 1.4_{syst}$                      | $4.36 \pm 1.09_{stat} \pm 1.17_{syst}$ |
| MGRO J2019+37   | 98.5   | $3.4 \pm 0.7_{stat} \pm 1.1_{syst}$                     | $7.1 \pm 1.6_{stat} \pm 1.9_{syst}$                      | $5.33 \pm 1.01_{stat} \pm 1.12_{syst}$ |
| MGRO J2031+41 B | 72.1   | $4.8 \pm 0.9_{stat} \pm 1.3_{syst}$                     | $14.1 \pm 3.2_{stat} \pm 4.2_{syst}$                     | $3.17 \pm 0.38_{stat} \pm 0.39_{syst}$ |
| MGRO J2228+61   | 114.0  | $2.9 \pm 0.5_{stat} \pm 0.5_{syst}$                     | $8.5 \pm 2.0_{stat} \pm 2.5_{syst}$                      | $3.21 \pm 0.43_{stat} \pm 0.45_{syst}$ |
| VER J0006+727   | 72.1   | $4.8 \pm 0.9_{stat} \pm 1.3_{syst}$                     | $14.1 \pm 3.2_{stat} \pm 4.2_{syst}$                     | $3.17 \pm 0.38_{stat} \pm 0.39_{syst}$ |
| VER J1959+208   | 111.5  | $2.9 \pm 0.5_{stat} \pm 0.5_{syst}$                     | $8.5 \pm 2.0_{stat} \pm 2.2_{syst}$                      | $3.22 \pm 0.43_{stat} \pm 0.45_{syst}$ |
| VER J2016+372   | 1204.6 | $12.4 \pm 0.9_{stat} \pm 1.9_{syst}$                    | $30.5 \pm 2.7_{stat} \pm 5.3_{syst}$                     | $3.85 \pm 0.22_{stat} \pm 0.31_{syst}$ |

Note. — Results of the maximum likelihood spectral fits for LAT-detected TeV sources. The test statistic (TS) for the source significance is provided in column 2. Columns 3 and 4 list the photon flux F(10–316 GeV) and the energy flux G(10–316 GeV). The fits used the best morphology reported in Table 5 and a power-law spectral model (see Equation 2) with photon index  $\Gamma$  given in column 5. The uncertainties on F(10–316 GeV), G(10–316 GeV), and  $\Gamma$  correspond respectively to the statistical and systematics uncertainties (see Section 4.7).

Table 7. Spectral fitting results for LAT-detected TeV sources in three energy bands logarithmically-spaced

| TeV source      | TS (10-31 GeV) | F(10-31 GeV)<br>( $10^{-10}$ ph cm $^{-2}$ s $^{-1}$ ) | TS (31-100 GeV) | F(31-100 GeV)<br>( $10^{-10}$ ph cm $^{-2}$ s $^{-1}$ ) | TS (100-316 GeV) | F(100-316 GeV)<br>( $10^{-10}$ ph cm $^{-2}$ s $^{-1}$ ) |
|-----------------|----------------|--|-----------------|---|------------------|--|
| HESS J1018-589  | 24.7           | $1.3 \pm 0.5_{stat} \pm 0.6_{syst}$                    | 0.5             | < 0.6   | 5.7              | < 0.6  |
| HESS J1023-575  | 42.8           | $3.7 \pm 0.8_{stat} \pm 1.8_{syst}$                    | 1.6             | < 0.9   | 18.3             | $0.6 \pm 0.3_{stat} \pm 0.3_{syst}$                      |
| HESS J1119-614  | 17.1           | $1.6 \pm 0.5_{stat} \pm 0.5_{syst}$                    | 1.0             | < 0.7   | 11.0             | $0.2 \pm 0.2_{stat} \pm 0.2_{syst}$                      |
| HESS J1303-631  | 20.9           | $3.6 \pm 0.9_{stat} \pm 3.2_{syst}$                    | 26.6            | $1.9 \pm 0.5_{stat} \pm 0.7_{syst}$                     | 7.8              | < 1.1  |
| HESS J1356-645  | 0.2            | < 9.4  | 14.7            | $0.6 \pm 0.3_{stat} \pm 0.3_{syst}$                     | 10.7             | $0.7 \pm 0.2_{stat} \pm 0.2_{syst}$                      |
| HESS J1418-609  | 28.7           | $3.7 \pm 0.9_{stat} \pm 1.2_{syst}$                    | 1.7             | < 1.1   | 0.2              | < 0.5  |
| HESS J1420-607  | 18.1           | $2.4 \pm 0.7_{stat} \pm 0.7_{syst}$                    | 12.3            | $0.8 \pm 0.3_{stat} \pm 0.3_{syst}$                     | 12.3             | $0.5 \pm 0.2_{stat} \pm 0.2_{syst}$                      |
| HESS J1507-622  | 18.2           | $1.4 \pm 0.4_{stat} \pm 0.4_{syst}$                    | 2.8             | < 0.7   | 0.5              | < 0.4  |
| HESS J1514-591  | 69.8           | $3.9 \pm 0.7_{stat} \pm 1.1_{syst}$                    | 65.7            | $1.7 \pm 0.4_{stat} \pm 0.4_{syst}$                     | 36.8             | $0.7 \pm 0.3_{stat} \pm 0.3_{syst}$                      |
| HESS J1614-518  | 73.4           | $7.9 \pm 1.2_{stat} \pm 2.5_{syst}$                    | 52.4            | $2.8 \pm 0.6_{stat} \pm 0.7_{syst}$                     | 27.2             | $0.9 \pm 0.3_{stat} \pm 0.4_{syst}$                      |
| HESS J1616-508  | 46.8           | $6.5 \pm 1.2_{stat} \pm 1.9_{syst}$                    | 28.4            | $2.3 \pm 0.6_{stat} \pm 0.6_{syst}$                     | 4.0              | < 1.0  |
| HESS J1632-478  | 71.2           | $10.3 \pm 1.5_{stat} \pm 4.1_{syst}$                   | 38.1            | $3.3 \pm 0.7_{stat} \pm 1.1_{syst}$                     | 37.6             | $1.6 \pm 0.4_{stat} \pm 0.5_{syst}$                      |
| HESS J1634-472  | 15.5           | $3.6 \pm 1.0_{stat} \pm 2.0_{syst}$                    | 11.7            | $1.3 \pm 0.5_{stat} \pm 0.6_{syst}$                     | 2.1              | < 0.8  |
| HESS J1640-465  | 20.7           | $3.2 \pm 0.9_{stat} \pm 1.5_{syst}$                    | 30.9            | $1.7 \pm 0.5_{stat} \pm 0.5_{syst}$                     | 0.0              | < 0.5  |
| HESS J1708-443  | 1131.3         | $22.0 \pm 1.5_{stat} \pm 3.3_{syst}$                   | 22.0            | $0.6 \pm 0.3_{stat} \pm 0.6_{syst}$                     | 0.0              | < 0.6  |
| HESS J1804-216  | 83.7           | $9.6 \pm 1.4_{stat} \pm 2.5_{syst}$                    | 37.1            | $2.9 \pm 0.7_{stat} \pm 0.7_{syst}$                     | 20.8             | $1.2 \pm 0.3_{stat} \pm 0.4_{syst}$                      |
| HESS J1825-137  | 18.2           | $6.4 \pm 1.6_{stat} \pm 3.4_{syst}$                    | 46.7            | $5.1 \pm 1.0_{stat} \pm 1.6_{syst}$                     | 19.4             | $1.2 \pm 0.5_{stat} \pm 0.8_{syst}$                      |
| HESS J1834-087  | 22.0           | $4.4 \pm 1.1_{stat} \pm 1.9_{syst}$                    | 7.0             | < 1.9   | 2.5              | < 1.0  |
| HESS J1837-069  | 30.6           | $6.9 \pm 1.4_{stat} \pm 3.4_{syst}$                    | 24.3            | $2.7 \pm 0.7_{stat} \pm 1.0_{syst}$                     | 28.3             | $1.7 \pm 0.4_{stat} \pm 0.5_{syst}$                      |
| HESS J1841-055  | 22.8           | $6.4 \pm 1.6_{stat} \pm 3.0_{syst}$                    | 11.0            | $2.0 \pm 0.7_{stat} \pm 1.0_{syst}$                     | 22.1             | $1.5 \pm 0.5_{stat} \pm 0.7_{syst}$                      |
| HESS J1848-018  | 16.0           | $5.8 \pm 1.6_{stat} \pm 3.1_{syst}$                    | 4.2             | < 2.6   | 0.4              | < 1.0  |
| HESS J1857+026  | 1.9            | < 2.9  | 12.9            | $1.4 \pm 0.3_{stat} \pm 0.4_{syst}$                     | 39.3             | $1.3 \pm 0.3_{stat} \pm 0.4_{syst}$                      |
| MGRO J0632+17   | 2144.4         | $27.6 \pm 1.6_{stat} \pm 9.8_{syst}$                   | 13.0            | $0.3 \pm 0.2_{stat} \pm 0.4_{syst}$                     | -0.0             | < 0.4  |
| MGRO J1908+06   | 32.1           | $2.6 \pm 0.5_{stat} \pm 1.2_{syst}$                    | 0.0             | < 0.5   | 2.6              | < 0.9  |
| MGRO J1958+2848 | 18.8           | $1.3 \pm 0.3_{stat} \pm 0.5_{syst}$                    | -0.0            | < 0.3   | -0.0             | < 0.3  |
| MGRO J2019+37   | 100.1          | $3.7 \pm 0.7_{stat} \pm 1.8_{syst}$                    | -0.0            | < 0.3   | 2.1              | < 0.5  |
| MGRO J2031+41 B | 66.7           | $4.6 \pm 0.8_{stat} \pm 1.3_{syst}$                    | 5.2             | < 0.9   | -0.0             | < 0.4  |
| MGRO J2228+61   | 108.8          | $2.7 \pm 0.5_{stat} \pm 0.5_{syst}$                    | 8.0             | < 0.7   | -0.0             | < 0.2  |
| VER J0006+727   | 1181.0         | $12.3 \pm 0.9_{stat} \pm 2.0_{syst}$                   | 38.4            | $0.4 \pm 0.2_{stat} \pm 0.2_{syst}$                     | 1.5              | < 0.3  |
| VER J2016+372   | 25.9           | $1.6 \pm 0.4_{stat} \pm 0.5_{syst}$                    | 3.4             | < 0.6   | 3.2              | < 0.5  |

Note. — Results of the maximum likelihood spectral fits for LAT-detected TeV sources in three different energy bands: 10–31 GeV, 31–100 GeV, 100–316 GeV using the same convention as in Table 6. A 99% c.l. upper limit is computed when the TS in the band is lower than 10.

Table 8. Upper limits for non-detected TeV sources above 10 GeV

| TeV source       | TS   | F(10–316 GeV)<br>( $10^{-10}$ ph cm $^{-2}$ s $^{-1}$ ) | G(10–316 GeV)<br>( $10^{-12}$ erg cm $^{-2}$ s $^{-1}$ ) |
|------------------|------|---|--|
| HESS J1026-582   | 1.0  | < 1.6   | < 9.3  |
| HESS J1427-608   | 4.4  | < 2.0   | < 11.4   |
| HESS J1458-608   | 12.6 | < 2.5   | < 14.5   |
| HESS J1503-582   | 9.8  | < 3.9   | < 22.3   |
| HESS J1554-550   | 0    | < 0.5   | < 2.8  |
| HESS J1626-490   | 1.5  | < 2.7   | < 15.4   |
| HESS J1646-458   | 1.12 | < 3.2   | < 18.1   |
| HESS J1646-458 B | 8.3  | < 4.2   | < 24.0   |
| HESS J1702-420   | 8.5  | < 6.8   | < 38.9   |
| HESS J1718-385   | 2.9  | < 2.5   | < 14.6   |
| HESS J1729-345   | 0    | < 1.3   | < 7.6  |
| HESS J1809-193   | 10.4 | < 11.0  | < 63.4   |
| HESS J1813-178   | 2.5  | < 2.4   | < 14.2   |
| HESS J1818-154   | 0    | < 1.4   | < 8.1  |
| HESS J1831-098   | 0    | < 1.8   | < 10.6   |
| HESS J1833-105   | 4.1  | < 2.1   | < 11.7   |
| HESS J1843-033   | 0    | < 1.0   | < 5.4  |
| HESS J1846-029   | 2    | < 2.0   | < 11.2   |
| HESS J1849-000   | 0.1  | < 1.3   | < 7.3  |
| HESS J1858+020   | 0    | < 1.2   | < 6.6  |
| HESS J1912+101   | 9.5  | < 4.5   | < 25.2   |
| MGRO J0631+105   | 5.9  | < 1.4   | < 7.7  |
| MGRO J1844-035   | 0    | < 1.4   | < 8.0  |
| MGRO J1900+039   | 0    | < 1.2   | < 6.9  |
| MGRO J2031+41 A  | 14.7 | < 30.0  | < 168.9  |
| VER J1930+188    | 0    | < 1.0   | < 5.5  |
| VER J1959+208    | 0    | < 0.3   | < 1.9  |
| W49 A            | 3.2  | < 2.4   | < 37.6   |

Note. — Results of the maximum likelihood spectral fits for non-detected TeV sources. The test statistic (TS) for the source significance is provided in column 2. Columns 3 and 4 list the 99% c.l. upper limits on the photon flux F(10–316 GeV) and on the energy flux G(10–316 GeV). The fits used the TeV template defined in Table 1 and a power-law spectral model (see Equation 2) with photon index fixed at 2.

Table 9. Upper limits for non-detected sources in 3 logarithmically-spaced energy bands

| TeV source       | TS (10–31 GeV) | F(10–31 GeV)<br>( $10^{-10}$ ph cm $^{-2}$ s $^{-1}$ ) | TS (31–100 GeV) | F(31–100 GeV)<br>( $10^{-10}$ ph cm $^{-2}$ s $^{-1}$ ) | TS (100–316 GeV) | F(100–316 GeV)<br>( $10^{-10}$ ph cm $^{-2}$ s $^{-1}$ ) |
|------------------|----------------|--|-----------------|---|------------------|--|
| HESS J1026-582   | 0.5            | < 1.6  | 0.0             | < 0.4   | 0.6              | < 0.7  |
| HESS J1427-608   | 0.3            | < 1.3  | 2.6             | < 0.9   | 3.3              | < 0.6  |
| HESS J1458-608   | 12.3           | $1.7 \pm 0.5_{stat} \pm 0.7_{syst}$                    | 0.4             | < 0.5   | 0.0              | < 0.3  |
| HESS J1503-582   | 0.9            | < 2.2  | 4.3             | < 1.5   | 5.2              | < 1.0  |
| HESS J1554-550   | 0.0            | < 0.6  | 0.0             | < 0.3   | 0.0              | < 0.3  |
| HESS J1626-490   | 0.7            | < 2.2  | 0.9             | < 1.1   | 0.0              | < 0.7  |
| HESS J1646-465   | 0.0            | < 2.0  | 1.5             | < 2.0   | 0.8              | < 1.1  |
| HESS J1646-465 B | 0.0            | < 2.3  | 3.4             | < 1.8   | 4.8              | < 1.2  |
| HESS J1702-420   | 0.3            | < 3.3  | 7.9             | < 3.6   | 1.0              | < 1.1  |
| HESS J1718-385   | 0.2            | < 1.7  | 0.3             | < 0.9   | 3.0              | < 1.0  |
| HESS J1729-345   | 0.0            | < 1.4  | 0.0             | < 0.8   | 0.0              | < 0.5  |
| HESS J1809-193   | 8.4            | < 9.3  | 3.3             | < 3.2   | 0.0              | < 1.2  |
| HESS J1813-178   | 0.0            | < 1.4  | 3.0             | < 1.6   | 0.5              | < 0.7  |
| HESS J1818-154   | 0.0            | < 1.5  | 0.0             | < 0.8   | 0.0              | < 0.4  |
| HESS J1831-098   | 0.0            | < 1.5  | 0.1             | < 1.0   | 0.2              | < 0.6  |
| HESS J1833-105   | 3.1            | < 1.9  | 1.2             | < 0.7   | 0.0              | < 0.7  |
| HESS J1843-033   | 0.0            | < 1.0  | 0.0             | < 0.5   | 0.0              | < 0.5  |
| HESS J1846-029   | 2.1            | < 2.3  | 0.0             | < 0.5   | 0.0              | < 0.4  |
| HESS J1849-000   | 0.2            | < 1.4  | 0.0             | < 0.5   | 0.0              | < 0.5  |
| HESS J1858+020   | 0.0            | < 1.2  | 0.0             | < 0.6   | 0.0              | < 0.4  |
| HESS J1912+101   | 0.9            | < 2.4  | 6.9             | < 2.0   | 3.2              | < 1.1  |
| MGRO J0631+105   | 3.5            | < 1.2  | 3.2             | < 0.6   | 0.0              | < 0.4  |
| MGRO J1844-035   | 0.0            | < 1.1  | 0.4             | < 0.3   | 0.0              | < 0.4  |
| MGRO J1900+039   | 0.0            | < 1.4  | 0.0             | < 0.6   | 0.0              | < 0.4  |
| MGRO J2031+41 A  | 8.7            | < 22.6   | 6.1             | < 8.4   | 0.9              | < 2.3  |
| VER J1930+188    | 0.7            | < 1.1  | 0.0             | < 0.4   | 0.0              | < 0.3  |
| VER J1959+208    | 0.0            | < 0.3  | 0.0             | < 0.3   | 0.0              | < 0.4  |
| W49 A            | 3.0            | < 5.5  | 0.5             | < 1.6   | 0.0              | < 0.8  |

Note. — Results of the maximum likelihood spectral fits for non-detected TeV sources in three different energy bands: 10–31 GeV, 31–100 GeV, 100–316 GeV using the same convention as in Table 8. A 99% c.l. upper limit is computed when the TS in the band is lower than 10.

Table 10. Spectral results for sources with a  $\gamma$ -ray detected pulsar within  $0.5^\circ$  with the pulsar included in the model

| Source name      | TS      | F(10-316 GeV)<br>( $10^{-10}$ ph cm $^{-2}$ s $^{-1}$ ) | Index                                  | shape      |
|------------------|---------|---|--|------------|
| HESS J1018-589   | 25.0    | $1.5 \pm 0.5_{stat} \pm 0.7_{syst}$                     | $2.31 \pm 0.50_{stat} \pm 0.81_{syst}$ | TeV        |
| HESS J1023-577   | 51.2    | $4.5 \pm 0.9_{stat} \pm 2.3_{syst}$                     | $2.04 \pm 0.26_{stat} \pm 0.33_{syst}$ | TeV        |
| HESS J1119-614   | 16.0    | $1.5 \pm 0.6_{stat} \pm 0.8_{syst}$                     | $1.80 \pm 0.48_{stat} \pm 0.53_{syst}$ | TeV        |
| HESS J1356-645   | 25.4    | $1.2 \pm 0.5_{stat} \pm 0.7_{syst}$                     | $1.00 \pm 0.38_{stat} \pm 0.42_{stat}$ | TeV        |
| HESS J1418-609   | 12.6    | $< 4.4$   | -                                      | TeV        |
| HESS J1420-607   | 35.8    | $3.4 \pm 0.9_{stat} \pm 1.2_{syst}$                     | $1.80 \pm 0.29_{stat} \pm 0.38_{syst}$ | TeV        |
| HESS J1458-608   | 11.0    | $< 2.5e-10$   | -                                      | TeV        |
| HESS J1708-443   | 62.7    | $8.3 \pm 1.5_{stat} \pm 4.2_{syst}$                     | $3.16 \pm 0.34_{stat} \pm 0.52_{syst}$ | point-like |
| HESS J1718-385   | 2.9     | $< 2.5$   | -                                      | TeV        |
| HESS J1646-458 B | $< 4.2$ | -   | -                                      | TeV        |
| HESS J1804-216   | 121.0   | $13.1 \pm 1.6_{stat} \pm 3.5_{syst}$                    | $2.00 \pm 0.16_{stat} \pm 0.29_{syst}$ | TeV        |
| HESS J1833-105   | 4.1     | $< 2.1$   | -                                      | TeV        |
| MGRO J0631+105   | 2.5     | $< 1.0$   | -                                      | TeV        |
| MGRO J0632+17    | 128.4   | $12.5 \pm 1.5_{stat} \pm 10.1_{syst}$                   | $4.09 \pm 0.33_{stat} \pm 0.63_{syst}$ | point-like |
| MGRO J1908+06    | 9.0     | $< 5.5$   | -                                      | TeV        |
| MGRO J1958+2848  | 18.6    | $1.2 \pm 0.4_{stat} \pm 0.7_{syst}$                     | $3.91 \pm 1.02_{stat} \pm 1.29_{syst}$ | point-like |
| MGRO J2019+37    | 16.8    | $2.1 \pm 0.8_{stat} \pm 1.2_{syst}$                     | $4.61 \pm 0.76_{stat} \pm 1.15_{syst}$ | point-like |
| MGRO J2228+61    | 18.4    | $1.5 \pm 0.5_{stat} \pm 0.5_{syst}$                     | $2.58 \pm 0.49_{stat} \pm 0.56_{syst}$ | point-like |
| VER J0006+727    | 27.9    | $3.1 \pm 0.9_{stat} \pm 1.5_{syst}$                     | $2.79 \pm 0.36_{stat} \pm 0.42_{syst}$ | point-like |

Note. — Results of the maximum likelihood spectral fits for sources with a known  $\gamma$ -ray pulsar within  $0.5^\circ$ . The pulsar is included in the model with the spectral parameters derived in the 2FGL catalog Nolan et al. (2012). A 99% c.l. upper limit is computed when the TS is lower than 16. As PSR J1028-5819 is already included and fitted in our model of the region of HESS J1026-5819 we did not report it in this table. PSR J1513-5908 and PSR J1702-4128 were detected after the 2FGL catalog analysis (Nolan et al. 2012). Therefore no spectral parameters were available for these 2 pulsars.

Table 11. Pulsars characteristics.

| Source          | PSR            | $\dot{E}$<br>erg s <sup>-1</sup> | $\tau_C$<br>kyr | Distance<br>kpc  | Ref             |
|-----------------|----------------|----------------------------------|-----------------|--|-----------------|
| Crab            | PSR J0534+2200 | 4.60e+38                         | 1.20            | 2.00 <sup>+0.50</sup> <sub>-0.50</sub>   | (1)             |
| HESS J1023-575  | PSR J1023-5746 | 1.10e+37                         | 4.60            | 2.40   | (30)            |
| HESS J1026-582  | PSR J1028-5819 | 8.40e+35                         | 90.00           | 2.30 <sup>+0.30</sup> <sub>-0.30</sub>   | (2)             |
| HESS J1119-614  | PSR J1119-6127 | 2.30e+36                         | 1.60            | 8.40 <sup>+0.40</sup> <sub>-0.40</sub>   | (3)             |
| HESS J1303-631  | PSR J1301-6305 | 1.70e+36                         | 11.00           | 6.65 <sup>+1.10</sup> <sub>-1.20</sub> - 15.84 <sup>+0.00</sup> <sub>-0.00</sub> | (4),(5)         |
| HESS J1356-645  | PSR J1357-6429 | 3.10e+36                         | 7.30            | 2.50 <sup>+0.44</sup> <sub>-0.53</sub>   | (6)             |
| HESS J1418-609  | PSR J1418-6058 | 4.90e+36                         | 1.03            | 1.60 <sup>+0.70</sup> <sub>-0.70</sub>   | (7)             |
| HESS J1420-607  | PSR J1420-6048 | 1.00e+37                         | 13.00           | 5.60 <sup>+0.85</sup> <sub>-0.91</sub>   | (5),(8)         |
| HESS J1458-608  | PSR J1459-6053 | 9.10e+35                         | 64.70           | 4.00   | (9)             |
| HESS J1514-591  | PSR J1513-5906 | 1.70e+37                         | 1.56            | 5.79 <sup>+0.90</sup> <sub>-0.80</sub> - 4.20 <sup>+0.60</sup> <sub>-0.60</sub>  | (5)             |
| HESS J1554-550  | -              | -                                | 18.00           | 7.75 <sup>+1.25</sup> <sub>-1.25</sub>   | (10),(11), (31) |
| HESS J1616-508  | PSR J1617-5055 | 1.60e+37                         | 8.13            | 6.46 <sup>+0.70</sup> <sub>-0.70</sub>   | (5),            |
| HESS J1632-478  | -              | 3.0e+36                          | 20.0            | 3.0  | (32)            |
| HESS J1640-465  | -              | 4.00e+36                         | -               | -  | (12)            |
| HESS J1702-420  | PSR J1702-4128 | 3.40e+35                         | 55.00           | 4.80 <sup>+0.50</sup> <sub>-0.60</sub>   | (13)            |
| HESS J1708-443  | PSR J1709-4429 | 3.40e+36                         | 17.50           | 2.30 <sup>+0.30</sup> <sub>-0.30</sub>   | (14)            |
| HESS J1718-385  | PSR J1718-3825 | 1.30e+36                         | 89.50           | 3.60 <sup>+0.40</sup> <sub>-0.40</sub> - 4.24 <sup>+0.40</sup> <sub>-0.40</sub>  | (15), (5)       |
| HESS J1804-216  | PSR J1803-2137 | 2.20e+36                         | 16.00           | 3.80 <sup>+0.40</sup> <sub>-0.50</sub>   | (5),(6)         |
| HESS J1809-193  | PSR J1809-1917 | 1.80e+36                         | 51.30           | 3.71 <sup>+0.50</sup> <sub>-0.40</sub>   | (5),(6)         |
| HESS J1813-178  | PSR J1813-1749 | 6.80e+37                         | 5.40            | -  | (5)             |
| HESS J1818-154  | -              | -                                | 9.00            | 10.0   | (16)            |
| HESS J1825-137  | PSR J1826-1334 | 2.80e+36                         | 21.00           | 4.12 <sup>+0.40</sup> <sub>-0.40</sub>   | (5),(6)         |
| HESS J1831-098  | PSR J1831-0952 | 1.10e+36                         | 128.00          | 4.33   | (5)             |
| HESS J1833-105  | PSR J1833-1034 | 3.40e+37                         | 4.85            | 4.70 <sup>+0.50</sup> <sub>-0.40</sub>   | (17)            |
| HESS J1841-055  | PSR J1838-0537 | 5.90e+36                         | 4.97            | 1.30   | (18)            |
| HESS J1846-029  | PSR J1846-0258 | 8.10e+36                         | 0.73            | 5.10   | (5)             |
| HESS J1848-018  | -              | -                                | -               | 4.70   | (19)            |
| HESS J1849-000  | PSR J1849-001  | 9.80e+36                         | 42.90           | 7.00   | (20)            |
| HESS J1857+026  | PSR J1856+0245 | 4.60e+36                         | 20.60           | 10.28  | (5)             |
| HESS J1912+101  | PSR J1913+1011 | 2.90e+36                         | 169.00          | 4.48   | (5)             |
| MGRO J0631+105  | PSR J0631+1036 | 1.70e+35                         | 43.60           | 3.70 <sup>+1.25</sup> <sub>-0.89</sub>   | (21)            |
| MGRO J0632+17   | PSR J0633+1746 | 3.20e+34                         | 342.00          | 0.20 <sup>+0.02</sup> <sub>-0.01</sub>   | (22)            |
| MGRO J1958+2848 | PSR J1958+2846 | 3.40e+35                         | 21.70           | -  | (5)             |
| MGRO J2019+37   | PSR J2021+3651 | 3.40e+36                         | 17.20           | 1.40 - 8.00  | (23), (24)      |
| MGRO J2228+61   | PSR J2229+6114 | 2.20e+37                         | 10.50           | 1.50 - 7.30 <sup>+3.30</sup> <sub>-2.00</sub>                                    | (25), (26)      |
| VER J0006+727   | PSR J0007+7303 | 4.50e+35                         | 13.90           | 1.40 <sup>+0.30</sup> <sub>-0.30</sub>   | (27)            |
| VER J1930+188   | PSR J1930+1852 | 1.20e+37                         | 2.89            | -  | (28)            |
| Vela X          | PSR J0835-4510 | 6.90e+36                         | 11.30           | 0.30 <sup>+0.02</sup> <sub>-0.02</sub>   | (29)            |

Note. — This table summarizes the pulsars properties taken into account in this analysis to perform the populations studies in Figures 24 & 23. Column 3 shows the pulsar spin-down power as found in the litterature, column 4 and 5 present the characteristic age of the pulsar and its distance.

References: (1) Trimble (1973), (2) Keith et al. (2008), (3) Caswell et al. (2004), (4) Abramowski (in prep.), (5) Manchester et al. (2005), (6) Lorimer et al. (2006), (7) Yadigaroglu & Romani (1997), (8) Kishishita et al. (2012), (9) Mattana et al. (2009), (10) Seward et al. (1996), (11) Sun et al. (1999), (12) Funk et al. (2007a), (13) Kramer et al. (2003), (14) Johnston et al. (1995), (15) Manchester et al. (2001), (16) Hofverberg (2011),

(17) Camilo et al. (2006), (18) Pletsch et al. (2012), (19) Chaves et al. (2008), (20) Gotthelf et al. (2011), (21) Weltevrede et al. (2010), (22) Verbiest et al. (2012), (23) Yadigaroglu & Romani (1997), (24) Hessels et al. (2004), (25) Abdo et al. (2009c), (26) Kothes et al. (2001), (27) Pineault et al. (1993), (28) Leahy et al. (2008), (29) Dodson et al. (2003), (30) Saz Parkinson et al. (2010), (31) Temim et al. (2009), (32) ?.



Table 12. PWNe properties.

| Source          | $G_{10}^{300\text{GeV}}$<br>$10^{-12} \text{ erg cm}^{-2} \text{ s}^{-1}$ | $G_1^{30\text{TeV}}$<br>$10^{-12} \text{ erg cm}^{-2} \text{ s}^{-1}$ | $G_2^{10\text{keV}}$<br>$10^{-12} \text{ erg cm}^{-2} \text{ s}^{-1}$ | $L_{\text{PWN}}$<br>$10^{34} \text{ erg s}^{-1}$     | Ref       |
|-----------------|---|---|---|--|-----------|
| Crab            | $485.7 \pm 187.56$  | $80.0 \pm 16.5$   | $2.10\text{e}+04 \pm 4.20\text{e}+3$                                  | $23.24^{+14.68}_{-14.68}$                            | (1)       |
| HESS J1023-591  | $24.6 \pm 11.68$  | $4.8 \pm 1.7$   | -   | $1.70^{+0.81}_{-0.81}$                               | (2)       |
| HESS J1026-582  | $< 9.3$   | $3.7 \pm 2.2$   | -   | $< 0.59$   | (2)       |
| HESS J1119-614  | $10.4 \pm 5.66$   | $1.2 \pm 0.5$   | -   | $8.78^{+4.85}_{-4.85}$                               | (3)       |
| HESS J1303-631  | $43.5 \pm 25.45$  | $25.0 \pm 1.0$  | $1.60\text{e}-01 \pm 3.00\text{e}-02$                                 | $23.02^{+15.47}_{-15.82} - 130.59^{+76.39}_{-76.39}$ | (12)      |
| HESS J1356-645  | $16.8 \pm 9.76$   | $6.7 \pm 3.7$   | $6.04\text{e}-02 \pm 1.28\text{e}-02$                                 | $1.26^{+0.85}_{-0.90}$                               | (4)       |
| HESS J1418-609  | $< 24.9$  | $2.4 \pm 0.6$   | $6.27\text{e}+00 \pm 1.30\text{e}-01$                                 | $< 1.19 - < 7.45$                                    | (3), (13) |
| HESS J1420-607  | $23.1 \pm 8.50$   | $14.5 \pm 3.3$  | $1.30\text{e}+00 \pm 0.26\text{e}+00$                                 | $8.67^{+4.13}_{-4.25}$                               | (1)       |
| HESS J1458-608  | $< 14.5$  | $2.5 \pm 0.7$   | -   | $< 2.78$   | (5)       |
| HESS J1514-591  | $46.8 \pm 12.81$  | $20.3 \pm 4.2$  | $2.86\text{e}+01 \pm 5.72\text{e}+00$                                 | $18.77^{+7.78}_{-7.30} - 9.88^{+3.91}_{-3.91}$       | (1)       |
| HESS J1554-550  | $< 2.8$   | $0.7 \pm 0.4$   | $3.07\text{e}+00 \pm 1.00\text{e}+00$                                 | $< 2.01$   | (3), (14) |
| HESS J1616-508  | $47.1 \pm 14.03$  | $21.0 \pm 5.0$  | $4.20\text{e}+00 \pm 8.4\text{e}-01$                                  | $23.52^{+8.66}_{-8.66}$                              | (1)       |
| HESS J1632-478  | $94.8 \pm 19.80$  | $14.8 \pm 4.7$  | $4.30\text{e}-01 \pm 8.00\text{e}-02$                                 | -  | (6)       |
| HESS J1640-465  | $29.4 \pm 11.18$  | $5.5 \pm 1.2$   | $4.60\text{e}-01 \pm 9.20\text{e}-02$                                 | -  | (7)       |
| HESS J1702-420  | $< 38.9$  | $9.1 \pm 3.4$   | $6.00\text{e}-03 \pm 1.20\text{e}-03$                                 | $< 10.72$  | -         |
| HESS J1708-443  | $24.4 \pm 11.90$  | $3.6 \pm 2.5$   | -   | $1.55^{+0.85}_{-0.85}$                               | (3)       |
| HESS J1718-385  | $< 14.6$  | $4.3 \pm 1.6$   | $1.40\text{e}-01 \pm 2.80\text{e}-02$                                 | $< 2.26 - 3.14$                                      | (1)       |
| HESS J1804-216  | $75.2 \pm 20.54$  | $11.8 \pm 2.4$  | $6.80\text{e}-02 \pm 1.36\text{e}-02$                                 | $12.99^{+4.48}_{-4.93}$                              | -         |
| HESS J1809-193  | $< 63.4$  | $19.0 \pm 5.7$  | $2.30\text{e}-01 \pm 4.60\text{e}-02$                                 | $< 10.44$  | (1)       |
| HESS J1813-178  | $< 14.2$  | $5.0 \pm 0.6$   | -   | -  | (3)       |
| HESS J1818-154  | $< 8.1$   | $1.3 \pm 0.9$   | -   | -  | (8)       |
| HESS J1825-137  | $180.7 \pm 27.73$   | $61.0 \pm 13.9$   | $4.40\text{e}-01 \pm 8.80\text{e}-02$                                 | $36.70^{+9.08}_{-9.08}$                              | (1)       |
| HESS J1831-098  | $< 10.6$  | $5.1 \pm 0.8$   | -   | $< 2.38$   | (3)       |
| HESS J1833-105  | $< 11.7$  | $2.4 \pm 1.2$   | $4.00\text{e}+01 \pm 8.00\text{e}+00$                                 | $< 3.09$   | (1)       |
| HESS J1841-055  | $79.6 \pm 24.92$  | $23.5 \pm 3.4$  | -   | $1.61^{+0.50}_{-0.50}$                               | (9)       |
| HESS J1846-029  | $< 11.2$  | $2.3 \pm 0.8$   | $2.27\text{e}+01 \pm 4.54\text{e}+00$                                 | $< 3.49$   | (1)       |
| HESS J1848-018  | $30.0 \pm 19.35$  | $4.3 \pm 1.0$   | -   | $7.93^{+5.11}_{-5.11}$                               | (10)      |
| HESS J1849-000  | $< 7.3$   | $2.1 \pm 0.4$   | $9.00\text{e}-01 \pm 2.00\text{e}-01$                                 | $< 4.28$   | (11)      |
| HESS J1857+026  | $54.0 \pm 26.89$  | $6.1 \pm 1.0$   | -   | $68.28^{+34.00}_{-34.00}$                            | (3)       |
| HESS J1912+101  | $< 25.2$  | $2.4 \pm 0.7$   | -   | $< 6.05$   | (3)       |
| MGRO J0631+105  | $< 7.7$   | -   | -   | $< 0.09$   | -         |
| MGRO J0632+17   | $29.5 \pm 14.87$  | -   | -   | $0.01^{+0.01}_{-0.01}$                               | -         |
| MGRO J1958+2848 | $3.0 \pm 1.78$  | -   | -   | -  | -         |
| MGRO J2019+37   | $7.1 \pm 2.33$  | -   | -   | $0.17^{+0.05}_{-0.05} - 5.44^{+1.79}_{-1.79}$        | -         |
| MGRO J2228+61   | $5.8 \pm 2.80$  | -   | -   | $0.16^{+0.08}_{-0.08} - 0.95^{+0.55}_{-0.55}$        | -         |
| VER J0006+727   | $14.1 \pm 5.28$   | -   | -   | $0.33^{+0.19}_{-0.19}$                               | -         |
| VER J1930+188   | $< 5.5$   | $1.2 \pm 0.4$   | -   | -  | (3)       |
| VelaX           | $134.2 \pm 11.14$   | $79.0 \pm 21.9$   | $5.39\text{e}+01$   | $0.14^{+0.02}_{-0.02}$                               | (1)       |

Note. — This table summarizes the PWNe properties and the fluxes taken into account in this analysis to perform the populations studies in Figures 24 & 23. Column 2,3 and 4 summarize the fluxes found in the GeV (10-316 GeV), TeV (1-30 TeV) and X-ray (2-10 keV) energy ranges. Column 5 shows the luminosity found using the energy flux in column 2 and the distance in Table 11. References : (1) Mattana et al. (2009) and references therein, (2) Abramowski et al. (2011d), (3) Mayer (2010), (4) Abramowski et al. (2011c), (5) de los Reyes et al. (2012), (6) ?, (7) Aharonian et al. (2006d), (8) Hofverberg et al. (2011), (9) Aharonian et al. (2008b), (10) Chaves et al. (2008), (11) Terrier et al. (2008), (12) Abramowski (in prep.), (13) Kishishita et al. (2012), (14) Temim et al. (2009).

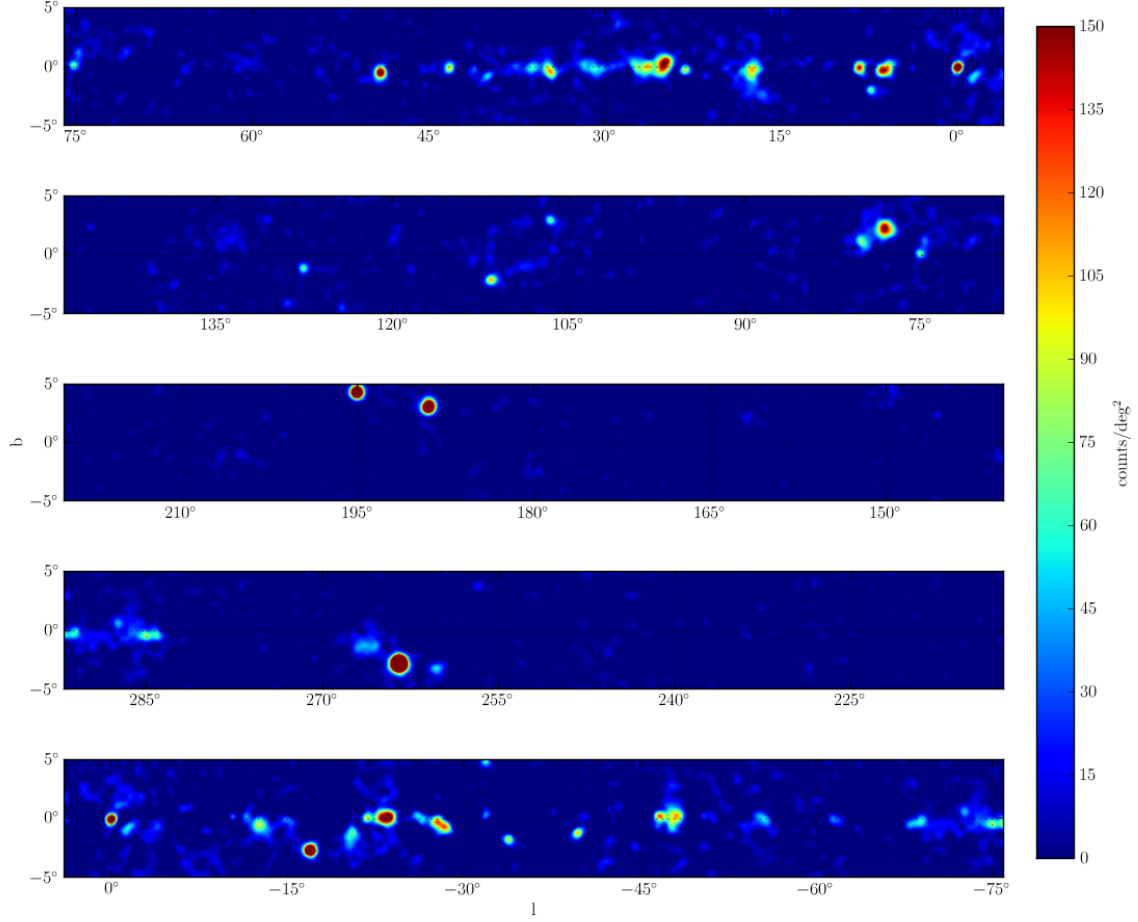


Fig. 1.— Residual counts map of the Galactic Plane above 10 GeV. The Galactic and isotropic diffuse emission are subtracted using the files described in section 4.2 with a normalization of 1. All sources associated to Blazars are subtracted using the spectral parameters listed in the hard source list (Abdo et al. in prep.a). Excesses visible in this map are due either to Galactic sources or to Blazars not yet associated, emitting above 10 GeV observed by the LAT. The counts map is smoothed with a Gaussian of  $0.27^\circ$ .

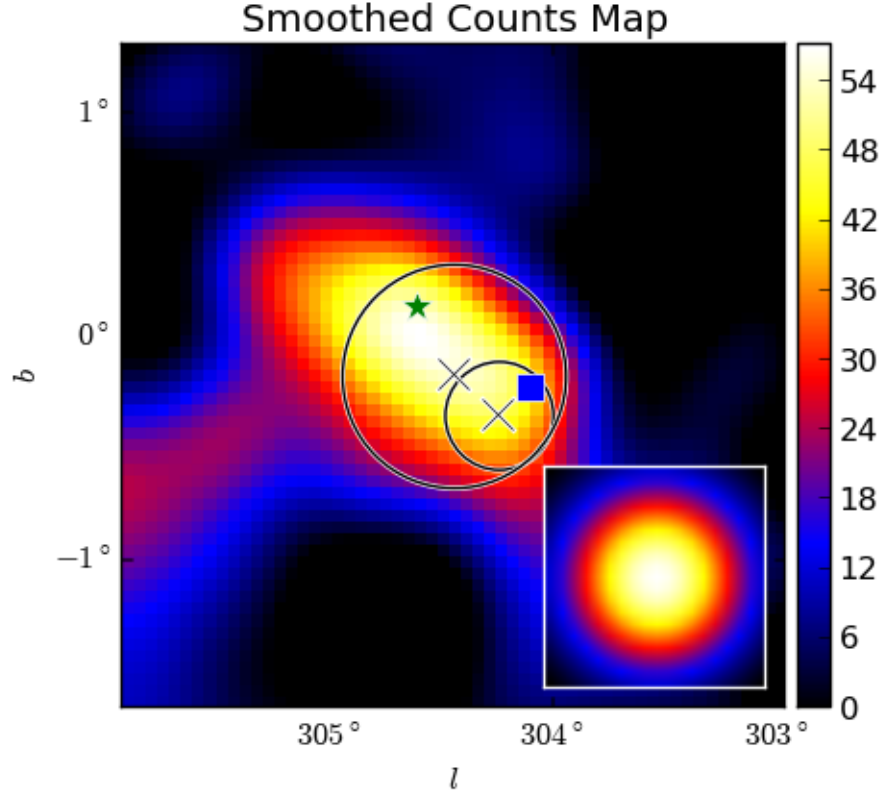


Fig. 2.— Counts map of the region of HESS J1303–631. We subtracted the Galactic and isotropic diffuse emission. The counts map is smoothed by a Gaussian of  $0.27^\circ$  corresponding to the PSF above 10 GeV. The green star indicates the position of the SNR Kes 17, the blue square represents the position of PSR J1301–6305. The small and big circles respectively show the extension of the TeV Gaussian proposed by Aharonian et al. (2005c) and the extension of the disk derived in this work.

Table 13. Results of the fit of the IC peak.

| Source         | $\Gamma_{TeV}$  | $\alpha$        | Epeak<br>MeV                          |
|----------------|-----------------|-----------------|---------------------------------------|
| HESS J1023–577 | $2.58 \pm 0.27$ | $2.24 \pm 0.41$ | $1.23\text{e}+05 \pm 7.90\text{e}+04$ |
| HESS J1119–614 | $2.75 \pm 0.15$ | $2.49 \pm 0.36$ | $3.73\text{e}+04 \pm 2.56\text{e}+04$ |
| HESS J1303–631 | $2.44 \pm 0.03$ | $1.77 \pm 0.35$ | $1.14\text{e}+06 \pm 6.32\text{e}+05$ |
| HESS J1356–645 | $2.20 \pm 0.28$ | $1.92 \pm 0.38$ | $4.79\text{e}+05 \pm 3.06\text{e}+05$ |
| HESS J1420–607 | $2.17 \pm 0.1$  | $1.92 \pm 0.28$ | $7.16\text{e}+05 \pm 4.15\text{e}+05$ |
| HESS J1514–591 | $2.27 \pm 0.31$ | $2.05 \pm 0.41$ | $2.46\text{e}+05 \pm 9.81\text{e}+04$ |
| HESS J1632–478 | $2.12 \pm 0.2$  | $2.13 \pm 0.43$ | $3.27\text{e}+04 \pm 1.87\text{e}+04$ |
| HESS J1804–216 | $2.72 \pm 0.06$ | $2.32 \pm 0.34$ | $4.01\text{e}+04 \pm 1.83\text{e}+04$ |
| HESS J1825–137 | $2.40 \pm 0.30$ | $2.47 \pm 0.49$ | $2.07\text{e}+05 \pm 9.51\text{e}+04$ |
| HESS J1841–055 | $2.41 \pm 0.08$ | $1.74 \pm 0.35$ | $3.36\text{e}+05 \pm 1.73\text{e}+04$ |
| HESS J1857+026 | $2.39 \pm 0.05$ | $2.03 \pm 0.35$ | $3.92\text{e}+05 \pm 1.94\text{e}+05$ |

Note. —

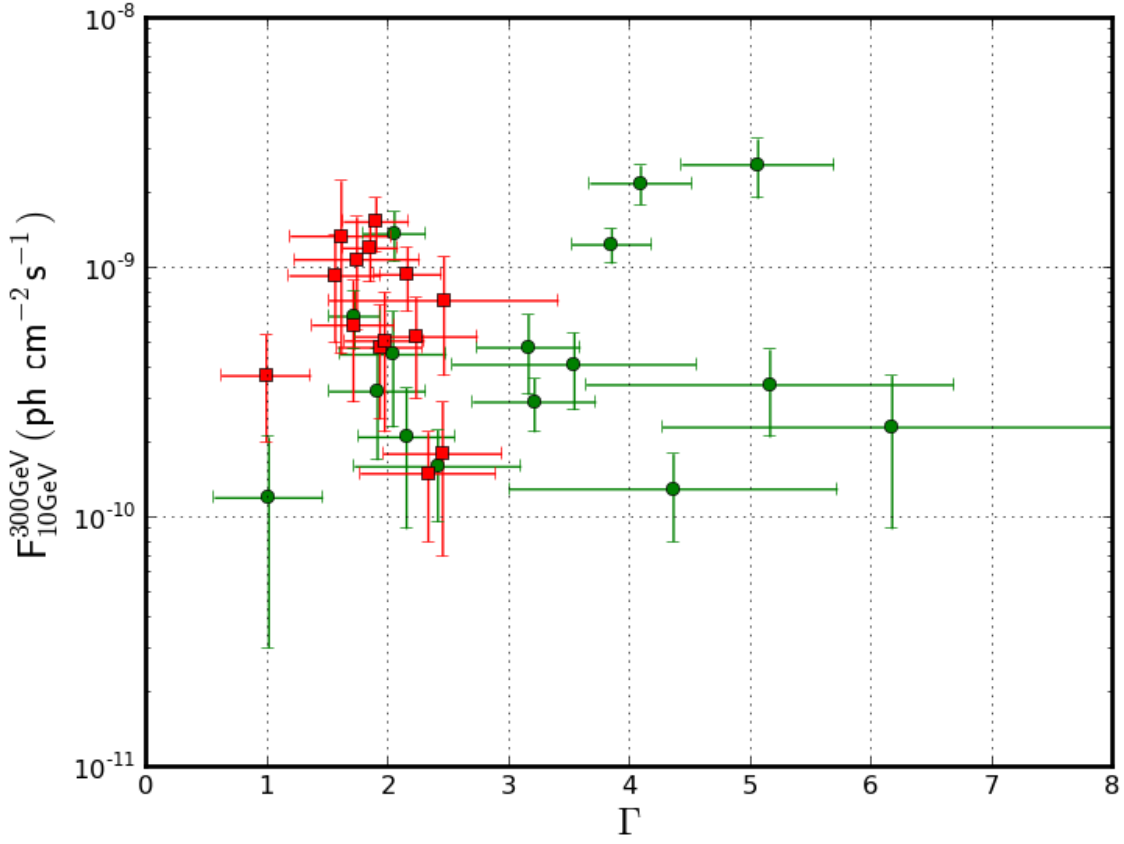


Fig. 3.— Integrated flux of the detected sources as a function of the power-law index between 10 and 316 GeV (see Table 6). The green circles show the sources within  $0.5^\circ$  of a pulsar detected by the LAT while the red squares represent the sources with no pulsar detected in the GeV energy range within  $0.5^\circ$ . The error bars show the statistical and systematic uncertainties added in quadrature.

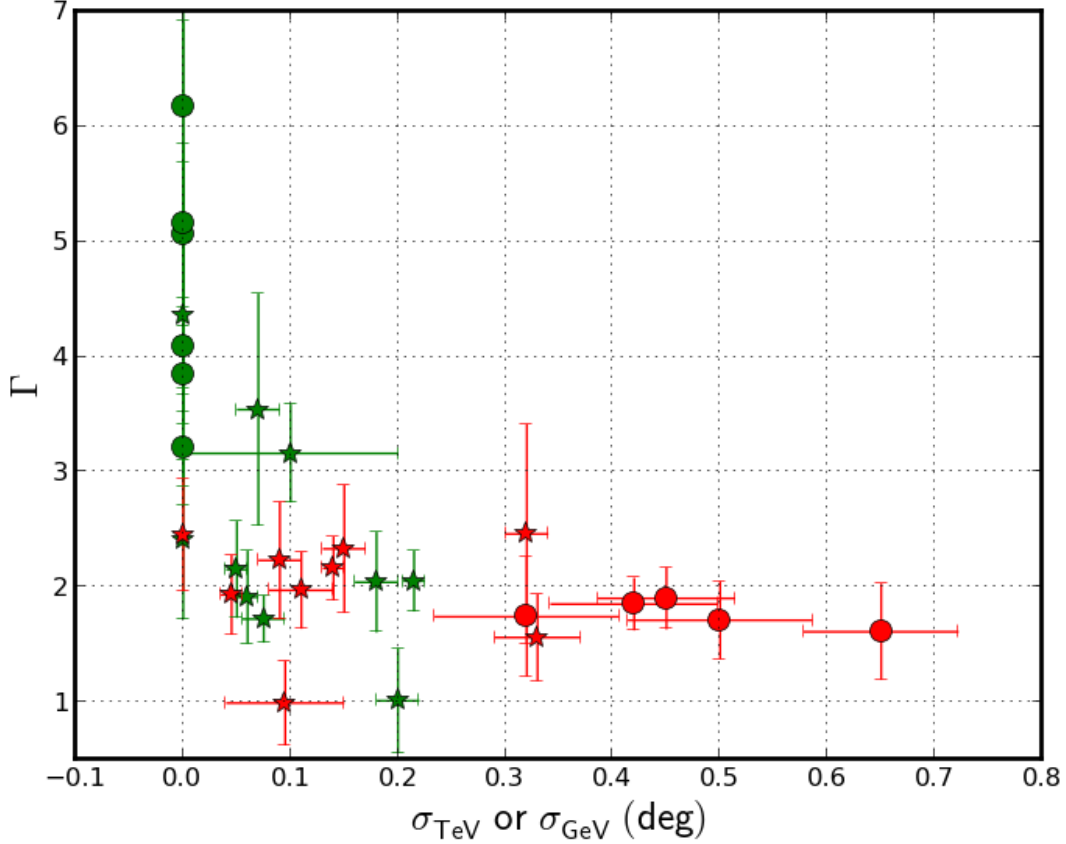


Fig. 4.— Spectral index as a function of the GeV or TeV extension for each detected source. The GeV morphology is obtained by fitting the position and extension of the sources as explained in Section 4.2 & 4.4. The green markers show the sources within  $0.5^\circ$  of a pulsar detected by the LAT while the red markers represent the sources with no pulsar detected in the GeV energy range within  $0.5^\circ$ . The error bars show the statistical and systematic uncertainties added in quadrature. The 11 circles represent the sources for which the GeV morphology significantly improved the fit compared to the TeV morphology (Table 5), while the stars represent the sources modeled assuming their TeV morphology. For sources modelled assuming their TeV morphology, we reported the uncertainties found in the associated reference in Table 1. For asymmetric sources we represented the mean extension with an error bar corresponding to the maximum uncertainty.

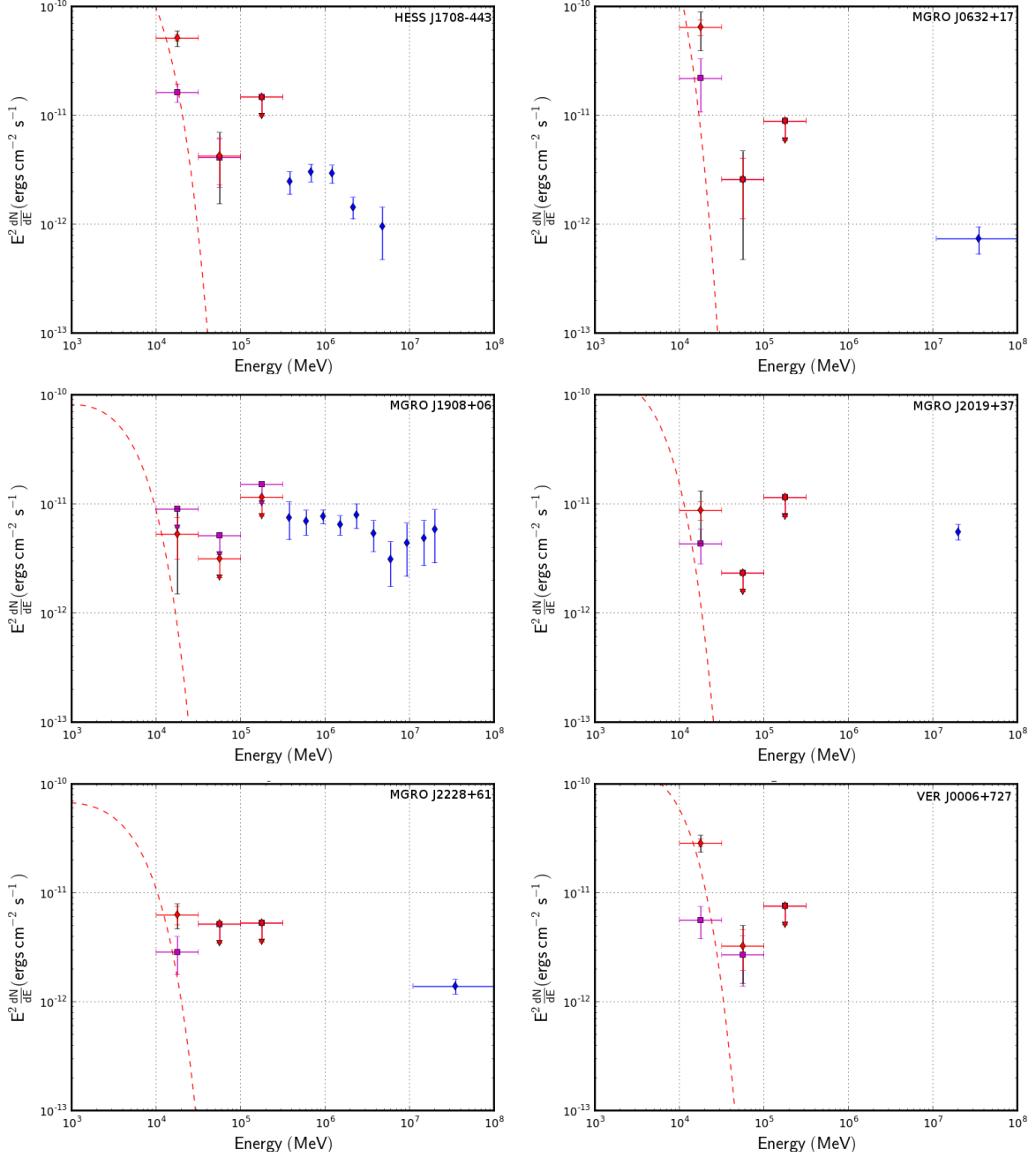


Fig. 5.— SED of sources better described by a point-like source and with a pulsar within  $0.5^\circ$ . The blue points show the TeV points taken from Abramowski et al. (2011b); Abdo et al. (2009f); Aharonian et al. (2009); Abdo et al. (2007b, 2009f); McArthur (2011). The red circles and the magenta squares show respectively the SED without the pulsar included in the model and with the pulsar included in the model. The black error bars show the statistical and systematic uncertainties added in quadrature. The dashed line corresponds to the model of the associated pulsars summarized in Table 10. In the case of MGRO J1908+06, the red SED was derived assuming a point-like source as determined in Table 5 while the magenta SED was derived assuming the TeV shape since it is not significant anymore when the pulsar is included in the model.

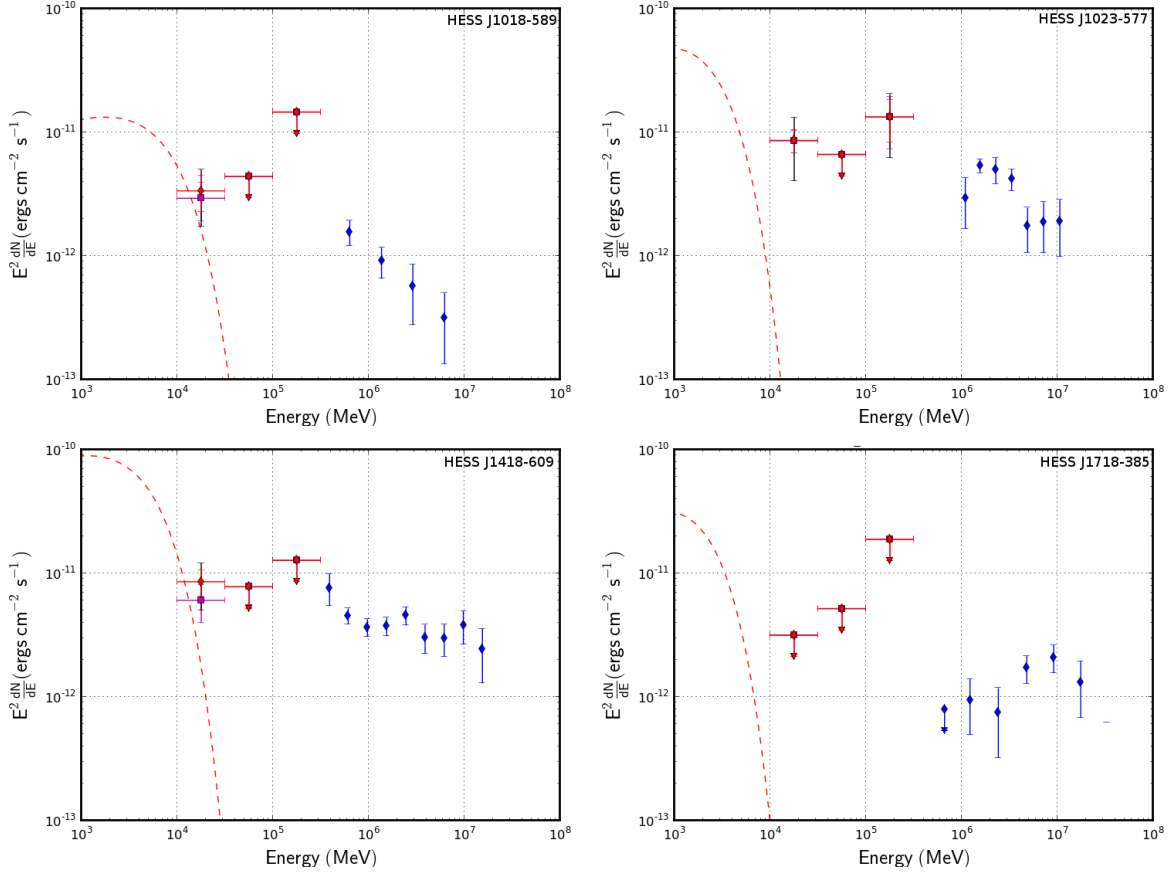


Fig. 6.— SED of sources better described by the TeV shape and with a pulsar within  $0.5^\circ$ . The blue points show the TeV points taken from the associated paper in Table 1. The red circles and the magenta squares show respectively the SED without the pulsar included in the model and with the pulsar included in the model. The black error bars show the statistical and systematic uncertainties added in quadrature. The dashed line corresponds to the model of the associated pulsars summarized in Table 10.



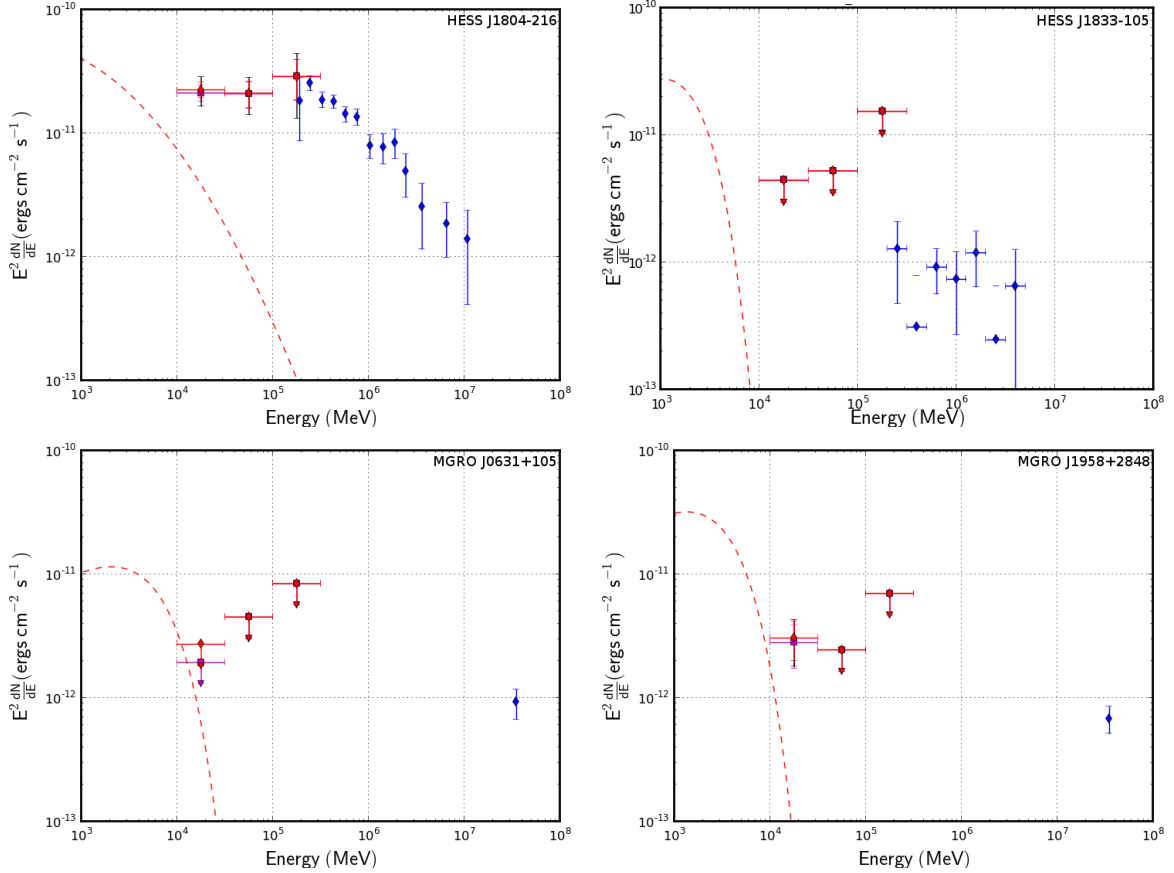


Fig. 7.— SED of sources better described by the TeV shape and with a pulsar within  $0.5^\circ$ . The blue points show the TeV points taken from the associated paper in Table 1. The red circles and the magenta squares show respectively the SED without the pulsar included in the model and with the pulsar included in the model. The black error bars show the statistical and systematic uncertainties added in quadrature. The dashed line corresponds to the model of the associated pulsars summarized in Table. 10.

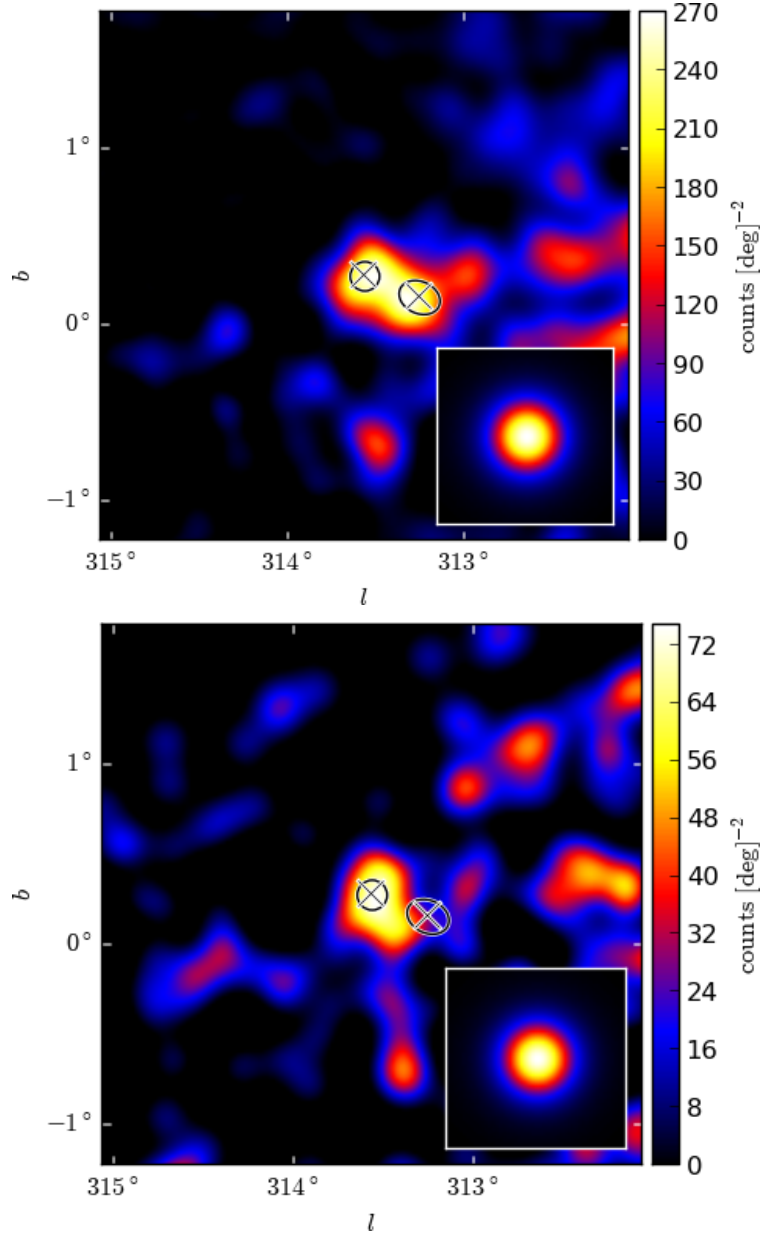


Fig. 8.— Smoothed counts map of the region of the Kookaburra complex observed by Fermi above 10 GeV (Top) and 30 GeV (Bottom). The Galactic diffuse emission is subtracted. The circle and right ellipse show the best fit obtained in TeV respectively for the K3 nebula and the Rabbit nebula.

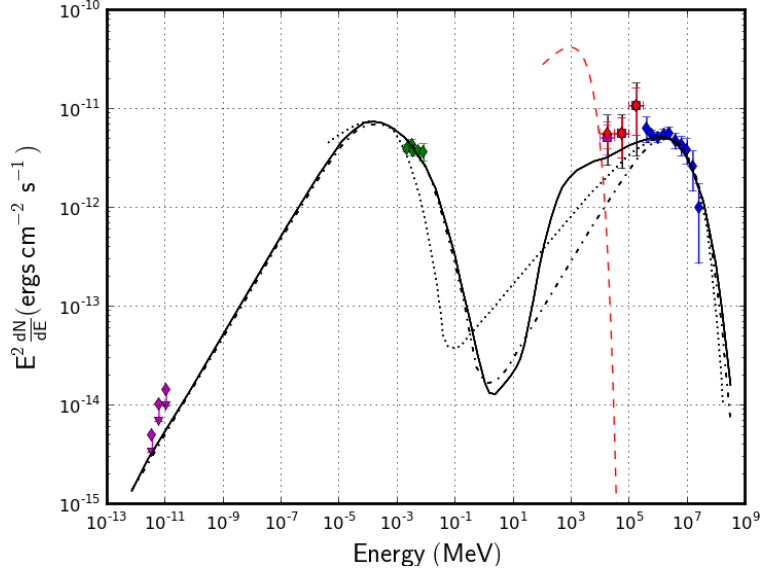


Fig. 9.— SED of HESS J1420-607. The blue, green and magenta points respectively show the spectral points obtained by HESS (Aharonian et al. 2006a), by Suzaku (Van Etten & Romani 2010) and the upper limits derived in radio. The red points and the magenta squares show the spectral points obtained in this work without and with the pulsar included in the model. In the LAT energy range the black error bars show the statistical and systematic uncertainties added in quadrature. The red dashed line corresponds to the 2FGL spectrum of the PSR J1420-607. The three black lines show the results of SED modeling for the broad extended nebula emission presented in previous works. The solid and dot dashed lines respectively shows to the hadronic plus leptonic and leptonic models proposed by Van Etten & Romani (2010). The dotted line corresponds to the leptonic model proposed by Kishishita et al. (2012) assuming an ambient magnetic field of  $3\mu\text{G}$ .

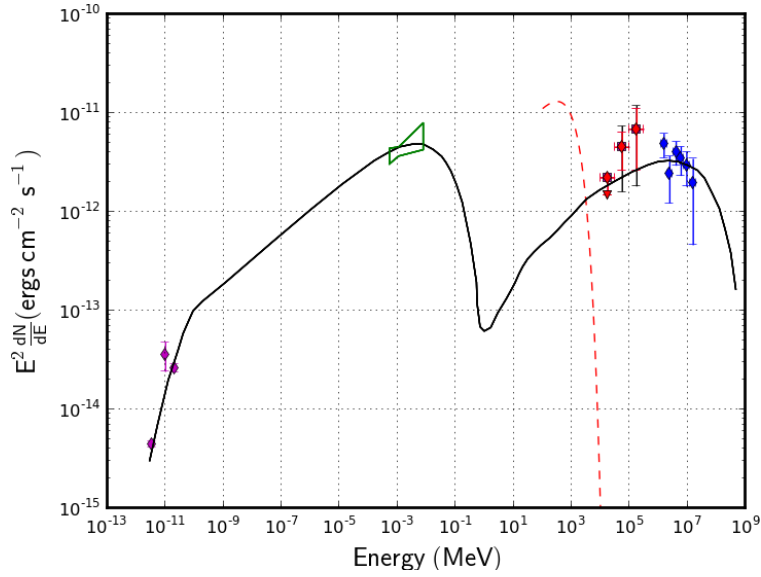


Fig. 10.— SED of HESS J1356-645. The blue, green and magenta points represents the results obtained by HESS (Abramowski et al. 2011c), the X-ray data (Lemoine-Goumard et al. 2011b) and the radio data (Murphy et al. 2007; Duncan et al. 1995; Griffith & Wright 1993). The red and magenta points between 10 and 316 GeV show the points obtained in this work without and with PSR J1357-6429 included in the model. In the LAT energy range the red and black error bars respectively show the statistical and systematic uncertainties added in quadrature. The solid line presents the one-zone leptonic model proposed by Abramowski et al. (2011c).

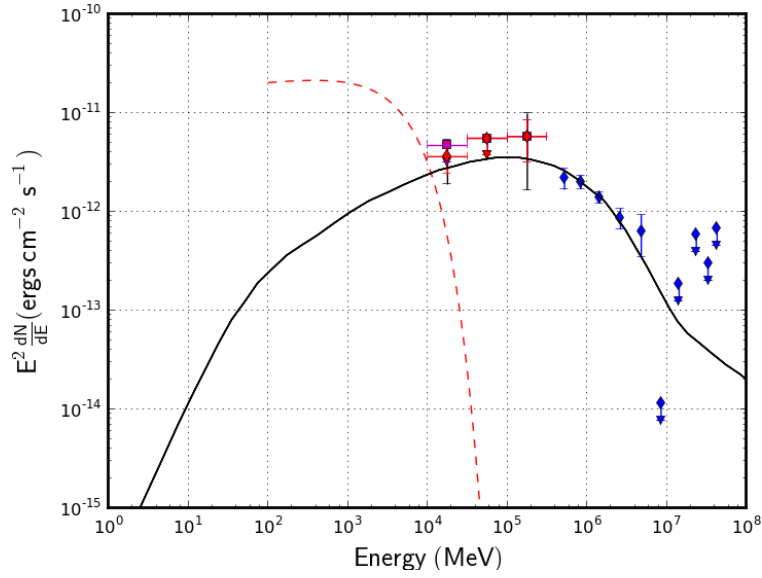


Fig. 11.— SED of HESS J1119–614. The blue points represent the HESS data (Mayer 2010). The red and magenta points between 10 and 316 GeV show the points obtained in this work without and with PSR J1119–6127 included in the model. In the LAT energy range the red and black error bars respectively show the statistical and systematic uncertainties added in quadrature. The solid line shows the model proposed by Mayer (2010). The red dashed line corresponds to the model of PSR J1119–6127 (Nolan et al. 2012).

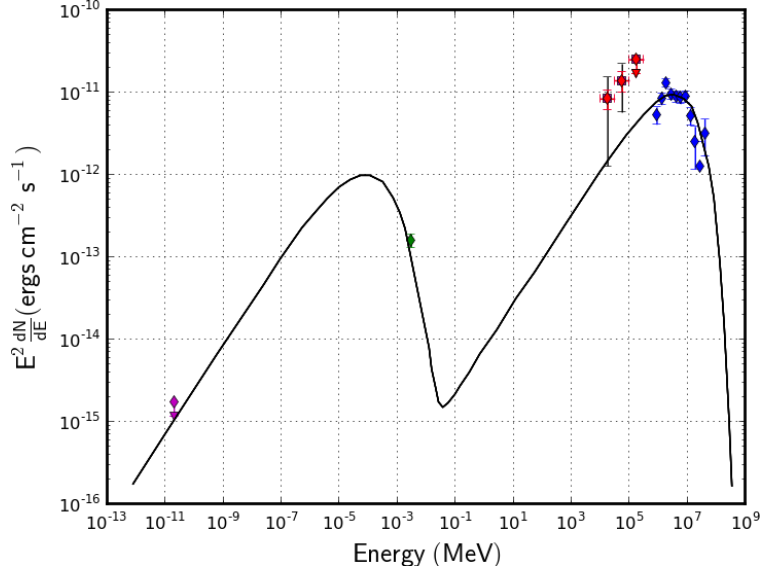


Fig. 12.— SED of HESS J1303-631. The blue, green and magenta points represents HESS results, the radio data and *Chandra* results (Abramowski in prep.). In the LAT energy range the red and black error bars respectively show the statistical and systematic uncertainties added in quadrature. The solid line shows the leptonic model proposed by Abramowski (in prep.).

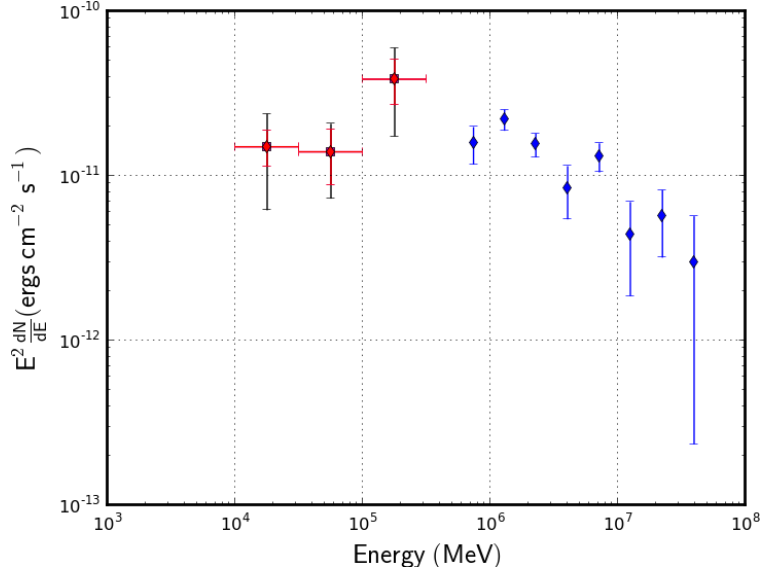


Fig. 13.— SED of HESS J1841-055. We reported the spectral points obtained using H.E.S.S. data in blues as well as the *Fermi*-LAT spectral points in red. The red and black error bars respectively show the statistical and systematic uncertainties added in quadrature.

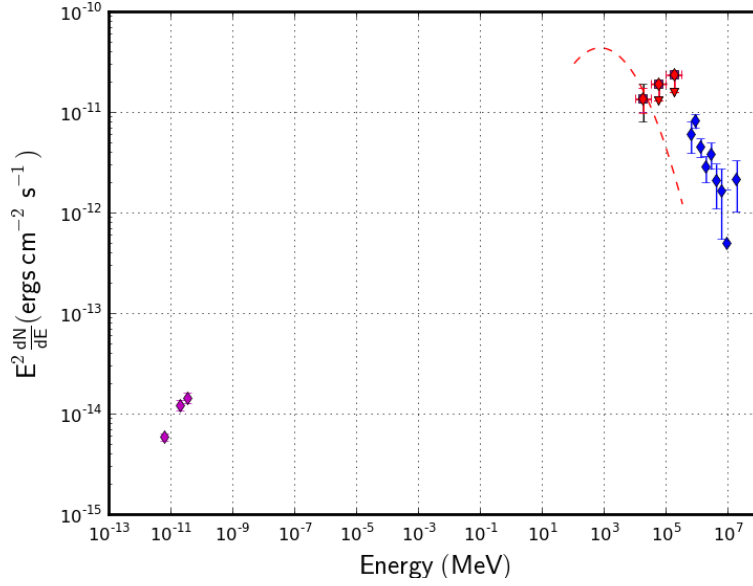


Fig. 14.— SED of HESS J1848–018. H.E.S.S. pectral points from Chaves (2010) are presented in blue while the radio points corresponding to the W43 central cluster from Luque-Escamilla et al. (2011) are indicated in magenta. Red points represent *Fermi*-LAT data. The red and black error bars respectively show the statistical uncertainties and statistical plus systematic uncertainties added in quadrature. The red dashed line corresponds to the SED derived in Lemoine-Goumard et al. (2011a) using *Fermi*-LAT data and assuming a Gaussian shape of  $0.3^\circ$ .

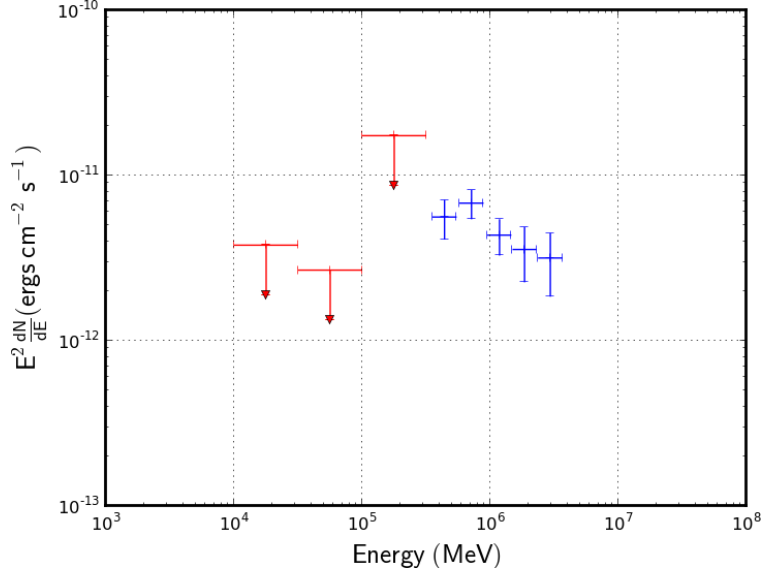


Fig. 15.— SED of HESS J1026–582. H.E.S.S. spectral points are reported in blue while *Fermi*-LAT upper limits are indicated in red.

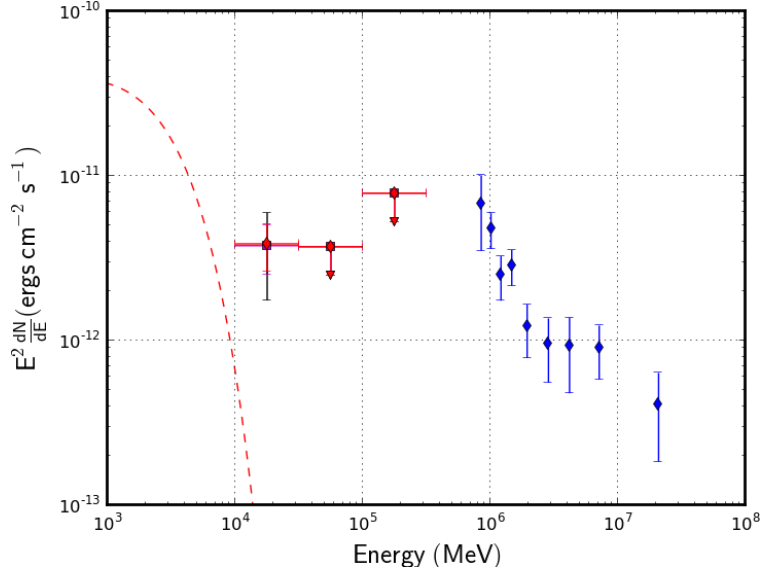


Fig. 16.— SED of HESS J1458–608. H.E.S.S. spectral points are reported in blue while *Fermi*-LAT spectral points are represented in red. The magenta points show the *Fermi*-LAT points obtained once PSR J1459–60 added to the model. The black error bars show the statistical and systematic uncertainties added in quadrature.



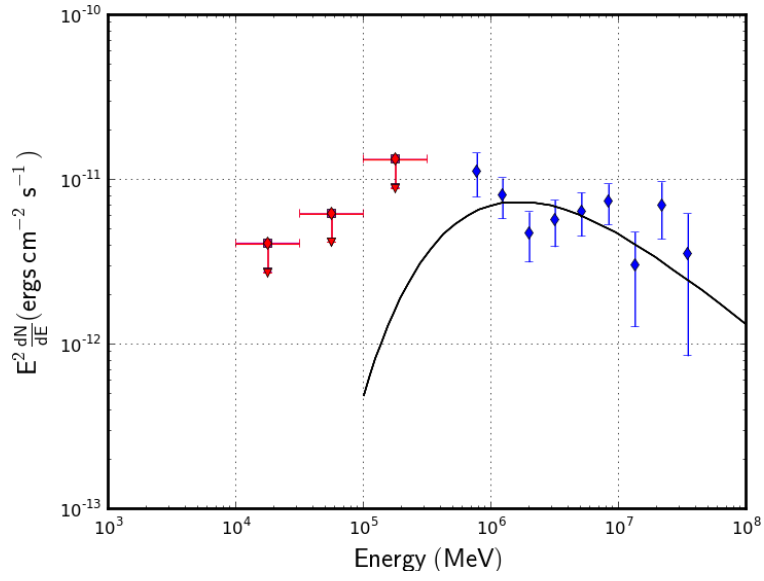


Fig. 17.— SED of HESS J1626–490. H.E.S.S. spectral points are reported in blue while *Fermi*-LAT upper-limits are indicated in red.

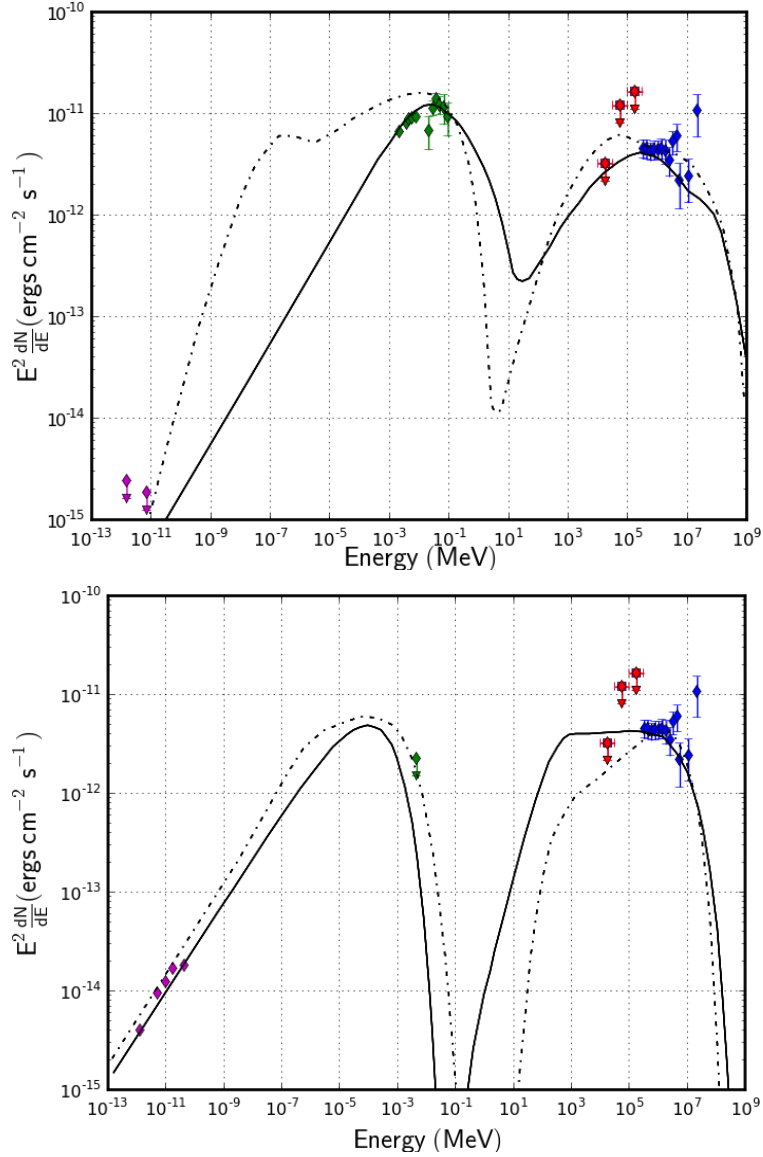


Fig. 18.— SED of HESS J1813–178. The blue and red points show the H.E.S.S. (Aharonian et al. 2006d) and *Fermi*-LAT spectral results. The radio data (magenta) are from VLA, Bonn, Parkes, and Nobeyama observatories (Brogan et al. 2005). The X-ray data are from XMM-Newton (Funk et al. 2007b) and INTEGRAL (Ubertini et al. 2005). These points were derived either for the shell of the SNR and for the core (PWN). The solid and dot dashed lines respectively correspond to the models proposed by Funk et al. (2007b) and by Fang & Zhang (2010). Top : Leptonic scenario in which the radiation is created by a PWN. Bottom : Hadronic scenario in which the radiation is created by the SNR.

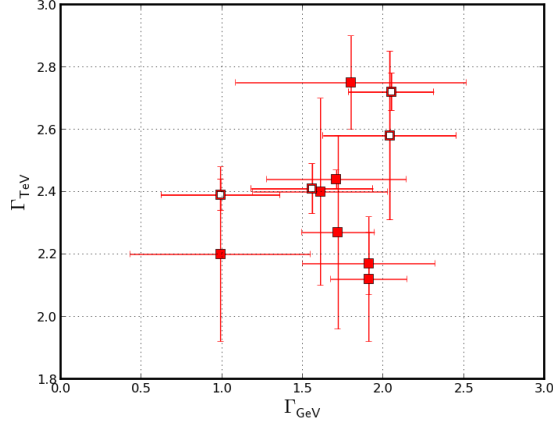


Fig. 19.— TeV spectral index as a function of the GeV spectral index for sources detected in our analysis for which the informations on the pulsar are available. These sources are summarized in Table 11. Full markers represent sources with a clear PWN association at TeV energies while hollow markers correspond to sources for which the association between TeV emission and a PWN is less clear. The dashed line corresponds to the symmetry compared to an index of 2. Pulsars summarized in Table 10 are included in the model.

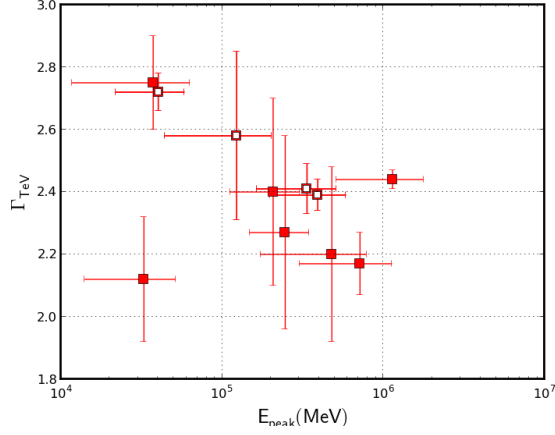


Fig. 20.— TeV spectral index as a function of the energy of the maximum of the IC peak for sources detected in our analysis for which the informations on the pulsar are available. These sources are summarized in Table 11. Full markers represent sources with a clear PWN association at TeV energies while hollow markers correspond to sources for which the association between TeV emission and a PWN is less clear. Pulsars summarized in Table 10 are included in the model.

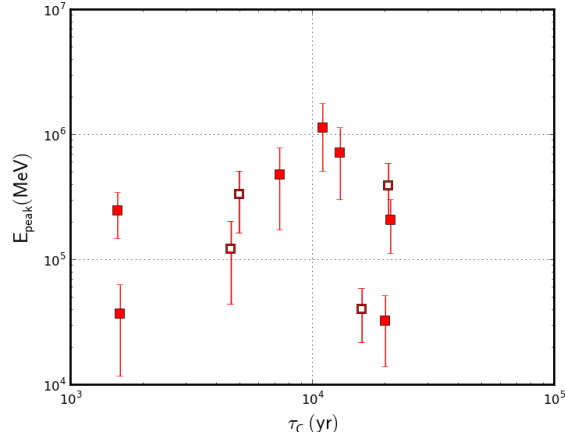


Fig. 21.— Energy of the maximum of IC peak as a function of the characteristic age of the pulsar for sources detected in our analysis for which the informations on the pulsar are available. These sources are summarized in Table 11. Full markers represent sources with a clear PWN association at TeV energies while hollow markers correspond to sources for which the association between TeV emission and a PWN is less clear. Pulsars summarized in Table 10 are included in the model.

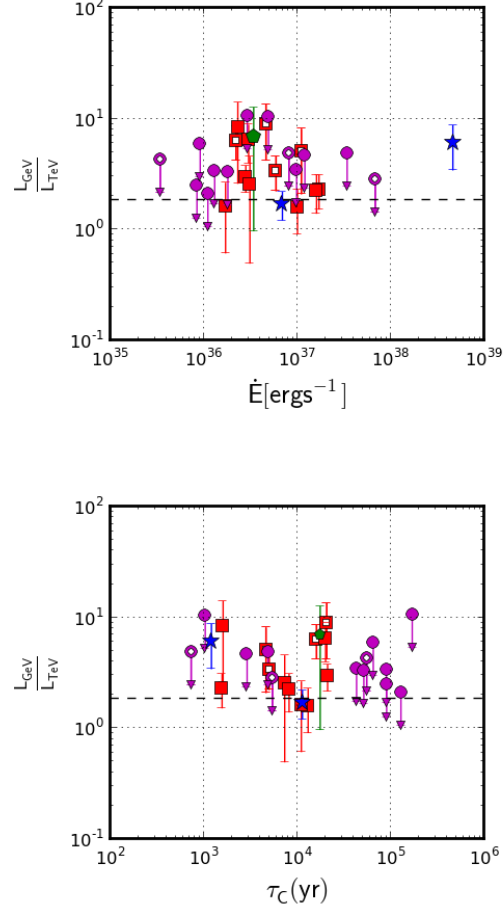


Fig. 22.— Ratio of luminosity of the PWN in GeV over the luminosity in TeV as a function of the pulsar spin-down power (top) and the pulsar characteristic age (bottom). Full markers correspond to sources with a clear PWN association at TeV energies while hollow markers correspond to sources for which the association between the TeV emission and a PWN is less clear. The red squares (■) represent the sources detected at GeV energies, the magenta circles (●) show the upper limits, the green pentagon (⬠) represent the sources showing a pulsar behaviour in the energy range and the blue stars (★) represent the Crab nebula and Vela-X not studied in this work. Pulsars summarized in Table 10 are included in the model. The dashed line represent the mean ratio found between the GeV and the TeV flux due to the spectral shape of the IC peak.

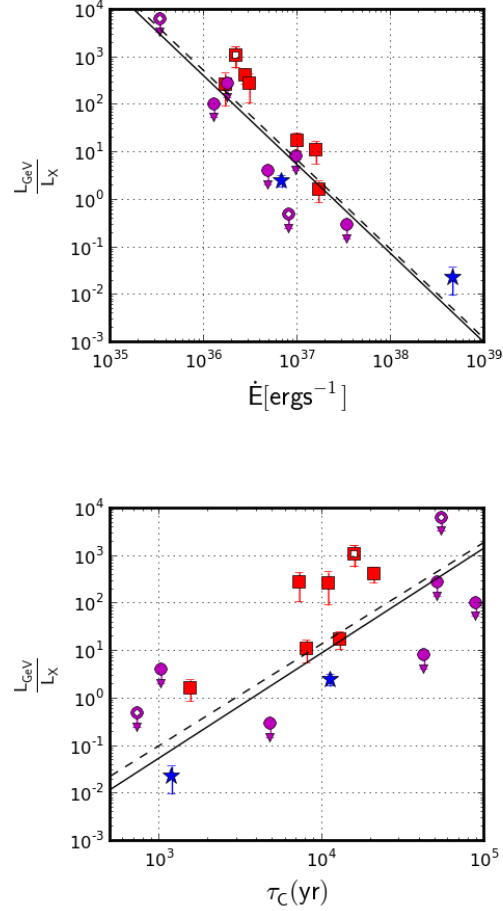


Fig. 23.— Ratio of luminosity of the PWN in GeV over the luminosity in X-rays as a function of the pulsar spin-down power (top) and the pulsar characteristic age (bottom). Full markers correspond to sources with a clear PWN association at TeV energies while hollow markers correspond to sources for which the association between the TeV emission and a PWN is less clear. The red squares (■) represent the sources detected at GeV energies, the magenta circles (●) show the upper limits, the green pentagon (⬠) represent the sources showing a pulsar behaviour in the energy range and the blue stars (★) represent the Crab nebula and Vela-X not studied in this work. Pulsars summarized in Table 10 are included in the model. The dashed and solid lines represent respectively the relations derived in Mattana et al. (2009) multiplied by  $\bar{R}$  for the whole sample of sources and for the sources clearly identify to PWNe.

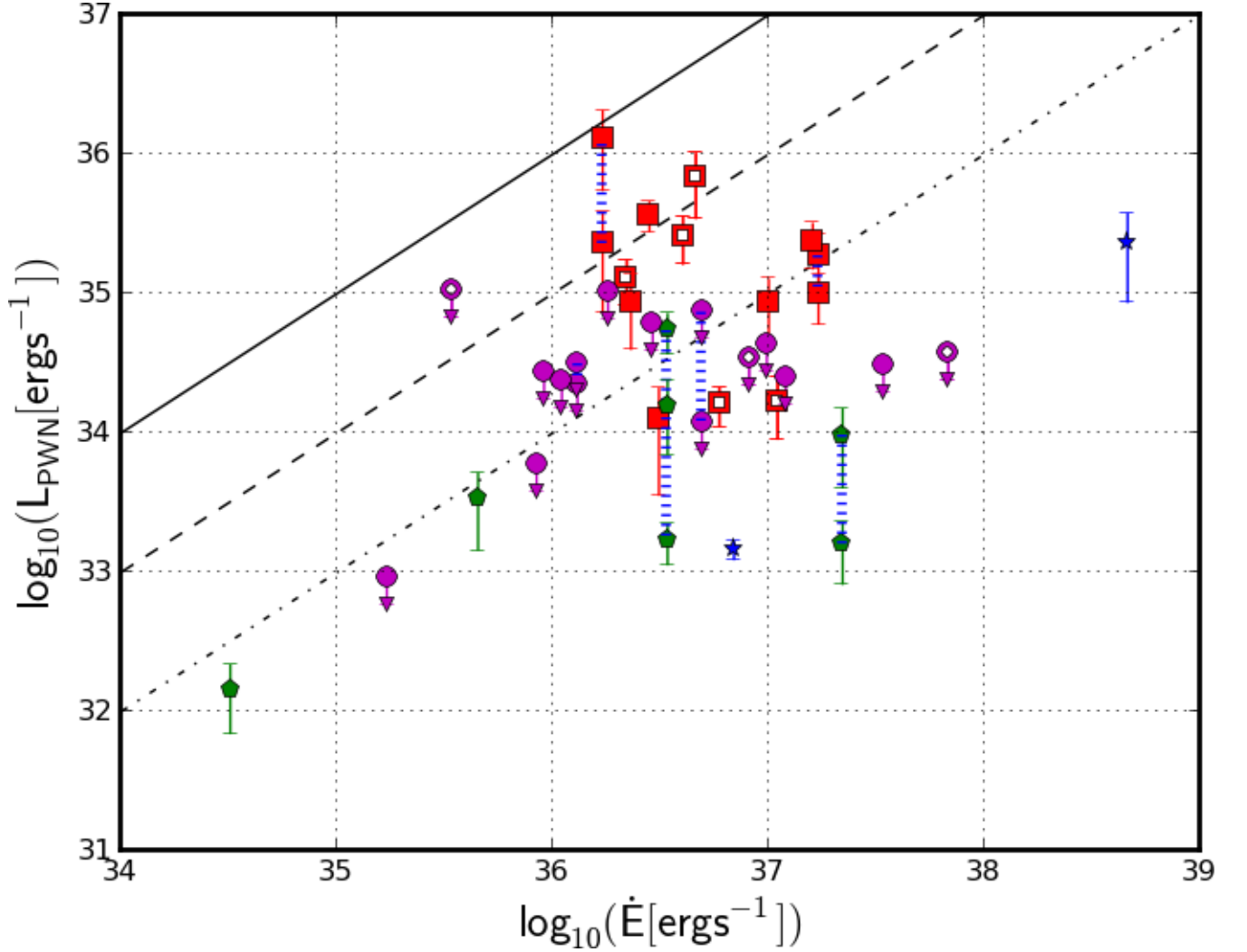


Fig. 24.— Luminosity of the PWN as a function of the pulsar spin-down power. Full markers correspond to sources with a clear PWN association at TeV energies while hollow markers correspond to sources for which the association between the TeV emission and a PWN is less clear. The red squares (■) represent the sources detected at GeV energies, the magenta circles (●) show the upper limits, the green pentagon (⬠) represent the sources showing a pulsar behaviour in the energy range and the blue stars (★) represent the Crab nebula and Vela-X not studied in this work. Sources with two distances estimates have two markers connected with a dotted blue line. Pulsars summarized in Table 10 are included in the model.